SURFACE MORPHOLOGY INVESTIGATION OF A BIODEGRADABLE MAGNESIUM ALLOY

A THESIS SUBMITTED TO
THE GRADUATE SCHOOL OF NATURAL AND APPLIED SCIENCES
OF
MIDDLE EAST TECHNICAL UNIVERSITY

BY

AYDIN TAHMASEBIFAR

IN PARTIAL FULLFILLMENT OF THE REQUIREMENTS
FOR
THE DEGREE OF DOCTOR OF PHILOSOPHY
IN
ENGINEERING SCIENCES

AUGUST 2015

Approval of thesis

SURFACE TREATMENT OF BIODEGRADABLE MAGNESIUM ALLOYS

submitted by **AYDİN TAHMASEBİFAR** in partial fulfillment of the requirements for the degree of **Doctor of Philosophy in Engineering Sciences Department, Middle East Technical University** by**,**

Prof. Dr. Prof. Dr. Gülbin Dural Ünver ______________________
Dean, Graduate School of **Natural and Applied Sciences**

Prof. Dr. Murat Dicleli ______________________
Head of Department, **Engineering Sciences**

Prof. Dr. Zafer Evis ______________________
Supervisor**, Engineering Sciences Dept., METU**

Prof. Dr. Muammer Koç ______________________
Co-Supervisor**, Sustainability Dept., HBKU, Qatar**

Examining Committee Members:

Prof. Dr. Hasan Okuyucu ______________________
Materials Engineering Dept., Yıldırım Beyazıt University

Prof. Dr. Zafer Evis ______________________
Engineering Sciences Dept., METU

Assoc. Prof. Dr. Yusuf Usta ______________________
Mechanical Engineering Dept., Gazi University

Assoc. Prof. Dr. Ayşen Tezcaner ______________________
Engineering Sciences Dept., METU

Assoc. Prof. Dr. M. Tolga Yılmaz ______________________
Engineering Sciences Dept., METU

Date: 20/08/2015

I hereby declare that all information in this document has been obtained and presented in accordance with academic rules and ethical conduct. I also declare that, as required by these rules and conduct, I have fully cited and referenced all material and results that are not original to this document.

Name, Last name: Aydin Tahmasebifar
Signature:

ABSTRACT

SURFACE MORPHOLOGY INVESTIGATION OF A BIODEGRADABLE MAGNESIUM ALLOY

Tahmasebifar, Aydin
PH.D., Department of Engineering Sciences

Supervisor: Prof. Dr. Zafer Evis
Co-Supervisor: Prof. Dr. Muammer Koç

August 2015; 118 Pages

In this study, the effect of manufacturing conditions (i.e. compaction pressure, sintering temperature and time) on physical, mechanical and electrochemical properties of Mg alloy discs as samples of biomedical implants prepared using powder forming technology were investigated. The main motivation of this study was to achieve the manufacturing of porous and micro-surface textured Mg-based biomedical implants with good mechanical and electrochemical properties. A Box-Behnken and Full Factorial experimental design was used in experimentation. Relative densities of the plates were obtained experimentally. They varied from 69.7±1% to 81.5±4%. According to ANOVA (Analysis of variances) test, manufacturing conditions did not affect the relative density significantly except the compaction pressure level. The bending strength was in the range of 30.3±2 MPa and 53.7±1 MPa. Compaction pressure led to an increase in the bending strength while sintering temperature and time decreased. Electrochemical tests were conducted using Hank's solution, DMEM (Dulbecco's Modified Eagle's Medium) and 10% FBS (Fetal Bovine Serum)+DMEM. The lowest and the highest corrosion potentials were measured in Hank's and 10% FBS+DMEM solutions, respectively. Pitting corrosion was detected on the surface of Mg alloy discs. In Hank's solution, pitting corrosion was observed more than DMEM and 10% FBS+DMEM. The discs with smooth surfaces also showed lower corrosion resistance than the discs with porous and micro-textured surfaces in the presence of

FBS. It was concluded that the manufacturing of porous and micro-surface textured Mg based biomedical implant using powder forming process was reasonable due to the convenience of near net shape production with sufficient material properties. Also, the cell culture studies showed that micro texture and roughness positively affected cell adhesion, proliferation and osteogenic activity. AZ91D-Mg alloy plates showed good cytocompatibility with higher cell proliferation compared to control groups at each incubation time period.

Keywords: Powder Metallurgy, Micro-texture, Porous Surface, Biomedical Implant.

ÖZ

BİOBOZUNUR MAGNEZYUM ALAŞIMININ YÜZEY MORFOLOJISININ ARAŞTIRILMASI

Tahmasebifar, Aydin
Doktora, Mühendislik Bilimleri Bölümü

Tez Yöneticisi: Prof. Dr. Zafer Evis
Ortak Tez Yöneticisi: Prof. Dr. Muammer Koç

Ağustos 2015; 118 Sayfa

Bu çalışmada, üretim şartlarının (örneğin: basma basıncı, sinterleme sıcaklığı ve zamanı) biyomedikal implant örnekleri olarak toz şekillendirme teknolojisi ile hazırlanmış Mg alaşımı disklerinin fiziksel, mekanik ve elektrokimyasal özellikleri üzerindeki etkisi araştırılmıştır. Çalışmanın temel amacı iyi mekanik ve elektrokimyasal özelliklere sahip gözenekli ve yüzey dokulu Mg tabanlı biyomedikal implant üretiminin başarılmasıdır. Deneylerde Box-Behnken ve tam faktöriyel deney tasarımı kullanılmıştır. Plakaların bağıl yoğunlukları deneysel olarak elde edilmiştir. Onlar 69.7±1% ile 81.5±4% arasında değişmiştir. Varyans analizi testine göre sıkıştırma basıncı hariç diğer üretim şartları bağıl yoğunluğu etkilememiştir. Ayrıca, eğme dayanımı 30.3±2 MPa ile 53.7±1 MPa seviyesindedir. Sıkıştırma basıncı eğme dayanımında artışa neden olurken sinterleme sıcaklığı ve zamanı düşürmüştür. Elektrokimyasal testler Hank solüsyonu, DMEM ve 10% FBS (Fetal Sığır Serumu)+DMEM karışımı kullanılarak yapılmıştır. En yüksek ve en düşük korozyon potansiyelleri sırasıyla Hank solüsyonu ve 10% FBS (Fetal Bovine Serum)+DMEM karışımında ölçülmüştür. Mg alaşımı disklerinin yüzeyinde oyuk korozyonu tespit edilmiştir. Oyuk korozyonu Hank solüsyonunda DMEM ve 10% FBS+DMEM solüsyonuna göre daha fazla görülmüştür. Ayrıca, FBS varlığında düz yüzeyli diskler gözenekli ve mikro desenli yüzeyli disklere göre daha düşük korozyon direnci göstermiştir.

Toz şekillendirme işlemi ile gözenekli ve mikro yüzey desenli Mg tabanlı biyomedikal implant üretimi bu yöntemin nete-yakın-biçim ile ve yeterli malzeme özellikleri ile üretime elverişli olmasından dolayı uygun olduğu sonucuna varılmıştır. Öte yandan, hücre kültürü çalışmaları mikro desenlerin ve pürüzlülüğün hücre yapışması, çoğalması ve ostejenik aktivite üzerinde pozitif etkisi olduğunu göstermiştir. Hücre kültürü çalışmalarıyla uyumlu olarak, AZ91D Mg plakalarının hücre canlığının her zaman periyodunun sonunda pozitif kontrolden yüksek ölçülmesi ile iyi bir biyouyumluluk göstermiştir.

Anahtar Kelimeler: Toz Metalürji, Mikro-desen, Gözenekli Yüzey, Biyomedikal İmplant.

To the memory of my father
and
To my beloved mother

ACKNOWLEDGMENTS

I would like to express my endless appreciation to my supervisor Prof. Dr. Zafer Evis for giving me the chance, believing me and his permanent presence and support during all periods of this study. The courage of starting this study and later on overcoming all problems wouldn’t be possible without his valuable and precious guidance. I am also so grateful to my supervisor for encouraging me in this fascinating field and for letting me benefit from his profound mind and knowledge.

I would also to express my gratitude to my co-supervisor Prof. Dr. Muammer Koç whose leadership took this research to the place it is. His support and feedback helped me on solving problems during this study.

I would like to thank Assoc. Prof. Dr. Ayşen Tezcaner, who supported me during Cell culture studies and designing of mold surface.

I would like to express my special thanks to Said Murat Kayhan who helped me in this experimental study. His cooperation and friendship made this work easier.

I should thank, Prof. Dr. Zafer Evis, Assoc. Prof. Dr. Ayşen Tezcaner and Assoc. Prof. Dr. Dilek Keskin for their generosities to let me work in their biomaterial laboratory. I owe my thank to my lab friends; Dr. Ömer Akturk, Sibel Ataol, Deniz Atila, Hazal Aydoğdu, Yağmur Çalışkan, Ali Deniz Dalgıç, Dr. Özge Erdemli, Merve Güldiken, Zeynep Gürtürk, Nil Göl, Dr. Ayşegül Kavas, Alişan Kayabölen, Reza Moonesi Rad, Bora Onat, Engin Pazarçeviren and Dr. Bengi Yılmaz for their support, friendship and the lovely environment they created in our lab.

This study is funded by the Scientific and Technological Research Council of Turkey (TUBITAK) under Award No: 112M340.

I also have to thank my close friends Payman Virani, Anar Tabestani, Adnan Mousavi, Said Murat Kayhan, Engin Pazarçeviren, Yasemin Özgül and Kaveh Hasan Zehtab for their precious friendship. With their presence, the joy they bring into my life and their constant support, they mean more than friends to me.

The last but the most, there is no word to state how grateful I am to my family beside love. To my father, Aziz Tahmasebifar that encouraged me to graduate study

and I owe my all to him. The happy memory of my father still provides a persistent inspiration in my life. I would like to give my greatest thanks to my mother Farideh Tabestani for the value she taught and for the endless support provided through my entire life. Also, I would like to express my special thanks to my brother, Dr. Arif Aziz (Tahmasebifar) as well as my sisters Dr. Vida, Sheida and Leila Tahmasebifar. Their confidence in me, their ideas and constant support have always given me inspiration and the strength I needed at every stage of my life, as in this study.

TABLE OF CONTENTS

CHAPTERS

LIST OF TABLES

LIST OF FIGURES

CHAPTER 1

INTRODUCTION

There has been an increasing need for continuous innovations in health sciences and biomaterials engineering to discover effective treatment methods and design of novel implants due to prolonged average life expectancies and a consequent increase in orthopedic fracture cases. Therefore, innovative solutions in biomedical implants (BI) such as hip, knee, retina and dental implants, scaffolds, degradable screws and plates, drug delivery systems etc. have gained importance in recent years (Bartolo et al., 2012). BI's offer proper and fast medical treatment process for patients who suffer from bone diseases. However, recent improvements in implant materials, design and manufacturing technologies are not to the adequate level to entirely cope with orthopedic fracture fixation and implant issues of durability and biocompatibility as the average life of an implant is no longer than 10-15 years. Increasing number of cases is reported with a need to remove an implant when a fracture is healed or when it completes its service life. Consequently, innovative way of thinking will be needed in biomedical engineering further in the near future as long as bone injury is a part of human lives.

Biodegradable and biocompatible implants have emerged as an excellent alternative implant idea to enable temporary use in a living system without a need for removal. Biocompatibility and biodegradability are very critical and versatile issues in evaluating the success of temporary implants.

In the next generation of biomedical fixation plates and screws, it is expected that biodegradable implants will substitute for non-degradable implants as they exhibit multiple advantages over non-degradable implants in terms of cost, time and risks. While conventional non-degradable biomedical implants need two surgical interventions (the first one is for inserting, the second one is for de-inserting), biodegradable implants do not require the second surgical intervention as they degrade in the body without any side effect. Thus, biodegradable implants offer a great opportunity to reduce cost, time, and patient anxiety, probably the most important benefit, by preventing the second surgical operation. It must be kept in mind that an increase in the number of surgical operations on a patient, particularly if they are elderly, also increases the risks for side effects, if not life, on patients. Moreover, it leads to unnecessary medical complications, unexpected costs and time away from a productive social life.

In this study, Mg-based biodegradable implant with micro-texture surface was designed and manufactured by a powder metallurgy (PM) method for the first time. Moreover, it was aimed to improve corrosion resistance and biological activity.

1.1 Powder Metallurgy

Powder metallurgy (PM) is a manufacturing technique that used metal or ceramic powders ranging from 0.1 to 200 μm as a raw material (Lai et al., 2014; Swamy et al., 2014). The final product is produced by changing the shape, properties and structure of powders. The most important advantage of PM to other manufacturing method is higher control to microstructure of final product (Lai et al., 2014). There is no need for expensive machining and finishing due to near-net-shape of final product in PM. Additionally, products with highly porous architecture can produced by this method. The theoretical porosity achieved in PM is 50%. However, porosity between 5 to 37% can be easily achieved by controlling the compaction pressure and morphology of powders.

It has been widely used in many sectors such as manufacturing of porous filters, oxide strengthened turbine alloys, functionally gradient artificial bones and contact alloys, etc (Exner and Arzt, 1990). PM technique can be divided in three main stages which are: 1) powder technology, 2) powder processing and 3) characterization properties and testing (Fig. 1).

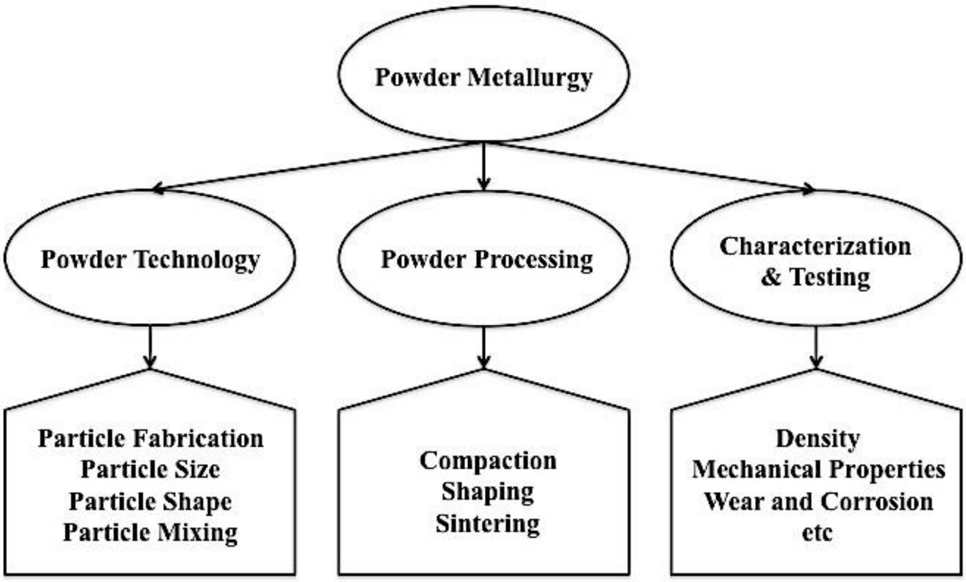

Figure 1: Powder metallurgy stages

1.1.1 Powder Compaction

Powders are compacted to densify by the application of pressure. In the first step, particles slide over together and then deformed by the application of a high pressure (Exner and Arzt, 1990; Smith et al., 1998). The rearrangement and small densification of powders are result of the application of low pressure. The plastic deformation and change in particle shapes are occurred by increasing the pressure beyond yield strength of powders and finally particles bond together (Exner and Arzt, 1990; Smith et al., 1998). Thus, the applied pressure, powder, shape, size and die tool have great effect on green density and strength.

Density is increased expeditiously at low pressure. However, the densification rate is decreased by failing of pores and resisting of particles to deformation at higher compaction pressures (Fig. 2). Thus, density is increased by increasing compaction pressure due to increasing coordination number and contact area between powder particles (Čapek and Vojtěch, 2014). Die-wall friction is an important limitation in compaction of powders. Density gradient of green compact is a result of die-wall friction phenomena that inhibits rejection of sample (Čapek and Vojtěch, 2014). Die-wall friction is decreased with increasing the distance from die-wall so close to die is denser. As a result, the ejection force is raised by increasing die-wall friction. Also, die-wall friction is increased by increasing compaction pressure (Čapek and Vojtěch, 2014).

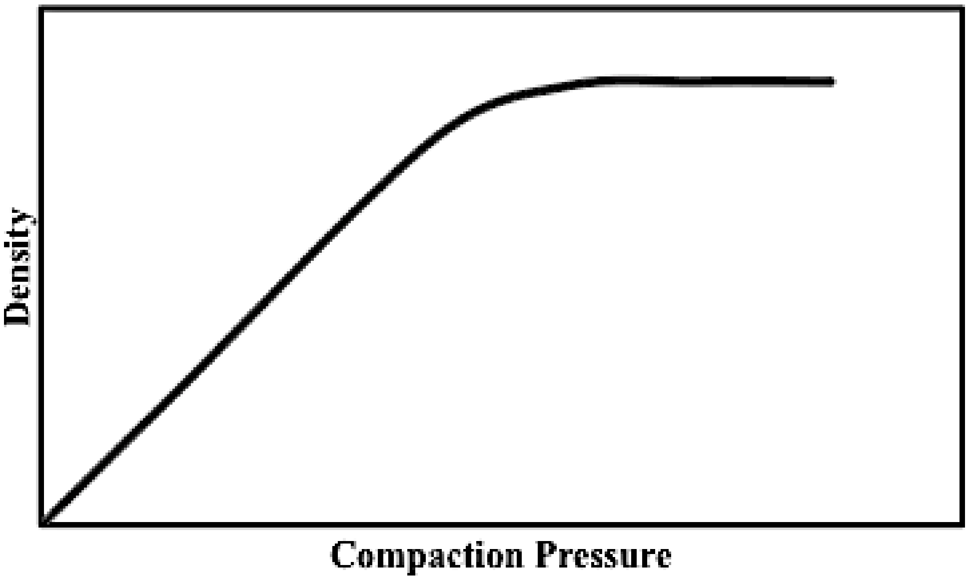

Figure 2: Relationship between compaction pressure and density

Another important parameter in compaction stage is mechanical properties of powders. The compressibility of powders depends on powder hardness (Smith et al., 1998). Thus, the compaction of extremely hard particles is too difficult while very soft particles are easily deformed (Andersson et al., 2014). It was proved that soft particles resist to deformation at high compaction pressure and achieve higher density at intermediate compaction pressures. Polymer particles are used to improve compressibility of very hard metal or ceramic particles. Polymer particles as a binder increase green density of extremely hard particles up to 60%. On the other hand, high compaction pressure gives more dense samples for powders that are not very hard and soft (Andersson et al., 2014).

Compressibility of powders also depends on powder size. Powders with small particles resist to deformation so compaction of powder with small size is more difficult due to high coordination number and rapid strain hardening (Andersson et al., 2014; Čapek and Vojtěch, 2014). Thus, the particles in nano-scale are used when higher mechanical strength is desired. On the other hand, mixing of nano and micro scale powders improves sintering ability and compressibility which show importance of particle size distribution on PM (Andersson et al., 2014; Čapek and Vojtěch, 2014). Also, the existence of surface contamination such as oxide layer declines the compressibility of powders. In addition to particle size, particle morphology is an important factor (Fig. 3). Powders with irregular shapes achieve higher density after compaction stage due to cold welding and mechanical interlock phenomena. Also, spongy particle with internal pores cannot be compressed easily because of the small pores inside the particles (Andersson et al., 2014).

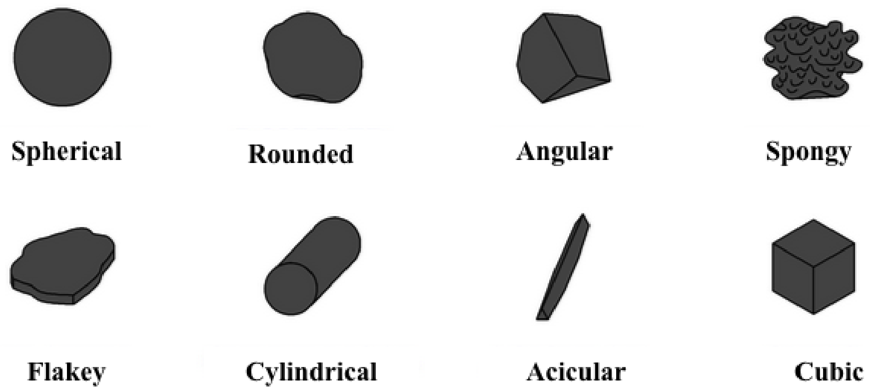

Figure 3: Powder morphology used in PM (Smith et al., 1998)

1.1.2 Sintering

Sintering is a heat treatment process for compacting particles at temperatures below the melting point. The neck growth of contacting particles at microscale should be investigated to determine sintering process (Fig. 4) (Exner and Arzt, 1990). Surface energy that is produced during compaction process is eliminated by sintering of green compact (Exner and Arzt, 1990). Conducted particles are enlarged and overlapped each other. Thus, density is increased and pore size is declined during sintering process. Also, the grain growth occurs due to increase in atomic motion.

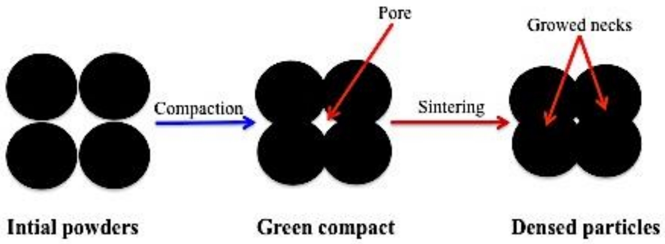

Figure 4: Neck growth during sintering process

Sintering process has two different stages. The first stage is local bonding of adjacent particles (early stage) and then pore shrinkage and rounding are occurred in late stage of sintering (Smith et al., 1998). The total volume of green compact decreases due to shrinking of sintering particles and total pore volume during sintering process (Exner and Arzt, 1990; Smith et al., 1998). The purpose of sintering process is minimization of the free surface enthalpy of the compacted particles (Exner and Arzt, 1990; Smith et al., 1998). Transportation of material is necessary for shrinkage of pores and neck growth from dense material. Five different mechanisms can control the material transportation during sintering. These mechanisms are: 1) migration of vacancies at microstructure, 2) diffusion of grain boundary, 3) surface diffusion, 4) plastic flow and 5) evaporation of atoms located on surface.

Previous studies showed that growth of necks should be investigated in order to find the responsible mechanism during sintering (Exner and Arzt, 1990; Smith et al., 1998). Volume diffusion is a responsible factor in the first stage of sintering for spherical metal particles, while predominant mechanism of glassy material is viscous flow. The pore shrinkage in the late stage of process is controlled by volume diffusion for both metal and glass particles (Smith et al., 1998).

Parameters which play important role in sintering process are: 1) sintering temperature, 2) sintering time, 3) heating rate and 4) sintering environment.

1.2 Biomedical Implants

Any material, surface or device that contacts with biological systems is known as a biomaterial. Biomaterials are classified in four different groups (Metallic, Polymeric, Composite and Ceramic) from material science point of view (Fig. 5).

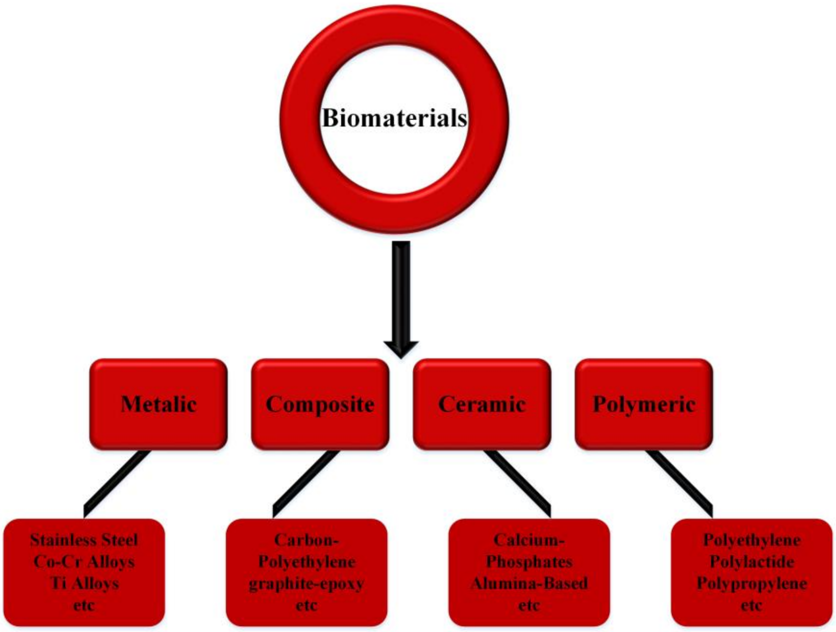

Figure 5: Classification of biomaterials

Ceramic biomaterials such as calcium phosphates are widely used as implants in bone regeneration because of their good biocompatibility, non-toxicity and osteoconductivity (Tahmasebifar et al., 2015). However, their poor mechanical properties and high corrosion rate in acidic environment restrict their usage as a bone implant in load bearing areas (Tahmasebifar et al., 2015).

Polymeric biomaterials are widely used because complex shape and structure can be easily manufactured and also the surface properties of these materials can be easily changed (Ratner et al., 2004). However, polymers are soft materials and cannot tolerate mechanical loading. Moreover, some toxic additives such as plasticizer, antoxidizer or stabilizers are used in synthesis of polymers which can be harmful to host tissue in terms of leaching in body fluid (Ratner et al., 2004). Additionally, chemical and mechanical properties of polymeric materials can be changed during sterilization.

Metal implants are widely used to repair hard tissues due to their outstanding mechanical properties among commercially available biomaterials (Ceramics, polymers and metals) (Table 1). Bio-metal implants such as 316L stainless steel, Co- and Ti-based alloys have established commercial success in medical sector (Wu et al., 2013).

Table 1: Mechanical properties of metal implants (Wu et al., 2013)

Materials	**Young's Modulus (GPa)**	**Yield Strength (MPa)**	**Ultimate Tensile Strength (MPa)**
Compact bone	10-27	-	-
Trabecular bone	1-2	10-90	120-200
Ti6Al4V	110	860	930
Ti6Al7Nb	105	795	860
Ti5Al2.5Fe	110	820	900
Ni-Ti	80	70-140	700-1100
Co-Based	220-230	450-1500	655-1900
316L Stainless steel	193	205-380	515-585
Mg-based	40-45	75-200	135-285

Metal implants are favored as a long term load bearing implants due to their high strength and outstanding ductility that lead to high resistance to fracture (Wu et al., 2013). Also, metal implants with complex architecture can be easily produced by casting, conventional machining and powder metallurgy, etc (Wu et al., 2013). Thus, good biocompatibility and matching of mechanical properties are two important factors for bone implants (Wu et al., 2013). Biocompatibility of bio-metal implants is affected by corrosion and wear products. In metal implants, harmful metal ions arising from corrosion and wear may lead to inflammation, cell apoptosis and other destructive tissue reactions (Biesiekierski et al., 2012; Wu et al., 2013). It was reported that release of Cr (Co-Cr alloys), Nb, V and Ni (Ti-Based) ions may cause detrimental tissue reaction by exceeding concentration of these elements in tissue or body fluid (Biesiekierski et al., 2012; Wu et al., 2013). For instance, Ni is a highly cytotoxic, genotoxic, carciogenic and mutagenic element.

Most of the commercial metal implants are bio-inert, so their biocompatibility depends on the positive response of cells and tissue to the implant surface (Biesiekierski et al., 2012). Thus, the surface characteristics of metal implants are important factors in bone regeneration and biocompatibility (Biesiekierski et al., 2012). However, surface modification may decline the corrosion resistance and mechanical properties.

The most common problem of metal implants is stress shielding. It is a result of great mismatch between elastic modulus of implant and surrounding bone in which applied stresses are taken up by the bone fewer than implant (Biesiekierski et al., 2012; Li et al., 2015). Bone fracture and loosening of implant may occur due to high Young's modulus of metal implants. Among metal implants, Mg alloys have Young's modulus most similar to cortical bone. While the Young's modulus of Ti-based and 316L stainless steel are 110 and 193 GPa, respectively (Biesiekierski et al., 2012; Li et al., 2015).

According to Gibson and Ashbey model, porosity of materials has significant effect on Young's modulus (Biesiekierski et al., 2012). The following formula shows the relationship between porosity and Young's modulus:

$$E_p = E_s C (\rho_p \rho_s^{-1})^2 \qquad (1)$$

Where: E_p is modulus of porous material, E_s is modulus of bulk material, C is a constant depending on pore structure, ρ_p is density of porous material and ρ_s is density of bulk material.

It can be concluded that porous structure can be a solution to decrease probability of stress shielding. Moreover, porous materials with interconnected pores allow new bone formation in growth and also transportation of body fluid. Thus, the porous implant shows better osteoconductivity (Biesiekierski et al., 2012).

1.3 Biodegradable Metal Implants

The new generation of degradable metallic biomaterials is named as a biodegradable metal implant (BMI) (Zheng et al., 2014). This generation of biomaterials exhibits improved corrosion resistance in body fluid during healing process of host tissue. BMIs main duty is supporting of host tissue with a slow corrosion in body fluid, then dissolved completely after healing of host tissue with no implant debris (Cheng et al., 2013; Zheng et al., 2014).

Three factors should be taken into account for selecting composition of BMIs: 1) Metallic elements can be metabolized by the human body, 2) Demonstrate applicable corrosion rate, 3) Demonstrate no toxicity and allergic effect (Francis et al., 2015).

BMIs are classified in three groups: 1) Pure metals, 2) Biodegradable alloys, 3) Biodegradable metal composites (Fig. 6) (Francis et al., 2015). Among BMIs, Mg, Fe and Zn based implants are widely investigated in recent years. These groups of implants are also known as smart implants. The most important problem of this generation is controlling the corrosion rate and maintaining of mechanical integrity in healing period of host tissue (Lévesque et al., 2008). Mg and Fe-based implants show good mechanical properties as a hard tissue implants. However, Mg-based materials high corrosion rate and Fe-based very low corrosion rate limited their application as biodegradable implants. Thus, degradation rate of pure Mg should be improved to use as biodegradable metal implants (Peuster et al., 2006; Lévesque et al., 2008).

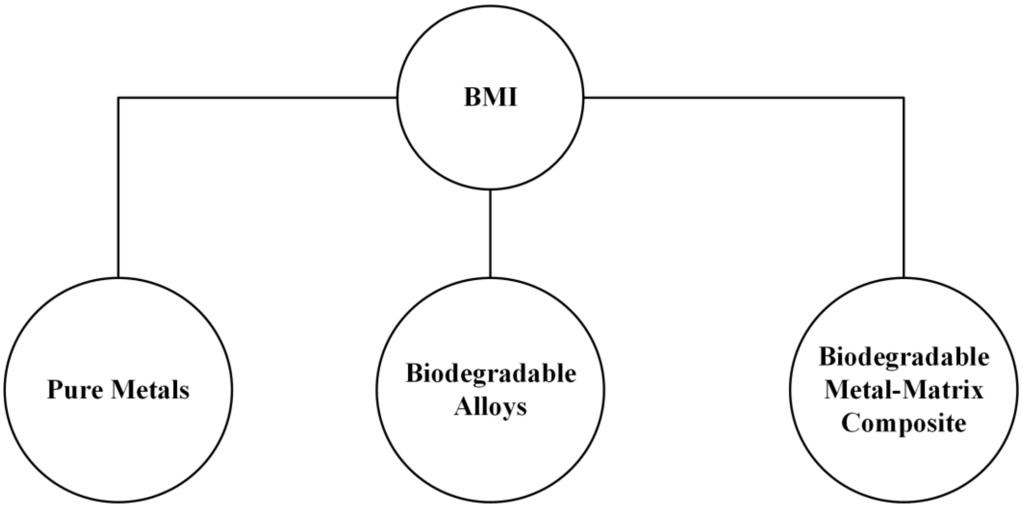

Figure 6: Classification of biodegradable metal implants

1.3.1 Iron-based Biodegradable Implants

Fe-based biomaterials show mechanical properties similar to stainless steel which is used as an inert biomaterial (Table 2). Also, its high modulus of elasticity makes it a good candidate for using as a stent (Moravej et al., 2010; Cheng and Zheng, 2013). Additionally, high ductility can be helpful during implantation of Fe-based stent. However, high corrosion resistance of Fe-based implants is a limitation. The Fe-based stents can remain in the blood-vessel for 20 months after surgery so it behaves like permanent stents (Moravej et al., 2010; Cheng and Zheng, 2013). Another limitation of this generation is their ferromagnetic properties. Mechanical properties, corrosion rate and ferromagnetic properties of Fe-based implants can be improved by alloying, surface modification and heat treatment (Cheng and Zheng, 2013). The common surface modification methods are: 1) Chemical treatment, 2) Powder metallurgy, 3) Electroforming and 4) Inject 3D printing.

Table 2: Mechanical and corrosion properties of iron based implants (Moravej et al., 2010; Cheng and Zheng, 2013)

Composition	Manufacturing Method	Ultimate Tensile Strength (MPa)	Corrosion Rate (mm/year)
Pure Fe	Cast	-	0.008
Pure Fe	Annealed	205	0.16
Pure Fe	Electroformed	423	0.85
Fe-30Mn	Cast	366.7	0.12
Fe-30Mn-6Si	Cast	433.3	0.29
Fe-35Mn	PM	430	0.44

1.3.2 Magnesium-based Biodegradable Implants

Mg and its alloys differ from other biomaterials by presenting compatible mechanical and physical properties to human bone. Their densities and elastic modulus are fairly close to each other which remove elastic mismatches between implants and the bone (Chen et al., 2014; Dorozhkin, 2014). The large difference between elastic modulus can cause the failure of implants called as stress shielding, and subsequently implant loosening (Willbold et al., 2015). Furthermore, Mg is naturally present in bone composition and it is a necessary metal for the metabolism (Saris et al., 2000). However, the fundamental problem of Mg-based implants is their low corrosion resistance showing fast and unexpected degradation behavior within a living system (Fig. 7). Researchers have been trying to enhance the corrosion resistance and to offer an industrial projection of biodegradable implants. Furthermore, it can be said that Mg-based biodegradable implant will shift the direction of medical sector in near future as their commercial products start to appear in the market.

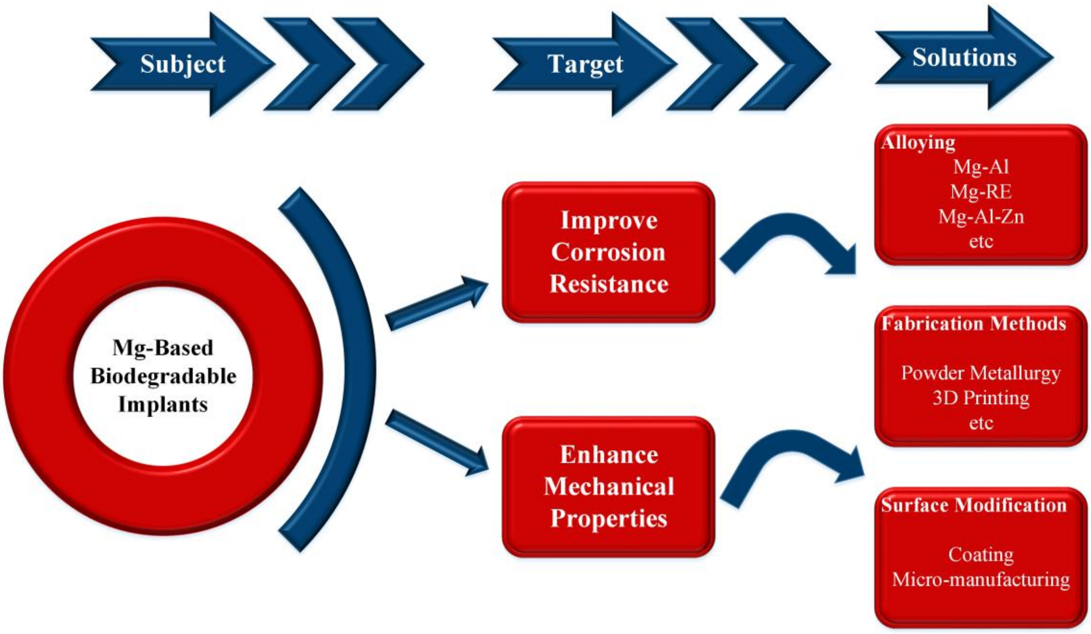

Figure 7: Problems faced and solutions for Mg-based biodegradable implants

To reveal the potential impact of Mg-based biodegradable implants, a comparison between two types of implants will be useful. An elderly person who suffers from bone fracture or damage will be hospitalized twice for insertion and de-insertion, if a non-degradable implant is used. Only one surgery will be needed, in case of biodegradable implants, owing to their absorption after healing process. Each surgical operation implies risk of infection especially for elderly people and can result in fatality. Prolonged hospitalization also increases the risk of health problems and negatively affects the patient’s psychology.

The most important drawback of pure-Mg as a biomaterial is its low resistance to corrosion. The corrosion resistance of Mg alloys has been tried to improve their corrosion resistance (Park and Bronzino, 2002; Quach et al., 2008; Willumeit et al., 2011; Li et al., 2012). For example, the non-soluble toxic oxide of Mg based implants, which is production of corrosion in vivo condition, can be taken out of body with urine.

There are many investigations on different commercial Mg alloys with biomedical purposes after casting and extrusion. Also in addition to commercial Mg alloys, Mg alloys with different elements are produced under laboratory condition and effects of participated elements on mechanical properties, corrosion and cell behavior have been investigated. The studies in the literature on these two different groups are discussed below. Furthermore, Mg is required to improve and replacement of the bone itself continuously. Thus, Mg alloys show great potential for application as biomaterials due to their properties such as light weight, biodegradability, strength under load and the natural decay in a period of 3-4 months in in-vivo condition which is a perfect time for the integration of bone tissue (Witte et al., 2005). However, pure Mg decays very fast, so it is not able to provide necessary mechanical integration during healing of bone tissue (Witte et al., 2005). Therefore, it has been becoming increasingly important to examine Mg alloys and protective coating on them.

AZ31 magnesium alloy (3wt% Al, 1wt% Zn) implants were implanted to sheep hip to investigate different cell behaviors (Willbold et al., 2011). Also, ZK60 magnesium alloy (5.4wt% Zn; 0.5wt% Zr) made by extrusion shows better corrosion resistance than the same alloy obtained by casting (Gu et al., 2011). In addition, this alloy showed corrosion behavior similar to AZ91, AM50, AZ31 and WE43 alloys (Gu et al., 2011). The effect of grain size in in-vitro degradation behavior of AZ91 Mg alloys has been studied and it was proved that the grain size has no significant effect on degradation behavior (Kannan, 2010). In a study investigating WE54 alloy, this alloy showed higher corrosion resistance than pure Mg (Walter and Kannan, 2011). However, this value is lower than the corrosion resistance of AZ91 alloy (Walter and Kannan, 2011). The fatigue resistance of WE43 and AZ91D alloys was measured in synthetic body fluid: AZ91D had a ductile behavior while WE43 was brittle in synthetic body fluid (Peng et al., 2010; Witte, 2010). The different compositions of Mg alloys (Mg-Ce, Mg-Ca, Mg-Li, Mg-Ti, Mg-Pb-Bi, Au-Cu-Mg, Mg-Cd, Mg-Y and Mg-Zn) their production methods, corrosion behaviors and mechanical properties were investigated previously (Park and Bronzino, 2002; Kannan, 2010; Peng et al., 2010; Witte, 2010). It was proved that Li increased the ductility and formability of Mg. Because it transformed the hexagonal close packed structure of Mg to the body centered cubic structure. Addition of Y improves the corrosion resistance and mechanical properties of Mg (Peng et al., 2010; Peng et al., 2011). Hydroxide coating by anodization on the surface of Mg-3.9Y-2.1Nd-0.51Zr alloy increased its corrosion resistance (Quach et al., 2008).

Mg-Li alloys are candidates for future cardiovascular stents due to their good ductility values. However, the presence of Mg-Li binary alloys decrease their mechanical strengths because of the Li. Zhou et al. improved the mechanical properties of this alloy by addition of Al and rare earth (RE) elements (Zhou et al., 2013) . They proved that the microstructure of alloy was changed by increasing the Li content from 3.5 to 8.5 wt. %. The addition of Al improves the tensile strength of this alloy through solid solution strengthening. However, alloying of Mg with RE elements decreases its corrosion resistance due to the presence of intermetallic phases (Zhou et al., 2013).

It was proved that RE elements such as La and Gd improve corrosion resistance of biodegradable Mg alloys. However, good biocompatibility of the elements released by Mg alloys during degradation is essential for their use in an implant (Grillo et al., 2014). It was showed that mechanical properties of Mg alloys were improved by the addition of RE elements due to the formation of metastable RE containing phases along the grain boundaries (Liu et al., 2009; Grillo et al., 2014). Gd higher than 10% increases the mechanical strength because of noble behavior of Mg5Gd precipitated in grain boundaries. Moreover, for Mg alloys containing 15% Gd, an increase in corrosion rate was observed. Addition of La to Mg alloys improves the corrosion resistance by forming a passive film (Grillo et al., 2014). However, there is no in-vitro or in-vivo investigation present on this alloy, which shows the lack of studies in this subject.

Ca increases the strength and corrosion resistance of Mg alloys and decreases the grain size of the alloy. Mg-Ca alloys containing different amounts of Ca are made and it was proved that Mg alloy containing 0.6 wt. % Ca gives better results in terms of corrosion and mechanical properties than Mg alloys with other Ca compositions (Zhang et al., 2011). Increasing the amount of Ca causes the formation of Mg2Ca phase which diminishes the compressive strength, bending strength and lowers the corrosion resistance (Zhang et al., 2011).

Addition of Zr reduces the grain size of Mg which results in improved ductility, smoothened grain boundaries and enhanced corrosion resistance. The ability to absorb huge loads of 1wt% Zr-Mg alloy is better than that of pure Mg (Ramsden et al., 2007). Also, Zr shows good biocompatibility in vivo, low ionic cytotoxicity and an osteocompatibility similar to Ti. Gu et al. proved that Zr higher than 5% led to unalloyed Zr phase in the alloy (Gu et al., 2011). Unalloyed Zr phase led to a decrease in corrosion resistance so subsequently result in poor biocompatibility (Li et al., 2012). As a result, the recommended content of Zr in Mg–xZr–ySr alloys is below 5% (Li et al., 2012). It was proved that the addition of Ca and Zr to Mg-based implants improves osseointegration rate and implant stabilization in host tissue (Mushahary et al., 2014). Mushahary et al. coated the Mg-5Zr-Ca alloy with type-I collagen (Mushahary et al., 2014). They demonstrated that coating of the Mg alloy increases the surface energy and hydrophobicity of this alloy (Mushahary et al., 2014).

It was reported that Sr has a high Mg alloying efficiency and refines grain size in Mg alloys (Li et al., 2012). Additionally, Sr increases the compressive strength, improves biocompatibility and bone formation. However, Sr > 5% in Mg-Zr-Sr alloys leads to Mg17Sr2 phase precipitation in the grain boundary and this intermetallic phase decreases the corrosion resistance. Thus, the level of Sr should be less than 5%. Sr enhances the replication of preosteoblastic cells, and stimulates bone formation.

Previous studies showed that Al has a positive effect on degradation and mechanical properties of Mg alloys. Also, it was proved that Al containing alloys (AZ31, AZ91, LAE442) have acceptable host responses and Al in limited concentrations can be used as an alloying element for Mg alloys as a biomaterial. Willbold et al. proved that Al does not diffuse into surrounding tissue at the degradation stage (Willbold et al., 2015). Also, Witte et al. showed that low amount of Al released during the degradation can be tolerable (Witte et al., 2007). Investigation exhibits that addition of Al up to 3% improves the corrosion resistance and mechanical properties of Mg alloys but addition of Al more than 3% has negative effect on their corrosion resistance (Homayun and Afshar, 2014).

In addition to hard tissue implants, Mg alloys (ZW21) are used as a biodegradable stent for the purpose of treatment for a certain period of time, so Mg alloys are an alternative for 316L stainless steel which is used as a permanent implant (Geis-Gerstorfer et al., 2011; Moravej and Mantovani, 2011). Mg based stents are coated with biodegradable polymers such as PLGA or PLLA to decrease biodegradation rate of the stent (Moravej and Mantovani, 2011). Also, two different Mg alloys (AE21 and WE43) which were implanted to pig's vessel (in-vivo) with temporary condition and biodegradability properties were examined over a period close to 3 months (Hermawan et al., 2010).

The resistance of Mg to biodegradability was increased as a result of the production of a HA-Mg composite (Witte et al., 2007). In addition, osteoblast cells proliferated on the composite surface (Witte et al., 2007). For Mg-Zn-Mn-Ca alloy surface coated with calcium phosphates and calcium silicate composites, the adhesion and proliferation of osteoblast cells are improved (Du et al., 2011). In another study, the corrosion rate of pure Mg was decreased by coating the surface with protein in the growth medium (Willumeit et al., 2011).

1.3.3 Mg-Al Alloys

Al improves mechanical strength of Mg by solid solution strengthening due to high solubility of Al in Mg. The solubility of Al is in the range of 12.7 wt.% at eutectic temperature which results in the formation of α-Mg and γ-$Mg_{17}Al_{12}$ phases in matrix and the minimum solubility is around 2 wt.% at RT (Li et al., 2012; Chen et al., 2014). Among the commercial Mg-Al alloys, AZ91 shows good castability, machinability and acceptable corrosion resistance (Bamberger and Dehm, 2008). For AZ91 alloy, four phase can be seen which are: divorced eutectic α-Mg, primary α-Mg, divorced eutectic β-$Mg_{17}Al_{12}$ and precipitate β-$Mg_{17}Al_{12}$ (Li et al., 2012). Previous studies proved that $Mg_{17}Al_{12}$ is a brittle phase so the plastic deformation of Mg-Al alloys can affected by morphology, distribution, size and amount of this phase (Li et al., 2012). Li et al. showed that formability of AZ91 alloys is improved by fine grain size (around 100μm) and homogeneous distribution of β-$Mg_{17}Al_{12}$ in α-Mg (Li et al., 2012). High mechanical properties were obtained by homogenization of as cast AZ91 at 380ºC for 15h (Li et al., 2012).

It was proved that corrosion behavior and mechanical properties of Mg-Al alloys were improved by grain refinement (Mostaed et al., 2014). In this mechanism, grain size of second phases is decreased and distributed homogeneously (Mostaed et al., 2014). Wen et al. investigated the effect of Al amount on corrosion behavior of Mg-Al based alloys (Wen et al., 2009). Corrosion resistance of Mg-Al alloys in SBF solution is increased by increasing the Al amounts up to 9% (Wen et al., 2009).

Previous studies proved that amount of Al in α-Mg(Al) phases and microstructure have significant effect on corrosion rate of Mg-Al alloys. AZ91D shows lower corrosion rate than AZ31 and AZ61 due to homogeneous and continuous precipitation of β-$Mg_{17}Al_{12}$ along the grain boundaries (Wen et al., 2009). Also, the depth of pits in AZ61 is higher than that of AZ31 because of the formation of more Al_8Mn_5 and β-$Mg_{17}Al_{12}$ (Wen et al., 2009).

1.3.4 Degradation Mechanism of Mg-based Implants

Mg and its alloys degrade through a corrosion process which is an electrochemical reaction (Zheng et al., 2014). The products of this electrochemical reaction are oxides, hydroxides, hydrogen gas and etc. Corrosion mechanism of Mg can be explained as follows:

$$Mg \rightarrow Mg^{2+} + 2e^- \quad \text{(Anodic reaction)} \quad (2)$$

$$2H_2O + 2e^- \rightarrow H_2 + 2OH^- \quad \text{(Cathodic reaction)} \quad (3)$$

$$2H_2O + O_2 + 4e^- \rightarrow 4OH^- \quad \text{(Cathodic reaction)} \quad (4)$$

$$Mg^{2+} + 2OH^- \rightarrow Mg(OH)_2 \quad \text{(Product formation)} \quad (5)$$

The negative difference effect phenomena is observed in Mg corrosion because of high amount of hydrogen gas evolution during anodic reaction. The speed of cathodic reaction declines as a result of this phenomena. Corrosion rate of Mg during anodic reaction is higher than cathodic reaction because of a moderately protective layer formation during cathodic reaction. However, these protective layers are not strong enough and break down before starting of anodic polarization.

Mg and its alloys show unpredictable behavior in physiological environment due to presence of proteins, amino acids and numerous ions (Sanchez et al., 2015). Dissolution rate of Mg and its alloys changes due to adsorption of proteins, amino acids and lipids over the implant surface (Fig. 8) (Yamamoto and Hiromoto, 2009; Zheng et al., 2014). Also, formation of $Mg(OH)_2$ protective layer over the surface of Mg-based implants has significant effect on corrosion rate. However, the high concentration of chloride ions in physiological environment break the $Mg(OH)_2$ protective layer which leads to pitting corrosion. $Mg(OH)_2$ protective films react with chloride ions and produce moderately soluble $MgCl_2$ (Willumeit et al., 2011; Zheng et al., 2014). It was reported that $MgCl_2$ is biocompatible and doesn’t show any toxic reaction in body (Zheng et al., 2014). Moreover, alkalization and the high concentration of calcium and phosphates in biological environment lead to calcium phosphate precipitation on the surface of $Mg(OH)_2$ (Zheng et al., 2014).

Environmental factors such as buffering system, inorganic ions, organic molecules, dissolved oxygen and stress have significant effect on biodegradable behavior of Mg-based implants (Zheng et al., 2014). Presence of organic anions such as Cl^- and SO_4^{2-} negatively affected the corrosion rate of Mg in physiological environment. Cl^- and SO_4^{2-} are aggressive for Mg-based implants and break down protective film on the surface of implant. However, presence of cations and anions such as Ca^{2+} and PO_4^{2-}, and CO_3^{2-} decreased the corrosion rate of Mg by formation of phosphate and carbonate protective layers (Zheng et al., 2014).

The presence of buffering agents such as HCl-Tris and Hepes which are used to neutralize pH value of simulated body fluid, accelerate corrosion rate of Mg-based implants by consuming OH^- ions (Zheng et al., 2014). Thus, consumption of OH^- ions leads to a decrease in corrosion product formation and an increase in corrosion rate. In contrast, protein (Fetal Bovine Serum) adsorption on the surface of Mg implants improves the corrosion resistance (Zheng et al., 2014).

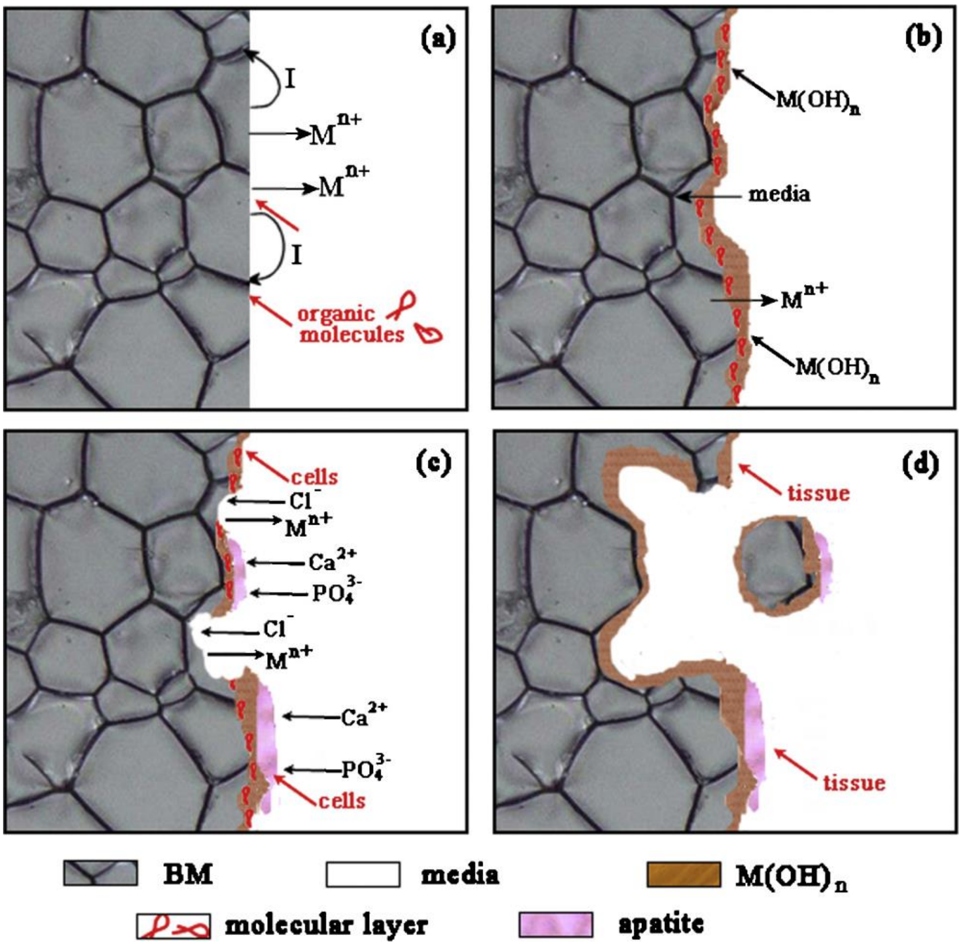

Figure 8: Degradation mechanism of Mg in-vivo (Zheng et al., 2014)

Corrosion behavior of Mg and its alloys is significantly affected by the microstructural defects such as dislocations and deformation twins (Zheng et al., 2015). An increase in residual stress as a result of microstructural defect, led to an increase in corrosion rate (Zheng et al., 2015). The corrosion rate of extruded AZ91 is increased due to an increase in population of dislocations, twins and grain boundaries. Also, mechanical stress has considerable effect on corrosion resistance. Corrosion resistance of Mg-2.65Zn was decreased by increasing the tensile and compressive loading (Zheng et al., 2015). However, intergranular corrosion behavior is different under tensile and compressive deformation.

Four different types of corrosion are likely to occur in physiological environment (Bauer et al., 2013). Galvanic, fretting, pitting and crevice corrosions are most common types of corrosion. Galvanic corrosion is caused by the presence of two metals with different corrosion potential at the same electrolyte. One of the metals acts as anode and the other one acts as a cathode and make a galvanic couple (Bauer et al., 2013). Thus, anode metal is corroded due to electropotential difference between two metals. Probability of galvanic corrosion is high for Mg implant in physiological environment. Micro galvanic corrosion is commonly observed in Mg alloys due to the presence of different alloying elements and phases (Liu and Schlesinger, 2009). For example, presence of α-phase (Mg-Al-Zn), β-phase ($Mg_{17}Al_{12}$), Al, Zn, Mg and other trace elements increase probability of galvanic corrosion in body fluid due to electropotential difference between phases and dissimilar metals (Liu and Schlesinger, 2009). The galvanic corrosion occurred at micro level because of galvanic couple formation.

Pitting corrosion is commonly observed in environments with aggressive ions such as chloride ions in body fluid (Zeng et al., 2006). Pitting corrosion is occurred at regions adjacent to second phases such as $Mg_{17}Al_{12}$ in presence of chloride ions (Zeng et al., 2006). Fretting corrosion occurs on the contact surfaces of metals. This type of corrosion causing a mechanical wear should be considered for Mg-based metal implants (Bauer et al., 2013). The mechanism of crevice corrosion is similar to pitting corrosion and results in localized corrosion on the Mg implant surface. Micro cracks can trigger crevice corrosion (Bauer et al., 2013).

1.4 Biological Properties of Mg

Mg is one of the most important element constructed within the human body and takes place in high number of enzymatic reactions in human body. It was reported that Mg takes place in synthesis process of protein and nucleic acid, stabilization of plasma membrane and many other cellular activity (Walker et al., 2014). Amount of Mg in an average adult human body is around 21-28 g and more than 50% of this amount is presented in bone tissue. Soft tissues contained 35 to 40% of this content and less than

1% is sequestered in serum (Walker et al., 2014). Mg element which is sequestered in bone acts as a reservoir for acute change in Mg levels of serum.

Mg^{2+} bivalent ions play an important role in determining bone fragility. Also, it is known that Mg^{2+} ion takes place in transformation process of immature bone into a mature bone. Mg ion content in bone mineral is around 6 mol% but this content decreases during maturation process of bone. Cartilage and immature bone tissues contain high concentration of Mg^{2+} ion but this concentration changes depending on the aging (Walker et al., 2014). Moreover, presence of Mg in bone composition increases the elasticity of bone (Walker et al., 2014).

Effect of Mg on bone formation was investigated in previous studies. Presence of Mg has significant effect on osteoblastic cell differentiation (Chaya et al., 2015). Bone formation around and over degraded Mg implants proved its effect on accelerating of bone healing (Chaya et al., 2015). Mg degradation led to the release of Mg^{2+} ions to surrounding tissue which resulted in stimulation of local cells to bone formation (Chaya et al., 2015). Also, it was proved that the hydrogen gas which is released during degradation process of Mg and its alloys can be tolerated by human body. However, high amount of hydrogen gas release can result in complication at healing period (Chaya et al., 2015). Thus, the corrosion rate of Mg should be controlled to decrease risk of gas accumulation. The amount of gas cleared from the implantation site also depends on the implanted region and available blood flow (Chaya et al., 2015).

It was proved that presence of Zn in composition of Mg alloys besides improving the mechanical properties and corrosion resistance, increases osteoblastic cell proliferation because Zn takes part in a wide range of physiological functions such as the regulation of immune system and enzymatic reactions (Hong et al., 2013). However, high concentration of Zn resulted in cytotoxic effect in vitro (Hong et al., 2013). Hong et al. proved ZK40-Mg and AZ31-Mg increase cell proliferation in comparison to pure Mg (Hong et al., 2013). High concentration of corrosion products leads to cytotoxic effect in human body due to osmotic shock effect on surrounding cells (Hong et al., 2013). In another study, Mg implant which is alloyed with different amount of Al did not show any cytotoxic or neurotoxic effect up to 9 wt.% of Al.

Moreover, osteoblastic activity was increased with increasing amount of Al up to 9 wt.% so the release of Al ions can be tolerated with human body at small levels (Witte et al., 2005).

1.5 Designing the Surfaces for Bone Implants

Hierarchical structure of bone should be considered in bone implant designs (Bauer et al., 2013; Shibata and Tanimoto, 2015). For instance, human compact bone is a composite material with a hierarchical architecture from macro-scale to nano-scale. Human compact bone can be explained as follows. Osteons are fibers with 200 μm diameter that are composed of parallel lamellae and pores. The lamellae are built of fibers which are built from fibrils. Mineral hydroxyapatite and collagen type I formed a composite at nano-scale. Thus, the wide range of scale should be taken into account to achieve high grade of compatibility with host tissue (Shibata and Tanimoto, 2015).

There are important factors that should be taken into account to improve biocompatibility of implants such as corrosion rate, strength, wear resistance, flexibility or solubility in water (Shibata and Tanimoto, 2015). Moreover, porosity, cavities or channels at micro scale play an important role in cell proliferation and ingrowth into the implant (Shibata and Tanimoto, 2015). As explained, individual surface parameters such as roughness, chemical composition, electrical charge, wettability and crystallinity perform an important role in terms of compatibility (Shibata and Tanimoto, 2015). The most important factor to attain a high degree of compatibility of an implant with host tissue is surface property of the implant. Also, surface properties have a significant effect on stress shielding, wear resistance and fatigue failure. Moreover, implant surface is a predominant factor on success or rejection of implanted material because it is in direct contact with the host tissue surface.

Surface roughness is a key factor for osseointegration rate and mechanical fixation of implant to bone (Deligianni et al., 2001). It was proved that surface roughness at micro-scale range improves the new bone formation rate due to an increase in protein adsorption and cellular activity (Deligianni et al., 2001). van Tol et al. showed that shear strength of bone-implant was increased by increasing surface roughness from 0.058 to 4.25 µm (van Tol et al., 2013). In another study, the bonding strength was increased (0.38-9.70 MPa) by increasing Ra (0.2-4µm) values (Scheerlinck and Casteleyn, 2006). Ra values of Mg plates were measured between 5.66 and 6.44 µm. Previous studies showed that the optimum surface roughness improves the bone-implant bonding strength. Rønold et al. investigated the effect of surface roughness on bone-implant integrity for Ti based implants (Rønold et al., 2003). They showed that the best bone-implant integrity was achieved at Ra=3.90 µm and there is a significant decline in bone-implant integrity by increasing Ra value from 5.07 to 11.03 µm (Rønold et al., 2003). In another study, there was a significant increase in bone cell activity by increasing surface roughness from 0.37 to 3.29 µm (Gittens et al., 2011).

Pore size and pore morphology have a significant effect on cell attachment and proliferation (Lake et al., 2015). It was proved that pores with hexagonal morphology increase cell attachment more than pores with spherical shape (Lake et al., 2015). Also, in-vivo studies showed that the risk of infection decreases by increasing pore size after implantation (0.1 mm) (Lake et al., 2015). On the other hand, increasing pore size negatively affected the mechanical properties of implants. Implants show brittle behavior by increasing the pore size from 100-200 to 350-450 µm. Thus, increasing the pore size declines elastic modulus, shear and compaction strength (Lake et al., 2015).

Combination of random macro, micro and nano-scale roughness on implant surface improves the integrity between implant and host tissue (Prodanov et al., 2013). Roughness on surface of an implant increases the protein accumulation and as a result improves cell attachment (Prodanov et al., 2013). Thus, mimicking the bone surface with micro and nano texture may promote osteointegration due to increase in mineral deposition (Sato et al., 2009). Prodanov et al. manufactured three different pattern surfaces (150, 300 and 1000 nm) (Prodanov et al., 2013). In vitro results proved that the best mechanical integrity was achieved on the surface with 300 nm roughness (Prodanov et al., 2013).

Branemark et al. modified the Ti surface by using laser technology (Brånemark et al., 2011). It was reported that the rate of new bone formation at contact region increases due to bone bonding at nano level (Brånemark et al., 2011). Also, pore size has a significant effect on in-vivo behavior of Ti implant. Shear stress was increased by increasing pore size from 100 to 200 µm while by increasing pore size from 200 to 300 µm, it was declined (Brånemark et al., 2011).

The optimum surface roughness should be found to increase cell attachment but it is not predominant factor in cell integration (Mirhosseini et al., 2007). The optimum size for roughness may depend on actual size of cell used in in-vitro studies (Mirhosseini et al., 2007). Mirhosseini et al. investigated the effect of laser patterning on cell attachment for Ti6Al4V implant (Mirhosseini et al., 2007). The patterned surfaces improve 2T3 osteoblast cell growth and uniform cell attachment (Mirhosseini et al., 2007). While, smooth surface cells accumulate on the implants in region which is near to the center of seeding (Mirhosseini et al., 2007).

1.6 Aim of the Study

In this study, it is aimed to design, develop, manufacture and validate biodegradable Mg-based porous bone implant with micro-textured surfaces by using PM manufacturing method. Box-Behnken design (BBD) was used to define the effects of manufacturing parameters on material characteristics and optimal parameter values of process conditions. Response Surface Methodology (RSM) was also used to present the effects of parameters for further understanding. The main objectives of this study are:

- Control the corrosion rate of Mg plates by surface modification.
- Investigate the effect of different media on corrosion behavior.
- Find a robust and repeatable manufacturing procedure and testing methods to characterize the material behavior at different manufacturing conditions.
- Investigate the effect of surface structure on biological response.

CHAPTER 2

MATERIALS AND METHODS

2.1 Mold Designing and Fabrication

A new mold was designed, according to production method used in this study. The new mold system is seen in Figure 9. A 3D solid mold was designed by using SolidWorks 2013 program. Technical drawing of mold is shown in Figure 9b.

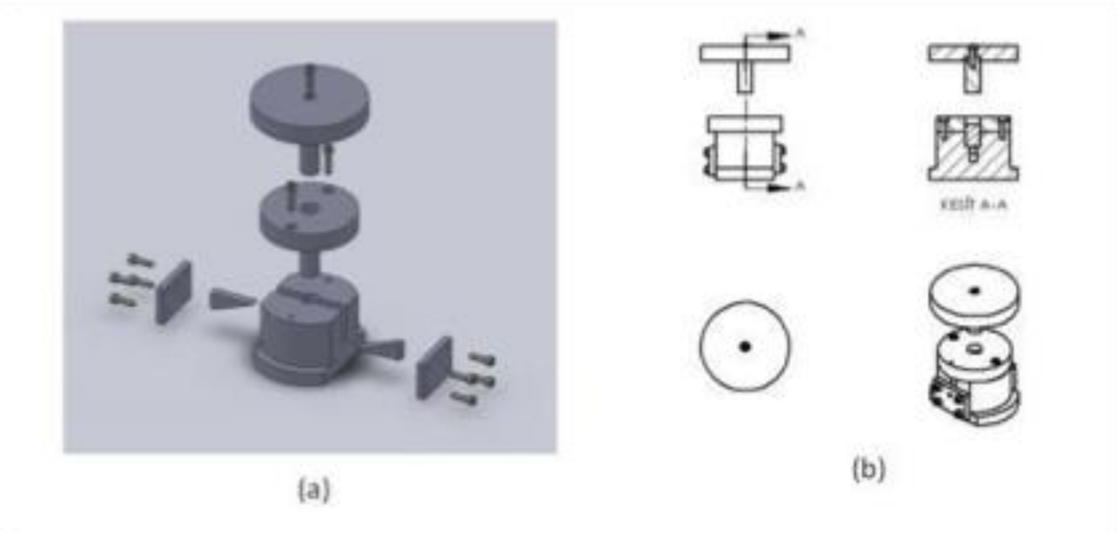

(a)

(b)

Figure 9: 3D image of mold system (a), Technical design (b)

In order to fabricate micro-textured porous biodegradable implant samples using Mg powders via powder compaction method, first, micro-textured die/mold surfaces on tools steels (H13) was designed and machined (Fig.10). Purpose of micro surface design is: improving the cell adhesion on the surface of implant so indirectly decline corrosion rate of implant. The most important factor which should be taken into account in designing mold surface is aspect ratio. Low aspect ratio can result in decreasing cell proliferation due to not reaching of enough oxygen to cells. On the other hand, cell attachment decreases for high aspect ratio.

Previous studies proved that optimum surface roughness, porosity and surface texture should be selected to improve cell attachment and proliferation (Fu and Soboyejo, 2009). Fu and Soboyejo showed that micro-texture between 10-120 μm increased the cell adhesion on the surface of implant (Fu and Soboyejo, 2009). Also, porosity play an important role in cell attachment, proliferation and bone-implant integrity (Fu and Soboyejo, 2009).

In mold surface design, aspect ratio was selected as 5/4 due to reasons mentioned above (Fig. 10b). Opening between micro-textures is 200 μm while the maximum depth is 160 μm.

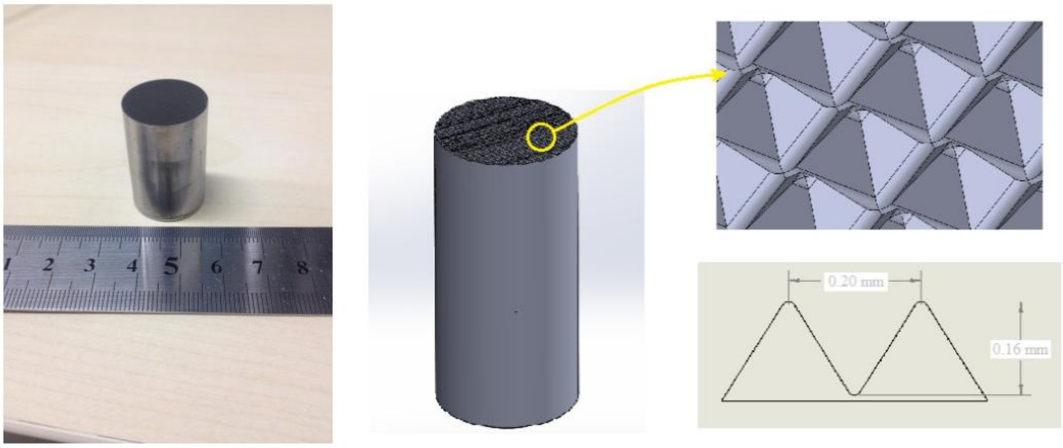

(a) (b)

Figure 10: Mold used in surface modification; Image of mold (a), Schematic design of mold

2.2 Design of Experiment

Design of experiment (DOE) is a branch of statistic which is used in experimental studies to 1) planning, 2) executive, 3) collecting results and 4) explication. The variables that have an impact on the results or set of variables and interactions between them can be determined by DOE (Montgomery, 2008). The most important feature of DOE is reduced number of experiments which provides more accurate results. Thus, the impact of variables on results can be determined more accurately and precisely with fewer number of experiments.

Box-Behken DOE method is used to evaluate effect of variables and test condition on results more precisely and reduce the number of experiments. This method has a pattern in which the assay varies according to factor number and level. The DOE with 3 variables and 3 level used in this study is shown in Figure 11. Level of variables are shown with '-1', '0', and '1'. The smallest value is expressed by '-1' while '1' is responsible to largest value. The main difference of this method with full factorial method is the combination of selected experiments done instead of entire probabilities. Thus, this method helps to save time and materials.

Experiments	Variables		
	X_1	X_2	X_3
1	-1	-1	0
2	-1	1	0
3	1	-1	0
4	1	1	0
5	-1	0	-1
6	-1	0	1
7	1	0	-1
8	1	0	1
9	0	-1	-1
10	0	-1	1
11	0	1	-1
12	0	1	1
13	0	0	0
14	0	0	0
15	0	0	0

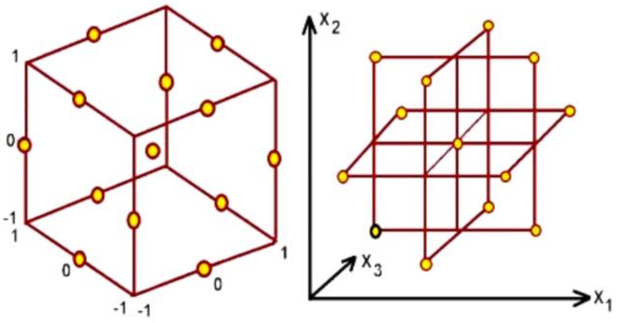

Figure 11: Box-Behken design of experiment

Impact of different variables (Compaction pressure, compaction temp., sintering temp., sintering time and aging, etc) was investigated during feasibility study. Compaction pressure, sintering temperature and time were selected among other parameters due to their significant effect on properties of final product. The variables and their levels are shown in Table 3.

Table 3: Variable levels of Box-Behken DOE

Variables	Variable Levels		
	-1	0	1
Compaction Pressure (MPa)	150	200	250
Sintering Temp. (ºC)	380	400	420
Sintering Time (min)	60	180	300

The effect of compaction pressure, sintering temperature and time on corrosion rate, porosity and bending strength were investigated. The combination of the variables in each experiment is presented in Table 4.

The effective variables are selected by consideration to results which are obtained from porosity, corrosion rate and bending strength and new design of experiment by using full factorial method. Thus, the further and precise statistical analysis may be done by reducing the number of variables. The full factorial DOE is shown in Table 5. The compaction pressure was selected as 250 and 300 MPa to increase corrosion resistance and mechanical strength of manufactured samples. Also, Mg plates with two different surface morphology (smooth and micro-textured) were selected to investigate the effect of surface modification on cell attachment and differentiation. Additionally, effect of sintering time on porosity is investigated. Compaction and sintering temperatures were constant for all of the samples which were manufactured by using full factorial method. Table 6 shows the experimental conditions used in cell culture experiments.

Table 4: The 3 variable and level Box-Behken experimental design

No.	Variables		
	Compaction Pressure (MPa)	Sintering Temp. (ºC)	Sintering Time (min)
1	150	400	60
2	150	400	300
3	250	400	60
4	250	400	300
5	150	380	180
6	150	420	180
7	250	380	180
8	250	420	180
9	200	380	60
10	200	420	60
11	200	380	300
12	200	420	300
13	200	400	180
14	200	400	180
15	200	400	180

Table 5: Full factorial design of experiment

Variables	Variables Level	
P1: Compaction Pressure (MPa)	250 (-)	300 (+)
P2: Surface	Smooth (-)	Textured (+)
P3: Sintering Time (min)	60 (-)	180 (+)
* (1) Sintering Temperature: 380ºC, (2) Compaction Temperature: 150ºC		

Table 6: Full factorial design for cell culture tests

#	P1	P2	P3
C1	+	+	+
C2	+	+	-
C3	+	-	+
C4	+	-	-
C5	-	+	+
C6	-	+	-
C7	-	-	+
C8	-	-	-

Variance analysis (ANOVA) statistical method was used to investigate impact of variable used in full factorial DOE method on biocompatibility and cell behavior. The significance of variables to consider their impact on the cell behavior can be understood accurately by variance analysis. Also, the effect of variables on each other can be determined by using this method (Ahmed and Rashed, 2014). In all statistical analyzes, $\alpha = 0.05$ significance level (95% confidence interval) was used.

2.3 Powder Metallurgy

2.3.1 Powder Compaction and Surface Modification

Mg-AZ91 powders are compacted in order to create the desired surface structure and obtain adequate mechanical strength. Powders are compacted according to design of experiment which is explained before. DARTEC universal tension and compression system with maximum capacity of 600 kN was used in compaction of the samples (Fig. 12). The machine was controlled by a computer based system during loading.

Figure 12: Dartec universal testing machine and control unite

System which is used in micro-deformation procedure is shown in Fig 13. Also, compaction mold and temperature control unit are seen in Fig. 13. Compaction mold is made of three different parts which are: support reservoir, upper and lower molds.

Figure 13: The die system used in surface modification

The temperature control unit was used to heat and stabilize temperature during compaction procedure. The mold temperature control with two k-type thermocouples which are able to measure temperatures in the range of -110 and 1300°C. Moreover, upper and lower modes were heated by two resident chamber and these chambers are controlled by a temperature control unit (Fig. 14).

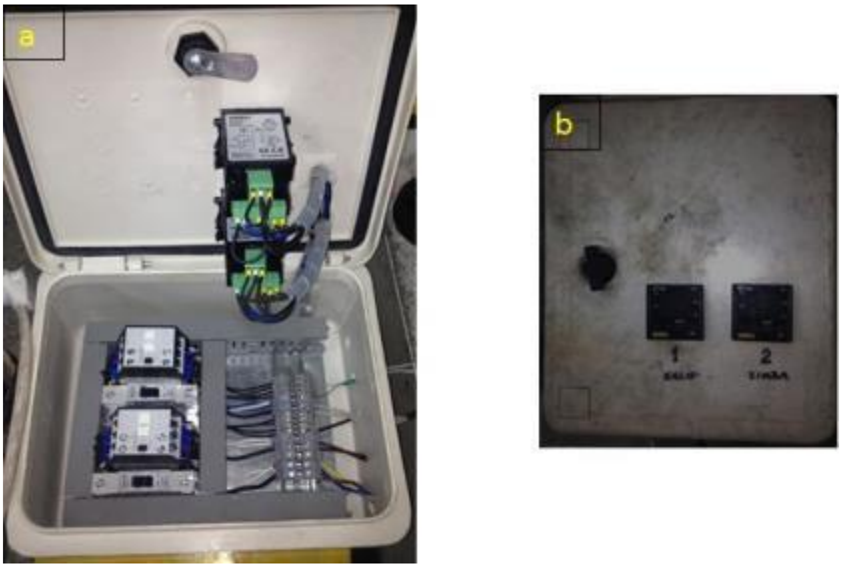

Figure 14: Controlling unit of heating chambers

The support reservoir was located into lower mold before starting of compaction stage. Then, by adjusting the height of mold powder is poured into the mold and upper mold is located over the powder. Finally, the mold was heated by using temperature control unit and load was applied.

2.3.2 Sintering of Green Compacts

Main purpose of sintering is improving the mechanical properties of green compacted plates. Powder particles are mechanically bonded during compaction process but sintering provides activation energy to diffusion of particles, participation of metallic or intermetallic phases and rearrangement of crystallographic structure (Fan et al., 2013).

The factors should be taken into account in sintering process are: 1) sintering temperature (supply enough activation energy), 2) sintering time, and 3) sintering environment (Jabur, 2013). These factors have momentous effect on mechanical properties of compacted materials.

Sintering temperature was selected by consideration to Mg-Al binary phase diagram (Fig. 15). Solid solution sintering method was selected for the sintering of green compacted plates. Sintering temperature of AZ91D-Mg alloy must be selected in the range of 330 and 520°C to have successful sintering process. Three different sintering temperatures (380, 420 and 480°C) were selected to explore effect of sintering temperature on mechanical, crystallographic properties and corrosion behavior of AZ91D-Mg alloy.

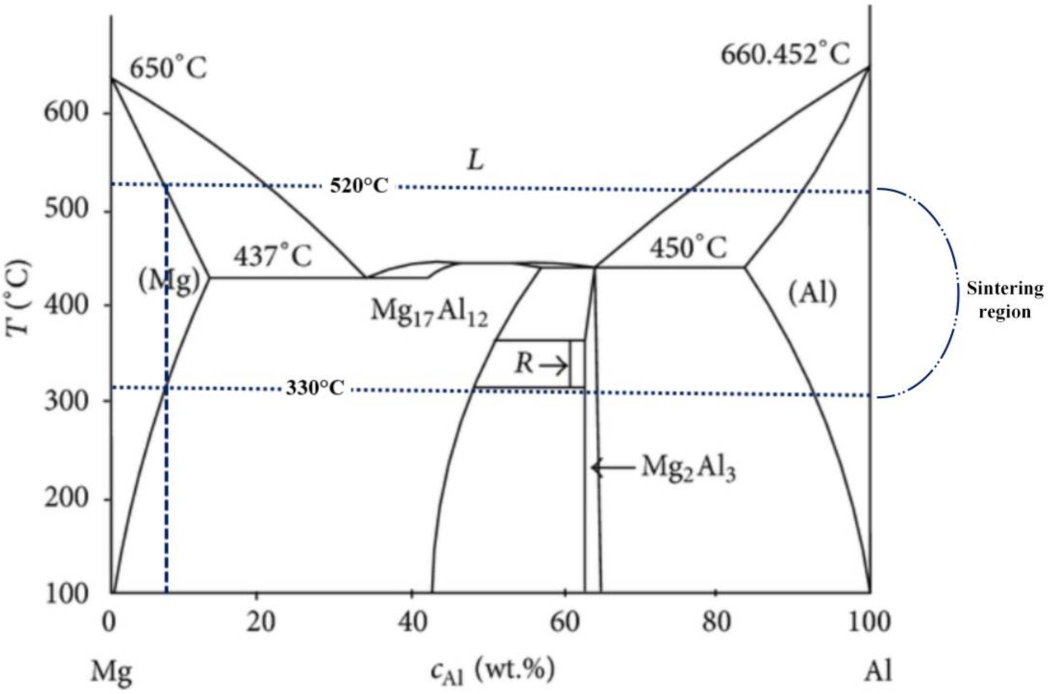

Figure 15: Mg-Al binary phase diagram (Liang et al., 1998)

Green compacted plates were sintered in a MTI quartz tube furnace (GLS-1200X, MTI, USA) with a maximum heating capacity of 1200°C and heating rate of 10°C/min (Fig. 16). Furnace was controlled by a computerized controlling unit. Plates were sintered at 380, 400 and 420°C for 60, 180 and 300 minutes. Sintering environment was 95% N_2 + 5 H_2 which provides an inert atmosphere and significantly decreases the oxidation risk. It is known that Mg is a highly active element and sintering environment must be controlled to prevent alloy from oxidation. Effect of sintering parameters on physical and mechanical properties of AZ91D-Mg was investigated in this study.

Figure 16: Sintering quartz tube furnace

2.4 Structural Analysis

2.4.1 X-Ray Diffraction (XRD)

Phase analysis of as received powder and sintered powders was done by XRD (Rigaku Ultima-IV). XRD was performed on the samples with Cu-Kα radiation at 40 kV/40 mA. Samples were scanned from 20 to 90 with 2θ angles with a scan speed of 2.0^o/min. Results obtained from XRD were compared with Joint Committee on Powder Diffraction Standards (JCPDS) in order to determine the possible phases.

2.4.2 Particle size and Size Distribution

Particle size and size distribution were defined by a particle sizer machine (Malvern Instruments Ltd., Worcestershire, UK). There are many methods which are used to determine particle size and distribution. Mie theory is one of the most used methods. In this method, beams are scattered from solid or some of liquid objects and the relationship between grain size and scattering angle is defined.

2.4.3 Scanning Electron Microscopy

SEM analysis (QUANTA 400F, FEI Ltd., Oregon, USA) was done for as received powders and samples after sintering to investigate powder morphology and formation of micro-texture on the surface of samples. Also, SEM-EDX was applied for elemental analysis of implant surfaces after immersion and electrochemical test. Moreover, cell morphology was investigated by SEM.

2.4.4 Surface Area Analysis

Brunauer-Emmett-Teller (BET) method was used to calculate specific surface area of as-received powder and compacted plates. Specific surface area of material was measured by consideration to physical adsorption of gas molecules (such as nitrogen) on the surface of material. BET analysis was conducted at 150°C for 1 hour under nitrogen environment by Autosorb-6 surface characterization machine (Quantachrome Corporation, USA).

2.4.5 Confocal Microscopy

Surface topographies of the insert and Mg alloy discs were displayed by employing confocal laser scanning microscopy in order to verify the applicability of intended surfaces to manufacture. Surface roughness parameters were measured and compared to the surface of the insert. Four different parameters used to display surface parameters (Fig. 17) and the meaning of parameters are presented in Table 7. Images and surface roughness parameters were captured by a Zeiss Laser Scanning Microscope (LSM 510, Zeiss GmbH, Germany).

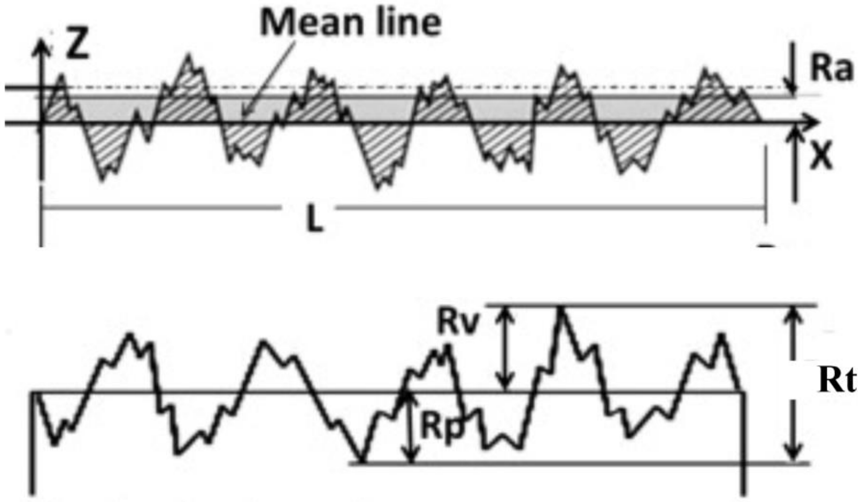

Figure 17: Schematic of surface roughness (Kumar et al., 2014)

Table 7: Explanation of parameters used in confocal microscopy (Kumar et al., 2014)

Symbols	Explanations
Ra	The integral of absolute value of surface profile roughness. It is obtained by dividing scanning area to L
Rt	Sum of the maximum depth and height in their entire length measured
Rv	Maximum depth in surface profile
Rp	Maximum height in surface profile

2.4.6 Relative Density

Density of AZ91D-Mg plates was calculated by dividing the mass by volume ($\rho = m/v$). Relative density of plates was calculated by dividing apparent density to theoretical density of AZ91D-Mg plates (1.82 g/cm^3) (Yamada et al., 1999). The effect of manufacturing parameters on relative density of plates was investigated.

2.5 Mechanical Test

2.5.1 3-point Bending Strength

3-point bending test is used for mechanical characterization of sintered plates. Fig.18 shows a schematic of 3-point bending test. Three-point bending tests were conducted using a universal testing machine (LS 500, Lloyd Instruments, UK). An adjustable gauge with a 2.5kN capacity was used as a measurement device. Force was applied to the middle of the samples and a computer controlled the data acquisition system during experimentation. The bending strength values in MPa are calculated by the following equation.

$$\sigma = (3Fl) / (2bh^2) \qquad (6)$$

Where F is the fracture force in Newton; l is the test span (the distance between supporters) in millimeters; b is the width of the specimen in millimeters; h is the thickness of the specimen in millimeters.

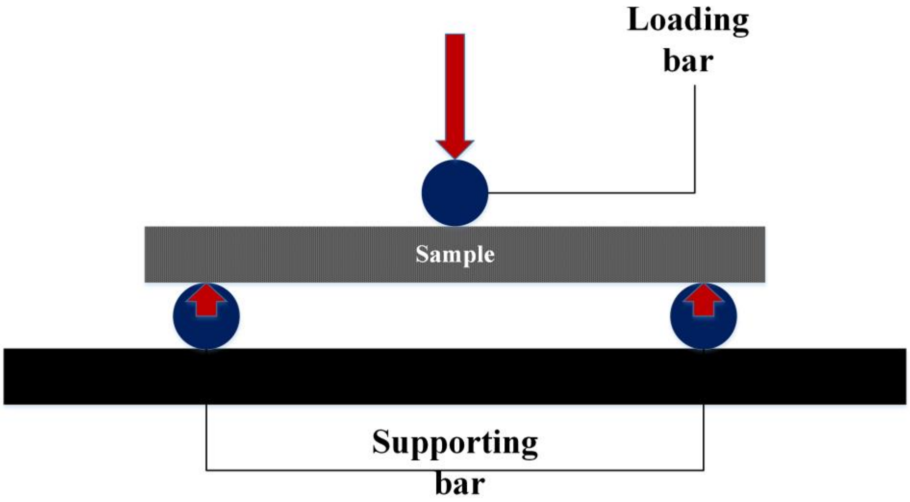

Figure 18: Schematic presentation of 3-point bending system

2.6 Corrosion Analysis

2.6.1 Electrochemical Tests

Electrochemical tests were conducted by using a three electrode cell system. Saturated calomel was used as a reference electrode while auxiliary electrode was graphite (Fig.19). Electropotential difference between reference electrode and working electrode was measured by using Potentiostat and data was analyzed by using a computer program. Potentiostat must be calibrated before each test. System was calibrated by using a calibration box which is a smart electronic brain. Crocodile connected to this box then calibration started to remove noise and standardizing of system which will able to compare data with previous studies.

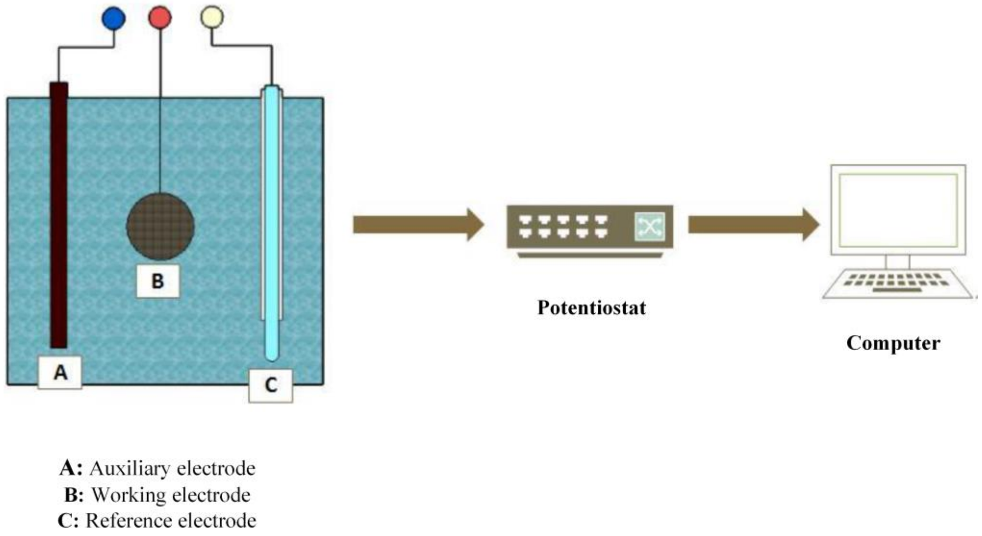

Figure 19: Schematic design of electrochemical analysis

Stabilization voltage range was determined by using Potentiodynamic tests in electrolyte (Table 8). Open circuit test was applied for 1h before starting of Potentiodynamic test which was used in determination of corrosion potential.

Electrochemical scan was performed between -800 mV and 1000 mV with a scanning rate of 0.1667 mV/s. Curves obtained from electrochemical test were compared and Tafel analyzing was applied to determine of corrosion rate of samples. Corrosion resistance was calculated by a software supplied by Gamry instruments. A three electrode cell system (Interface 1000, Gamry Instruments, USA) composing of working electrode, auxiliary electrode and reference electrode was used for electrochemical evolution of the samples. The working electrode (Mg plate) was coated with a dielectric polymer and just 1 cm^2 of working electrode was exposed to electrolyte. Samples were gently washed with deionized water and 99.9% alcohol, dried at 37°C at the end of the electrochemical tests.

Table 8: Chemical composition of solutions used in electrochemical tests (Gu et al., 2011)

Composition	Hank Solution	DMEM(L)	DMEM(L) + 10% FBS
NaCl	136.75	109.4	109.4
KCl	5.37	5.37	5.37
$CaCl_2$	1.85	1.8	1.8
$NaHCO_3$	3.15	44.05	44.05
K_2HPO_4	0.42	–	–
NaH_2PO_4	0.65	1.04	1.04
$MgSO_4$	0.81	0.81	0.81
Glucose	5.55	5.55	5.55
Amino Acid	–	11.01	11.01
Fetal bovine serum	–	–	10%

2.6.2 Immersion Tests

Immersion test is used to investigate degradation behavior of materials. There are two types of immersion test which are static and dynamic. In both of these methods, the solution concentration and immersion time have significant effect on corrosion rate (Boland et al., 2013).

The simulated body fluid (SBF) was prepared in order to use in immersion test. The SBF was prepared according to Table 9.

Table 9: Simulated body fluid (SBF) (Zafari et al., 2014)

	Chemical	**Weight (g l^{-1})**
1	NaCl	8.035
2	$NaHCO_3$	0.335
3	KCl	0.225
4	$K_2HPO_4.3H_2O$	0.231
5	$MgCl_2.6H_2O$	0.311
6	$CaCl_2$	0.292
7	Na_2SO_4	0.072
8	Tris $(HOCH_2)_3CNH_2$	6.228

SBF preparation procedure was carried out according to the following seven items.

1. Plastic containers with a smooth surface is preferred in the solution preparation. The glass containers are not preferred because any scratch on the surface of glass leads to apatite precipitation.
2. The reagent solution was added simultaneously.
3. The SBF temperature was maintained at 37 ± 0.5°C throughout the preparation.
4. Tris was added after solution of other 6 reagents.

5. The pH of solution was adjusted to 2±0.1 before starting the addition of Tris. The pH is gradually raised to 7.45 by addition of tris to solution.
6. The addition of Tris was stopped after raising the pH to 7.45 ± 0.01 level. The pH of solution was dropped to 7.42 ± 0.01 by addition of 1M HCl.
7. The remaining Tris and HCl were added to solution gradually to keep the pH level between 7.45 ± 0.01 and 7.42 ± 0.01.

Fabricated samples were immersed in SBF for 8 days. SBF was renewed every two days and then the samples were washed with distilled water and dried before weighting. The corrosion rate was calculated according to following formula:

$$\nu_{corr} = (M_o - M_1)/(St) \qquad (7)$$

Where: M_o is weight before immersion, M_1 is weight after immersion, S is surface area and t is immersion time.

Also, the morphology of corroded samples was investigated by using SEM. EDX was used to determine apatite precipitation on the surface of plates.

2.7 Cell Culture Studies

2.7.1 Cell Proliferation

h-FOB (Human Fetal Osteoblastic) cells were seeded on AZ91D-Mg plates which were designed according to full factorial DOE method. Plates were sterilized with 25 kgray gamma irradiation before seeding. The h-FOB cells were grown in DMEM/HAM’s F12 (Gibco Life Technologies, UK) with 15% fetal bovine serum (FBS) (Merck Millipore, Germany) and 0.1% penicillin-streptomycin (Merck Millipore, Germany). The initial cell seeding density was 30000 cells/cm^2. Cells were incubated on AZ91D-Mg plates for three different time periods: 1, 3 and 7 days at

37°C under 5% CO_2 humidified environment in a carbon dioxide incubator (5215, Shel Lab., USA) and the medium was refreshed every 2 days.

Proliferation of the cells on the plates was investigated by Presto Blue (Life Technologies, UK). The cell seeded plates for each time point are incubated at 37°C under 5% CO_2 humidified environment for 23 h after adding presto blue. The absorbance of samples were measured by a μOuant^{TM} microplate spectrophotometer (Biotek Instruments Inc, USA). The excitation and reference wave lengths are 570 and 600 nm for presto blue, respectively.

The absorbance values were normalized with using the values obtained from excitation with reference wave length. The percent reduction of presto blue was calculated to determine percent of alive cells according to following formula:

$$\text{PrestoBlue reagent percent reduction (\%)} = (((O2*A1) - (O1*A2))/ ((R1*N2)-(R2*N1)))*100 \quad (8)$$

Where:

O1 is molar extinction coefficient of oxidized presto blue reagent at 570 nm

O2 is molar extinction coefficient of oxidized presto blue reagent at 600 nm

R1 is molar extinction coefficient of reduced presto blue reagent at 570 nm

R2 is molar extinction coefficient of reduced presto blue reagent at 600 nm

A1 is absorbance of test wells at 570 nm

A2 is absorbance of test wells at 600 nm

N1 is absorbance of media only wells at 570 nm

N2 is absorbance of media only wells at 600 nm

2.7.2 Morphology of Cells

The morphology of h-FOB cells seeded on AZ91D-Mg plates was analyzed by SEM (QUANTA 400F, FEI Ltd., Oregon, USA) after 1 and 7 days. Cells must be fixed before SEM analysis. The medium was removed and the plates were soaked in 2.5% glutaraldehyde for 2 h. following to this step, the plates were rinsed with cacodylite buffer (0.1M pH:7.4) and dehydrated with increasing ethanol-deionized water solution series (30, 50, 60, 70, 80, 90 and 100%). In the final step, the plates were immersed in hexamethyldisilazane (HMDS) for few seconds and dried to obtain better resolution. The plates were coated with Au-Pd with a thickness of 10 nm just before SEM.

2.7.3 Confocal Microscope Analysis of Cells

The morphology of h-FOB cells seeded on AZ91D-Mg plates was analyzed by laser scanning confocal microscope (Zeiss LSM 510, Zeiss ltd., Germany) after 1 and 7 days. The cells were fixed and stained by phalloidin-FITC (Life Technologies, Thermo Fisher Scientific, USA). The stock solution of phalloidin-FITC was prepared in methanol or DMSO at 0.1-5 mg/ml. The seeded plates were washed with PBS and then fixed with 4% formaldehyde for 10 min. Following to this step, plates were soaked to PBS and dehydrated with 0.1% Triton X-100 in PBS for 10 min and washed with PBS after dehydration step. The staining of cells should be done in dark room. The seeded cells were stained with phalloidin-FITC (50 μg/ml) at room temperature for 40 min. In final step, the stained cells must be washed with PBS for three time.

2.7.4 Alkaline Phosphate Assay (ALP)

h-FOB cells were seeded on AZ91D-Mg plates with a seeding density of 30000 cells/cm^2. The seed plates incubated for 3 different (1, 5 and 10 days) time periods. The cells were grown in differentiation medium which composed of DMEM/HAM's F12 with 15% FBS, 0.1 % penicillin-streptomycin, 50μg/ml ascorbic acid, 10 mM β-glycerophophate and 10-8 M dexamethasone. The differentiation medium was renewed every 2 days. The cells seeded on the plates were lysed with 600 μl of 0.1% Triton X-100 (composed of 0.1% w/v sodium azide and 1% protease inhibitor) in PBS on ice. The lysed cells were kept on ice for 60 min and then thawed. The collected lysates diluted with differentiation medium and then 20 μl of the diluted solution added into 100 μl p-nitrophenyl phophate (pNPP) substrate solution and incubated at 37°C for 1 h under 5% CO_2 humidified environment. pNPP was converted into p-nitrophenol and an inorganic phosphate due to the intracellular ALP enzyme activity during incubation period. The reaction is represented in Figure 20:

p-nitrophenyl phosphate $\longrightarrow$ *p*-nitrophenol + phosphate

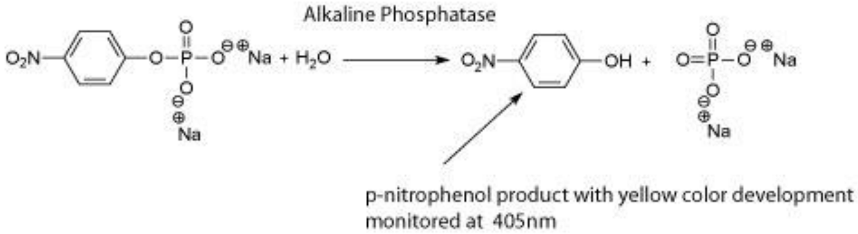

Figure 20: Reduction of p-nirophenyl phosphate to p-nitrophenol (Lozzi et al., 2008)

μOuantTM microplate spectrophotometer was used to read the absorbance of each lysate at 405 nm. According to calibration curve which is constructed in the range of 25-250 μM (Appendix). Protein content of each sample was used to normalize its ALP activity. The specific ALP activity was stated as nmol/μg protein/min. For this procedure, the substrate solution was prepared by mixing 1ml of copper sulfate solution (2 g cupric sulfate in 50 ml water) with 50 ml of BCA reagent. 50 μl of each cell lysate was added into 1 ml of copper sulfate-BCA mixture and the absorbance was read at 562 nm with a μOuantTM microplate spectrophotometer after 30 minutes of incubation. The protein content of each cell lysate was determined according to the calibration curve obtained with bovine serum albumin (BSA) in the range of 0-1.2 mg/ml.

CHAPTER 3

RESULTS AND DISCUSSION

3.1 Structural Analysis

3.1.1 XRD Analysis

XRD analysis was applied to as-received powder and powders which were sintered at three different temperatures (380, 400 and 420°C) for 5 hour to investigate the effect of sintering. Corresponding to Figure 21, XRD patterns of all of samples were matched with JCPDS files for α-Mg (JCPDS 04-0770), β-$Mg_{17}Al_{12}$ (JCPDS 1-1128) and CaO (JCPDS 37-1497) which is similar to XRD pattern of AZ91D-Mg alloy (Miyazawa et al., 2004).

It is clearly seen that crystallinity increased after sintering of as-received powder and also intensity of β-$Mg_{17}Al_{12}$ increased during sintering process in which the highest intensity of β-$Mg_{17}Al_{12}$ was achieved for powder sintered at 380°C. The presence and distribution of β-$Mg_{17}Al_{12}$ play an important role in corrosion behavior of AZ91D-Mg alloy (Zhang et al., 2013). Intensity of β-$Mg_{17}Al_{12}$ peaks was decreased by increasing sintering time due to solution of intermetallic phase (Smith et al., 1998).

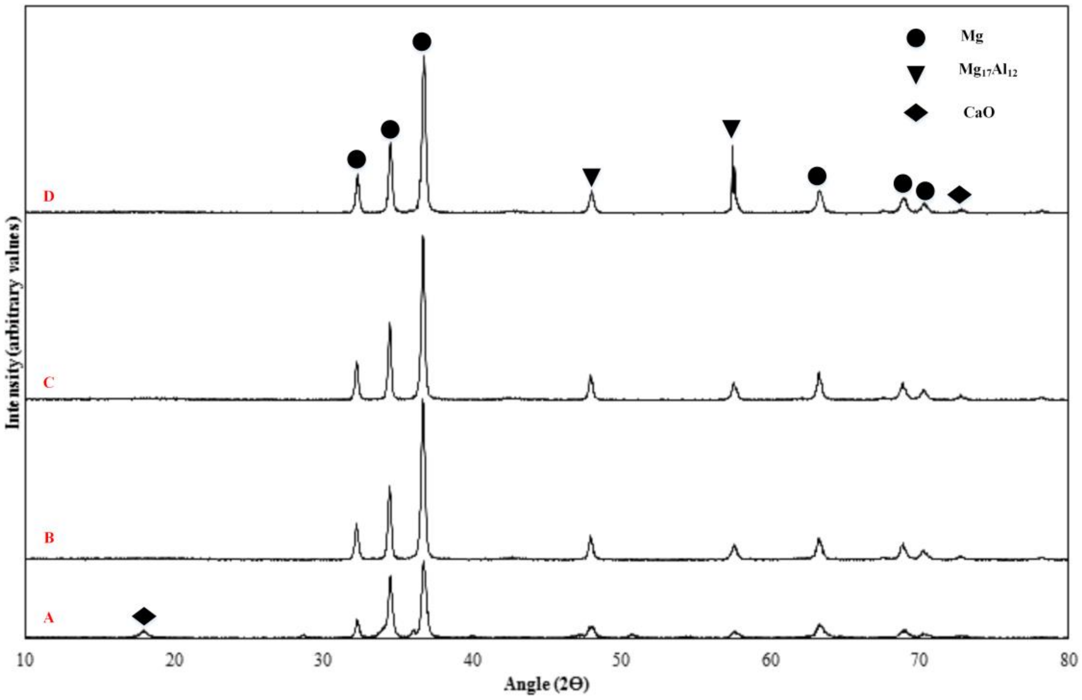

Figure 21: XRD patterns of (A): As-received powder, (B): Powder sintered at 420°C for 5h, (C) Powder sintered at 400°C for 5h and (D) Powder sintered at 380°C for 5h.

3.1.2 Particle Size Analysis and Powder Morphology

Particle size measurement showed that average particle size was approximately 107 µm and powder particle sizes mainly ranged from 50 µm to 614 µm (Fig. 22). d-values of the powders were measured as d10=50, d50=177 and d90=614 µm. Figure 23 exhibits the metal powders with irregular shapes and it can be understood that they were manufactured by mechanical grinding.

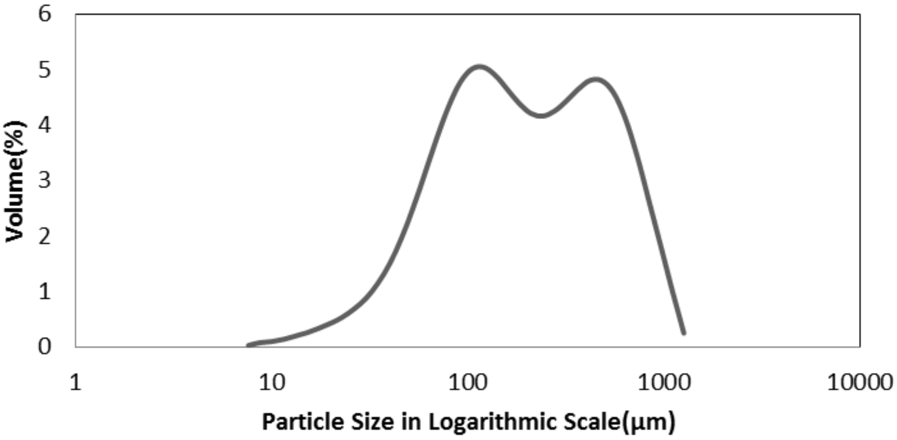

Figure 22: Particle size distribution of AZ91D-Mg

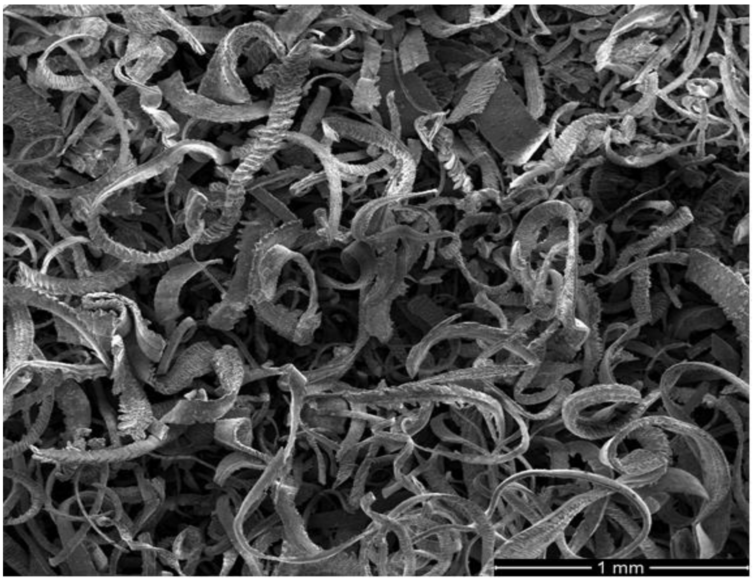

Figure 23: SEM images of as received powders

3.1.3 SEM Analysis

SEM images of some samples after compaction and sintering process are given in Figures 24 and 25. SEM images clearly showed the formation of micro-textures on the surface of plates. Also, the metal powders are bonded together after compaction and sintering. Moreover, it was clearly seen that the powders are not formed layer by layer structure and particles diffused to each other at the end of manufacturing process. Thus, the compacted powders are diffused and overlapped in sintering process (Exner and Arzt, 1990). As it was discussed before, the diffusion and overlapping of particles have significant effect on density, pore size and mechanical behavior of final products.

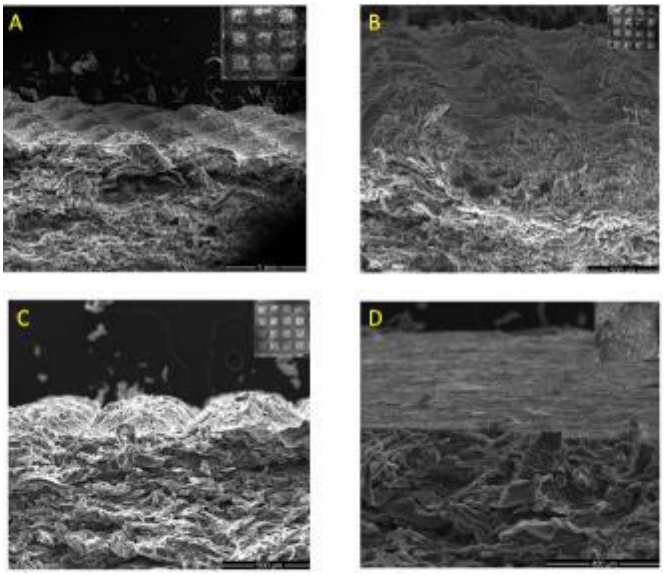

Figure 24: SEM images of AZ91D-Mg plates: A) Compacted under 150 MPa at 400℃ for 1h; B) Compacted under 150 MPa at 380℃ for 3h; C) Compacted under 250 MPa at 380℃ for 3h; D) Compacted under 250 MPa at 380℃ for 1h with smooth surface

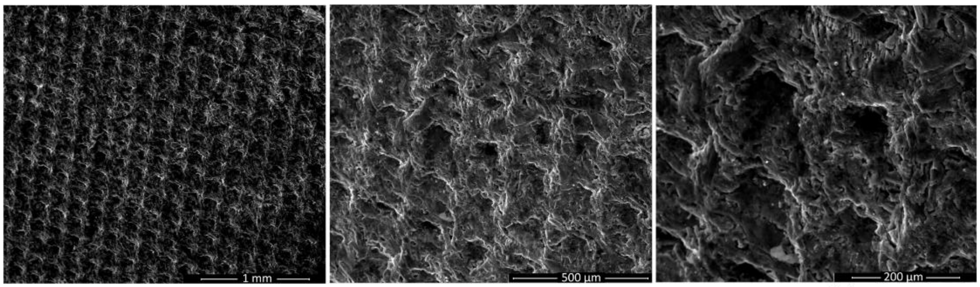

(a) (b) (c)

Figure 25: SEM images of the prepared Mg alloy disc (Compacted under 200 MPa at 400℃ for 3h) with various magnifications: a) 100x; b) 250x; and c) 500x

In Figure 25, surface microstructures of the green plates are distinctly formed on the surface of plates. Micro-shaped surface consists of a porous structure. Production process was completed successfully to manufacture micro-textured porous surfaces.

Pores with a radius of ~60 µm and less were observed on the surface (Fig. 26). Thus, a surface with micro pores was achieved by PM. Pore size and pore morphology have a significant effect on cell attachment and proliferation (Lake et al., 2015). It was proved that the pores with hexagonal morphology increase cell attachment more than pores with spherical shape (Lake et al., 2015). Also, in-vivo studies exhibit that the risk of infection is decreased by increasing pore size after implantation (0.1 mm) (Lake et al., 2015). It was proved that cell attachment was improved by increasing the pore size up to 400 µm (Du et al., 2011). On the other hand, increasing pore size negatively affected the mechanical properties of implants. Implants show brittle behavior by increasing the pore size from 100-200 to 350-450 µm. Thus, increasing pore size declines elastic modulus, shear and compaction strength (Wang et al., 2013). In addition to pore size, pore size distribution plays an important role on cell behavior (Murphy et al., 2010). Wide range of pore size distribution on surface improves cell attachment and proliferation. Therefore, pore size and shape are important parameters in manufacturing of implants. The interconnectivity of pores was proved by using a simple test. A droplet of DMEM was dropped on the surface of green plate and it diffused after few minutes to the other side of the samples.

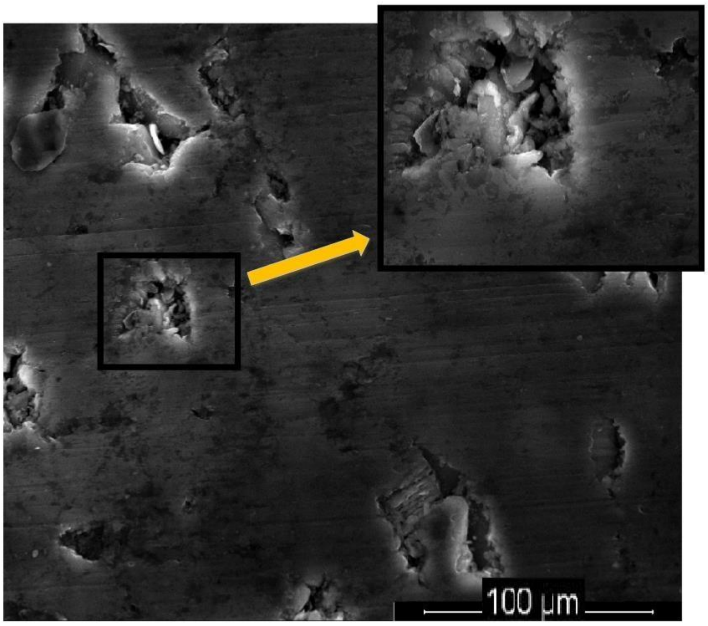

Figure 26: SEM image of Mg alloy plate with porous structure (sample #1)

3.1.4 Surface Area Analysis

As-received powders revealed the highest specific surface area (3.55 m^2/g) while increasing the compaction pressure and sintering time declined the specific surface area (Fig. 27). Moreover, the results proved that plates with textured surface show higher surface area than the plates with smooth surface structure. It is known that porosity and pore size play important role in specific surface area of materials (Diao et al., 2015). Specific surface area of plates was collapsed by increasing the sintering time due to decreasing pore size and grain coarsening (Exner and Arzt, 1990; Davim et al., 2015). Pore size was decreased during sintering process because the neck between compacted particles was grown by supplying activation energy which is necessary for diffusion (Exner and Arzt, 1990). Furthermore, grain growth occurred due to increasing atomic motion (Exner and Arzt, 1990). The results are in good agreement with previous studies which were demonstrated that specific surface area of materials decreased by increasing sintering time and temperature.

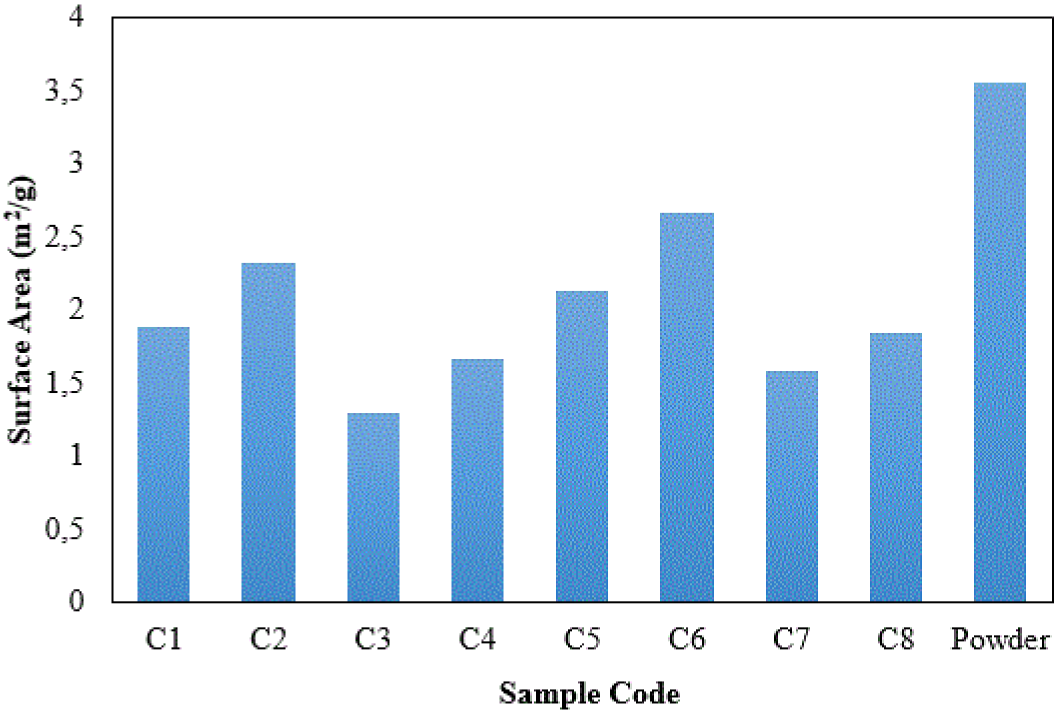

Figure 27: Specific surface area of as-received powders and compacted plates

3.1.5 Confocal Microscope Analysis

Confocal microscope was used to investigate the formation of micro-textures under different compaction pressure and also the surface roughness was measured. Micro-textures are successfully formed on the surface of implants. According to Figure 28, the micro-textures were formed at different ratios with respect to compaction pressure.

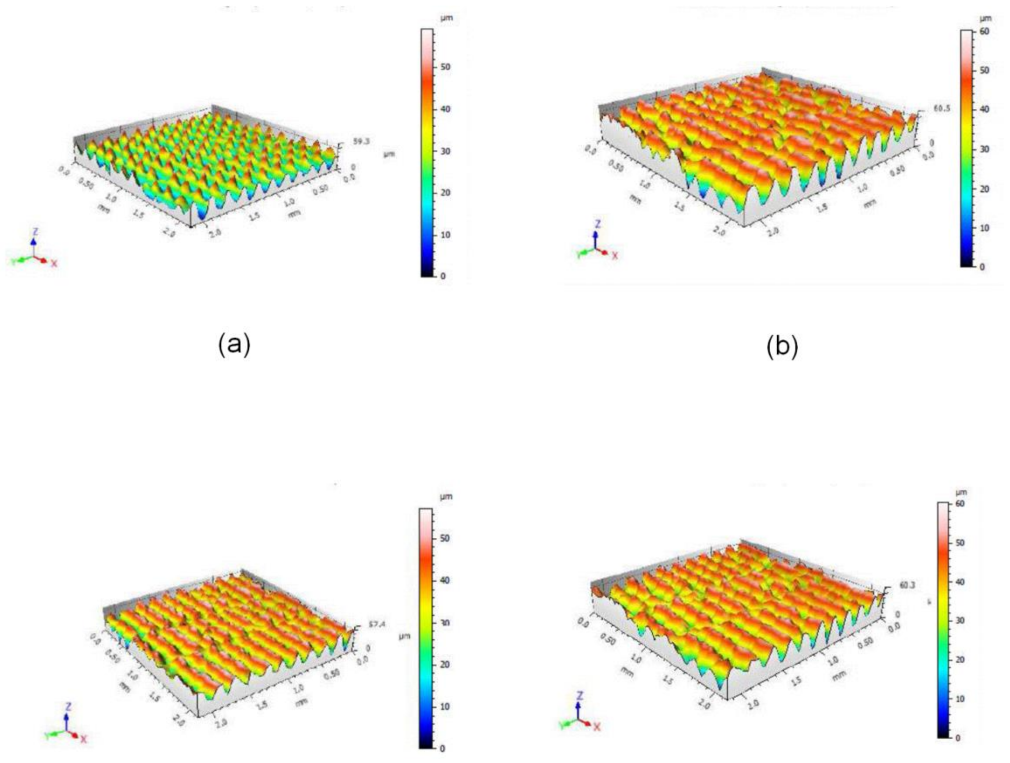

(a)

(b)

(c)

(d)

Figure 28: Confocal images of (a) mold, (b) sample compacted at 150 MPa, (c) sample compacted at 200 MPa, (d) sample compacted at 250 MPa

Surface roughness parameters of the sample and from confocal microscope results in Figure 28 are represented in Figure 29. Mean roughness (Ra) is widely used to evaluate surface roughness in surface engineering (Apedo et al., 2015). According to Figure 28, the mean roughness of the plates was measured between 5.66 and 6.46 µm. there was no significant difference between Ra values of the plates. Thus, it can be concluded that 50 MPa increase in compaction pressure is not a significant parameter to change Ra values of the surface. The summation of maximum height and depth (Rt) and also maximum surface roughness (Rp) of plates show increasing tendency by increasing the compaction pressure. Moreover, the maximum depth (Rv) was decreased by increasing compaction pressure. Contrary to the expectation, Ra, Rv and Rt values of the plates are greater than mold values because high porosity of surfaces results in extensive number of calculation for measuring surface roughness which increases the probability of error. However, the Rp value of mold is bigger than that of plates as expected.

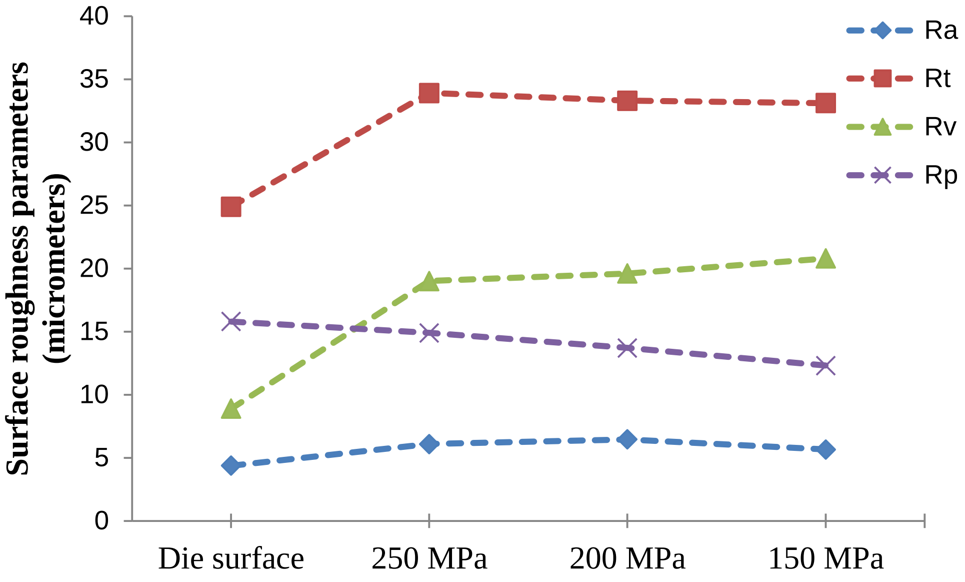

Figure 29: Surface roughness of mold and compacted samples

Combination of surface roughness and porosity accelerates the cell attachment (Happe et al., 2015). Additionally, surface roughness has a positive effect on bone-implant integrity (Lin et al., 2013). Thus, manufacturing a porous surface is an important factor. In addition, surface roughness plays an important role to improve bone-implant bonding under shear stress. van Tol et al. showed that shear strength of bone-implant was increased by increasing surface roughness from 0.058 to 4.25 µm (van Tol et al., 2013). In another study, bonding strength was increased (0.38-9.70 MPa) by increasing Ra (0.2-4µm) values (Scheerlinck and Casteleyn, 2006). The Ra values of Mg plates were measured between 5.66 and 6.44 µm. Previous studies proved that the optimum surface roughness improves bone-implant bonding strength. Rønold et al. investigated the effect of surface roughness on bone-implant integrity for Ti based implants (Rønold et al., 2003). They showed that the best bone-implant integrity was achieved at Ra=3.90 µm and an important decline in bone-implant integrity was observed when Ra value was increased from 5.07 to 11.03 µm (Rønold et al., 2003). In another study, there is a significant increase in bone cell activity by increasing surface roughness from 0.37 to 3.29 µm (Gittens et al., 2011). As explained before, rough surface increases the bone-implant integrity in comparison to smooth surfaces. Thus, an optimum surface roughness should be obtained to achieve maximum bone-implant integrity. It can be concluded that the surface roughness of plates were manufactured in this study at acceptable level for the bone-implant integration.

3.1.6 Density Analysis

Relative densities of Mg alloy discs are presented in Table 10. Standard deviations are also given at the end of relative density values.

Table 10: Relative density of AZ91D-Mg plates (n=3)

		Independent parameters			***Response***
Order	**Random order**	**Compaction pressure (MPa)**	**Sintering time (h)**	**Sintering temperature (^{0} C)**	**Relative density (%)**
1	9	150	1	400	74.49 ±5.23
2	3	150	5	400	69.65 ±1.48
3	12	250	1	400	75.2 ±1.08
4	8	250	5	400	72.84 ±1.19
5	1	150	3	380	70.94 ±4.22
6	14	150	3	420	74.55 ±2.66
7	10	250	3	380	81.52 ±4.35
8	7	250	3	420	77.17 ±2.27
9	6	200	1	380	77.4 ±2.89
10	15	200	1	420	75.98 ±2.38
11	5	200	5	380	76.58 ±1.18
12	2	200	5	420	77.71 ±3.56
13	4	200	3	400	79.66 ±2.12
14	13	200	3	400	75.74 ±1.92
15	11	200	3	400	76.55 ±2.01

Relative densities of Mg alloy discs prepared by PM varied from 71 to 82% under compaction pressures of 150, 200 and 250 MPa. Results were compatible with results of similar studies in the literature. Al-2.5Mg alloy powder particle densified between 70-80% under 200 MPa. Additionally, 50 MPa increase in pressure led to an increase up to 83% of relative density (Moazami-Goudarzi and Akhlaghi, 2013). In the compaction range of 100-290 MPa, the same compaction pressure caused more densification in Fe metal powders with spongy-like morphology due to higher specific surface area than the particles having spongy morphology. Spherical shaped particles had relative density of 48.9-65.7% while spongy shaped particles had 55 and 71.4% (Poquillon et al., 2002). Beyond that, Mg alloy particles with needle-like shape and wide variety of particle size were compacted. The morphological and dimensional characteristic of Mg alloy powder induced higher densification rates in this study. It was proved that Ti alloy powder with irregular shapes (spongy, needle-like and flaky) had higher densification capability than spherical or cuboidal powders (Chikosha et al., 2014). It can be concluded that Mg alloy discs densified better than the counterparts manufactured at the same conditions since they had irregular morphology and wide range of particle size. Irregular morphology having high specific surface area provides more contact area to create a bond between particles and could be the reason behind better densification.

Corresponding to Table 11, compaction pressure had a significant effect on relative densities of Mg alloy discs. In another aspect, sintering parameters did not affect significantly the densification behavior. Sintering parameters generally change the relative density of compacted powders. However, the effect of sintering parameters was limited on the relative densities. Relative density depends on sintering temperature and time owing to dimensional changes during heat treatment. Sintering parameters contribute further densification on spherical powders as just as compaction pressure. However, the same effect was not seen in this study (Fig. 30). Similarly, the sintering effect was minor on the relative density of Ti alloy powder with irregular morphology (Xiao et al., 2011; Bolzoni et al., 2013).

Table 11: Analysis of variance for relative density

Variation source	**Degree of freedom**	**Sum of Squares**	**Mean Squares**	**F**	**P**
Compaction Pressure	2	0.006101	0.00305	5.23	0.035
Sintering Time	2	0.001561	0.00078	1.34	0.315
Sintering Temperature	2	0.000636	0.000318	0.55	0.600
Error	8	0.004664	0.000583		
Lack of fit	6	0.003806	0.000634	1.48	0.456
Pure Error	2	0.000858	0.000429		
Total	14	0.01307			

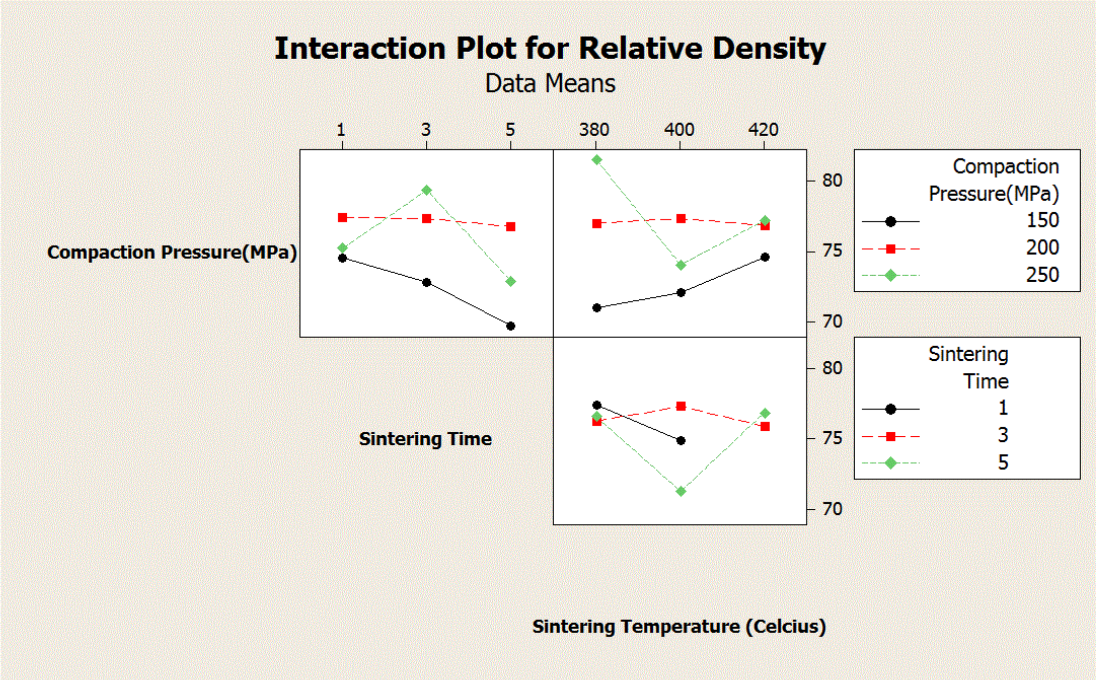

Figure 30: Interaction effect of manufacturing parameters on relative density

Figure 31 shows effect of sintering temperature and compaction pressure on relative density at the same time. Results clearly proved that the highest relative density is achieved for samples compacted at 250 MPa and sintered at 380°C. On the other hand, relative density was declined by increasing sintering temperature. Furthermore, the smallest relative density was obtained for samples compacted at 150 MPa and sintered at 380°C. Thus, compaction pressure is the most effective parameter on relative density in recent study. Irregular shape of particles may play an important role in this phenomena because the number of contacted point increases during compaction pressure due to the irregular shapes of AZ91D-Mg powders used in this study.

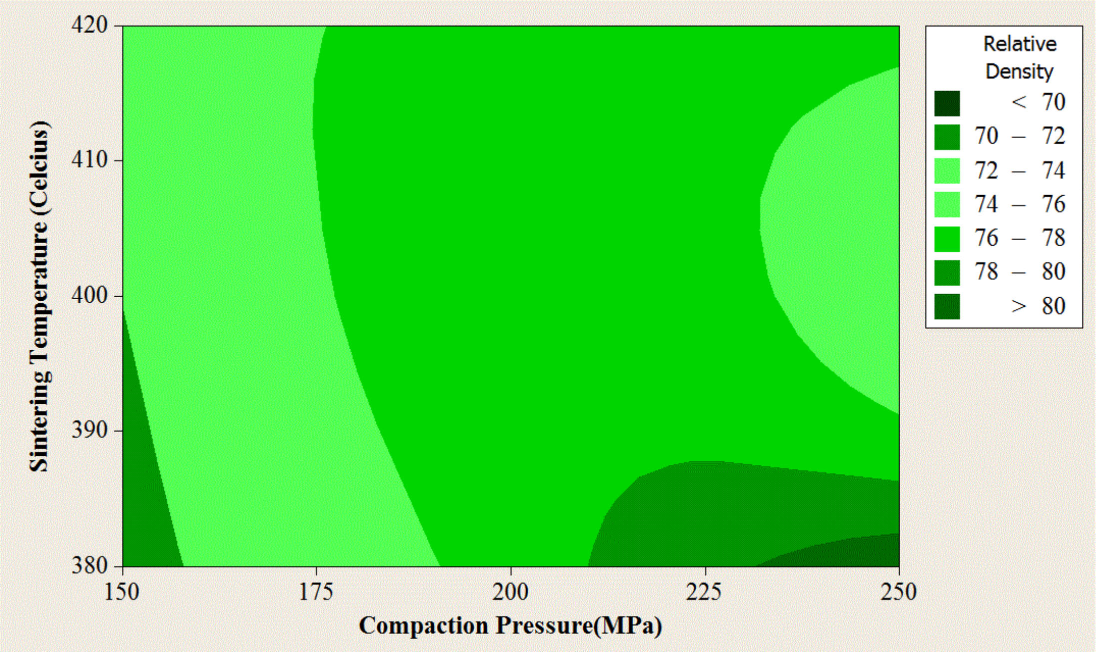

Figure 31: Effect of sintering temperature and compaction pressure on relative density

3.2 Mechanical Test

3.2.1 3-point Bending Analysis

In Table 12, 3-point bending test results are presented. Maximum bending strength values of Mg alloy discs varied from 30 to 60 MPa. It is expected that porous materials have less mechanical integrity than their bulk counterparts (Fan et al., 2013). Micro or nano pores in microstructure or on surface, which can be regarded as discontinuities or flaws, cause unexpected fractures and also reduce the mechanical strength acting as stress concentrators. However, the discs prepared by pure Mg alloy powders had lower bending strength than the bending strength obtained in this study (Zhuang et al., 2008; Čapek and Vojtěch, 2014). In a similar study, compacted Fe powders under pressures of 100-290 MPa resulted in bending strength between 8.2 and 61.2 MPa (Poquillon et al., 2002). Furthermore, compacted MgO/Fe-Ni-Cr composite powders having porosity of 50.9-51.6% had bending strength in the range of 21-65.8 MPa (Chen et al., 2011). Apart from this, higher bending strength can be interpreted in terms of powder particle morphology. In this study, irregular and needle-like Mg alloy powder contributed high bending strength due to the fact that powder morphology has great impact on mechanical properties.

It is important that an implant material should show mechanical resemblance to bone. Bending strength measurements varied from 25 to 300 MPa in the bone extracted from various animals (Currey, 1999). It can be concluded that even if the bending strength values do not span all animal bone bending strength value range (25-300 MPa), the values cover most of the bending strength belonging to numerous animal bones.

Table 12: 3-point bending results of AZ91D-Mg plates (n=3)

		Independent parameters			***Response***
Order	**Random order**	**Compaction pressure (MPa)**	**Sintering time (h)**	**Sintering temperature (℃)**	**Bending strength (MPa)**
1	9	150	1	400	34.25 ±2.73
2	3	150	5	400	30.26 ±2.30
3	12	250	1	400	53.62 ±1.81
4	8	250	5	400	43.69 ±3.12
5	1	150	3	380	30.93 ±1.72
6	14	150	3	420	35.12 ±3.02
7	10	250	3	380	59.76 ±3.88
8	7	250	3	420	41.99 ±1.67
9	6	200	1	380	41.90 ±3.41
10	15	200	1	420	36.21 ±2.16
11	5	200	5	380	38.43 ±2.57
12	2	200	5	420	44.42 ±1.53
13	4	200	3	400	41.57 ±1.02
14	13	200	3	400	40.99 ±1.37
15	11	200	3	400	43.44 ±3.16

According to Table 13, Compaction pressure has significant effect on maximum bending strength while sintering time and temperature have not significant effect. Sintering parameters affected precipitation and morphology of second phase in the structure in which presence of secondary intermetallic phase decrease strength of AZ91D-Mg alloy (Yan et al., 2014). However, the precipitation of β-$Mg_{12}Al_{17}$ intermetallic phase in nano-scale along grain boundary improve mechanical strength (Yan et al., 2014).

Table 13: Analysis of variance for bending strength

Variation source	**Degree of freedom**	**Sum of Squares**	**Mean Squares**	**F**	**P**
Compaction Pressure	2	0.006101	0.00305	10.08	0.005
Sintering Time	2	0.001561	0.00078	0.73	0.510
Sintering Temperature	2	0.000636	0.000318	0.19	0.831
Error	8	0.004664	0.000583		
Lack of fit	6	0.003806	0.000634	1.62	0.456
Pure Error	2	0.000858	0.000429		
Total	14	0.01307			

Effect of manufacturing parameters on the bending strength of each Mg alloy disc was investigated through main effect diagram (Fig. 32). When a material is subjected to bending, bending fracture is expected where discontinuity or flaws are placed. Besides, fracture can be originated from grain boundaries due to poor bonding between particles or regions where intermetallic phases form (Wang et al., 2008). Discontinuities such as pores decrease bending strength as well as other mechanical properties (Čapek and Vojtěch, 2014). Moreover, the precipitation and morphology of β phase in AZ91D-Mg alloy have significant effect on mechanical strength (Yan et al., 2014). Percentage of second phase was increased by heat treatment of AZ91D-Mg and the β phase mostly precipitated around Al rich regions (Yan et al., 2014). It was proved that hot compression improves the mechanical properties of AZ91D-Mg because of crushing of β phase to smaller blocks which was participated along grain boundaries before hot compression (Yan et al., 2014).

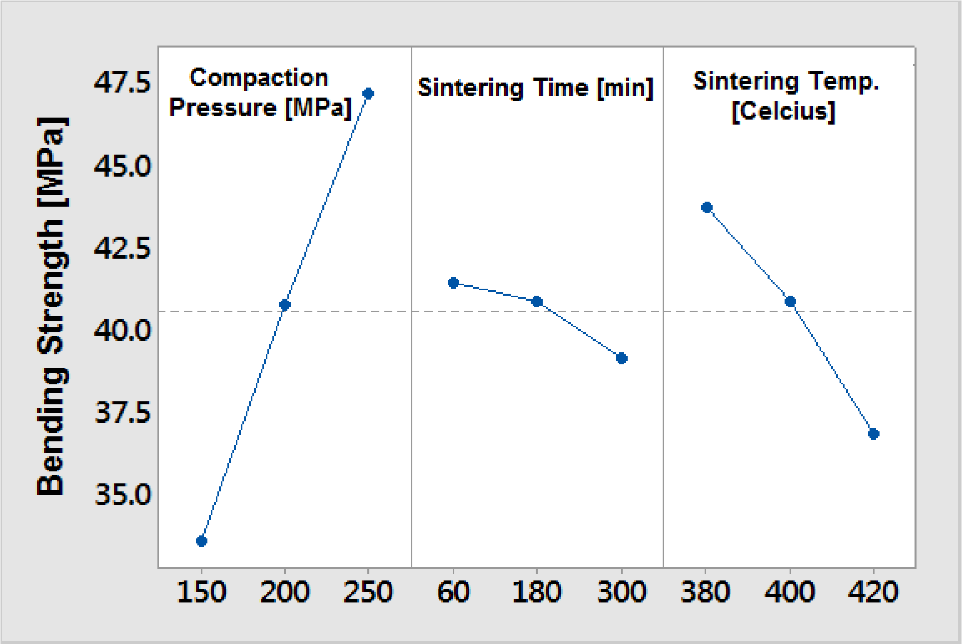

Figure 32: Effect of manufacturing parameters on bending strength

The bending strength sharply increased as compaction pressure increased. It was already known that higher pressures allow further densification in metal powders (Zhuang et al., 2008). However, it was also concluded that mechanical interlocking between needle-like Mg alloy particles was increased as compaction pressure increased. Although the positive effect of compaction pressure on bending strength was shown by several studies (Jabur, 2013; Luo et al., 2014). It can be said that the mechanical interlocking contributed further increase in the bending strength.

Bending strength of the sample was decreased as sintering temperature and time increased. In compaction stage, powder particles are bonded to each other by applying the compressive stress. In this study, the drop in bending strength with increasing the sintering time and temperature could be originated from relieving tensile stress in Mg alloy discs. Sintering effect was compatible with literature studies. Many metal powders showed the same behavior with increasing temperature and time (Zhou et al., 2013; Wang et al., 2014). Longer sintering time and higher sintering temperature induce grain growth in the microstructure that reduces dislocation resistance by diminishing interparticle surface area. For this reason, bending strength was reduced by increasing sintering time and temperature in this study.

Highest and lowest bending strength values are also represented in a response surface of two parameters (Fig. 33). The highest bending strength was measured for Mg alloy disc, which was sintered for 1 h after compaction under 250 MPa. The lowest value was obtained as the sintering time was 5 h and compaction pressure was 150 MPa.

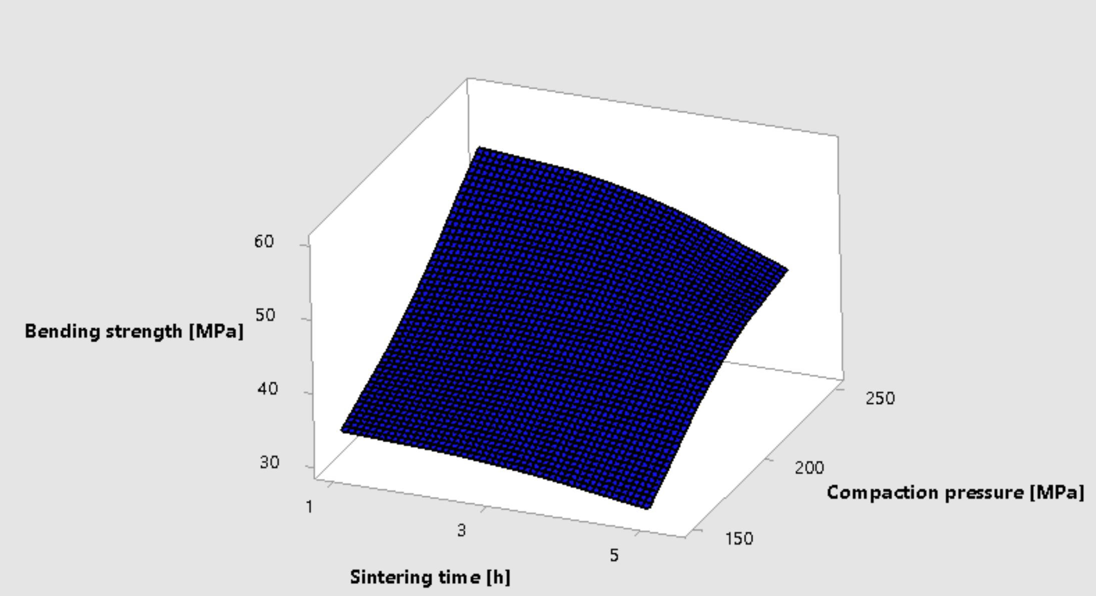

Figure 33: Response surface plot showing the relationship bending strength sintering time and compaction pressure

3.3 Corrosion Analysis

3.3.1 Electrochemical Analysis

3.3.1.1 Hank’s Solution

Potentiodynamic polarization curve for Hank’s solution are given in Figure 34. Corrosion potential of plates was between -1.532 and -1.440 V which shows high similarity to previous studies. Zhang et al. showed that corrosion potential of Mg-Y alloys located between -1.605 and -1.580 V (Zhang et al., 2013). Additionally, the corrosion potential of AM50-Mg alloys with different Gd amount is increased from -1.75 to -1.51 (Miao et al., 2014). Thus, the corrosion resistance of Mg-Y and AM50-Mg alloys is lower than plates produced by PM method in this study. In another study, the corrosion potential of AZ91 was measured as -1.45 V (Rojaee et al., 2014). Also, Wu et al. showed corrosion potential of AZ92-Mg alloy with different amount of Sm element is between -1.526 and -1.464 V for which corrosion resistance was improved by addition of Sm (Daogao et al., 2014).

The corrosion resistance is increased with increasing corrosion potential (Nam et al., 2012). According to Potentiodynamic curves some abrupt changes and irregularities can be seen in graphics. This phenomena shows crevice corrosion which is one of the common corrosion types in Mg and its alloys in aggressive electrolytes (Garcia et al., 2009). Presence of open pores on the surface of the plates may accelerate crevice corrosion mechanism in this study which caused abrupt changes in Potentiodynamic curves.

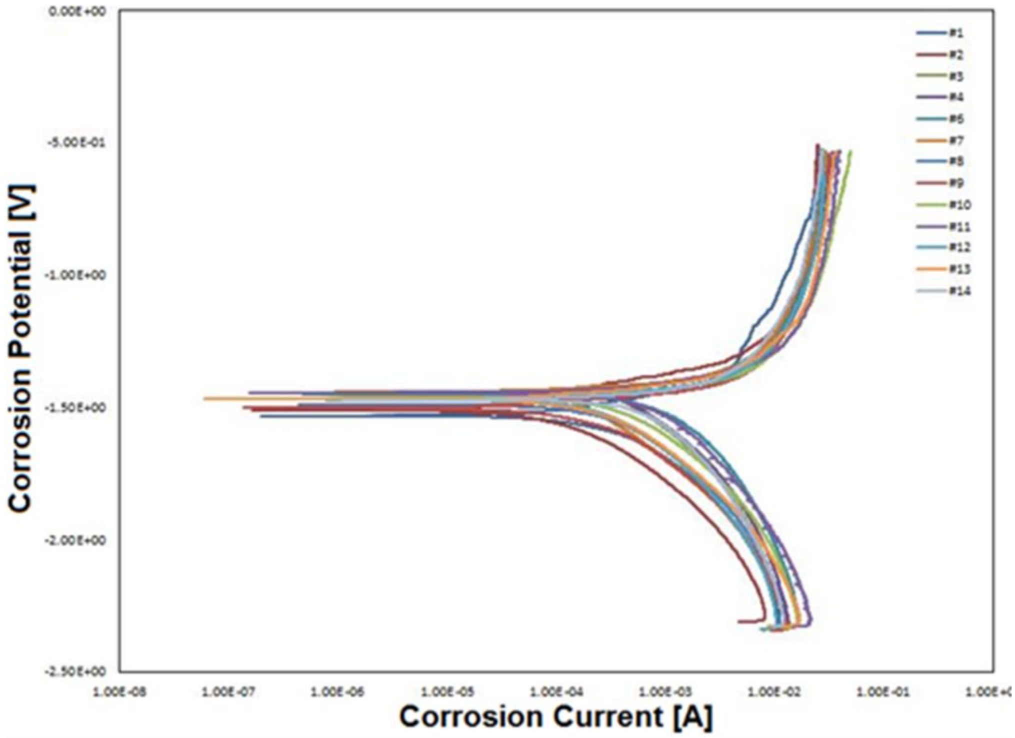

Figure 34: Potentiodynamic curves of surface modified AZ91D-Mg plates in Hank’s solution

The surface morphology of plates was investigated by SEM after electrochemical tests. Figure 35 shows surface morphology of sample number 1 after electrochemical test in Hank’s solution. It is observed that some parts of plate are more susceptible to corrosion which is an expected phenomena due to porous structure and textured surface of plates in this study. Bright portions indicate notches on the surface while the darker parts are showing high architectures.

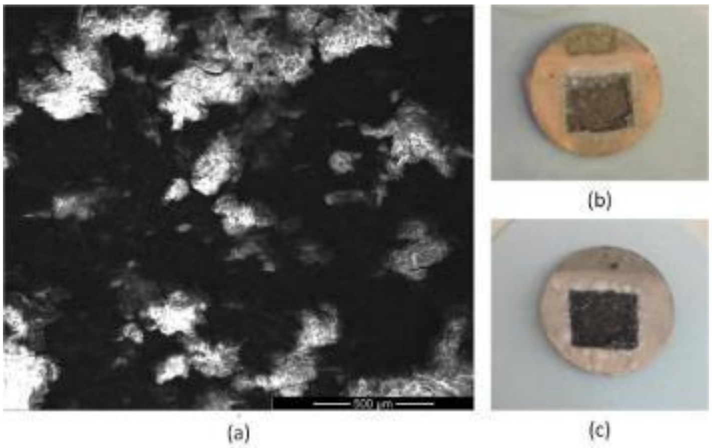

Figure 35: Surface morphology of sample #1 after electrochemical test in Hank’s solution

The main effect diagram in Figure 36 shows impact of manufacturing parameters on corrosion resistance of AZ91D-Mg alloy in Hank’s solution. It can be seen that corrosion potential was increased by increasing compaction pressure. Thus, an increase in compaction pressure improves corrosion resistance of all samples. Garcia et al. proved corrosion resistance of stainless steel samples manufactured by PM route with compaction pressures from 400 to 800 MPa (García et al., 2007). Also, the corrosion rate was decreased with increasing sintering time from 60 to 180 min. However, the corrosion resistance was decreased after increasing the sintering time to 300 min. On the other hand, the highest corrosion resistance was achieved at 380°C while the corrosion rate is decreased by increasing sintering temperature from 400 to 420°C.

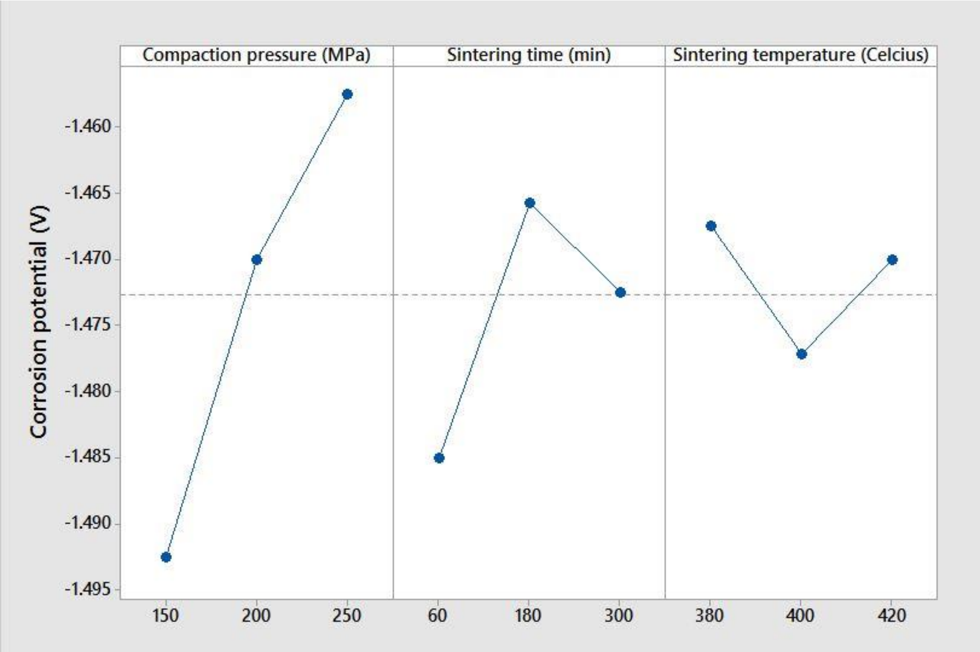

Figure 36: Effect of manufacturing parameters on corrosion potential in Hank's solution

Figure 37 shows effect of sintering temperature and compaction pressure on corrosion resistance at the same time. In this figure, light colored portion shows high corrosion voltage values while darker portions show low corrosion voltage values. According to this figure, the lowest corrosion resistance was seen for the sample compacted with 150 MPa at 400°C.

It is clearly seen that sintering temperature and time affected the corrosion resistance of plates. This phenomena can be explained by considering the effect of sintering temperature and time on precipitation of second phase (β-$Mg_{17}Al_{12}$) and grain refinement. Presence of second phases in structure of Mg alloys leads to micro galvanic corrosion (Zhang et al., 2013). The precipitation of intermetallic phase along grain boundary increased the corrosion rate of Mg alloys (Zhang et al., 2013). Furthermore, precipitation regions and distribution of second phase are effective parameters on corrosion behavior of Mg alloys such as AZ91, Mg-Sr and Mg-Zn series in which discontinuous morphology of second phase accelerate micro-galvanic corrosion (Zeng et al., 2006; Zhang et al., 2013). Also, amount of second phase affected the corrosion rate because micro galvanic corrosion rate anticipated with

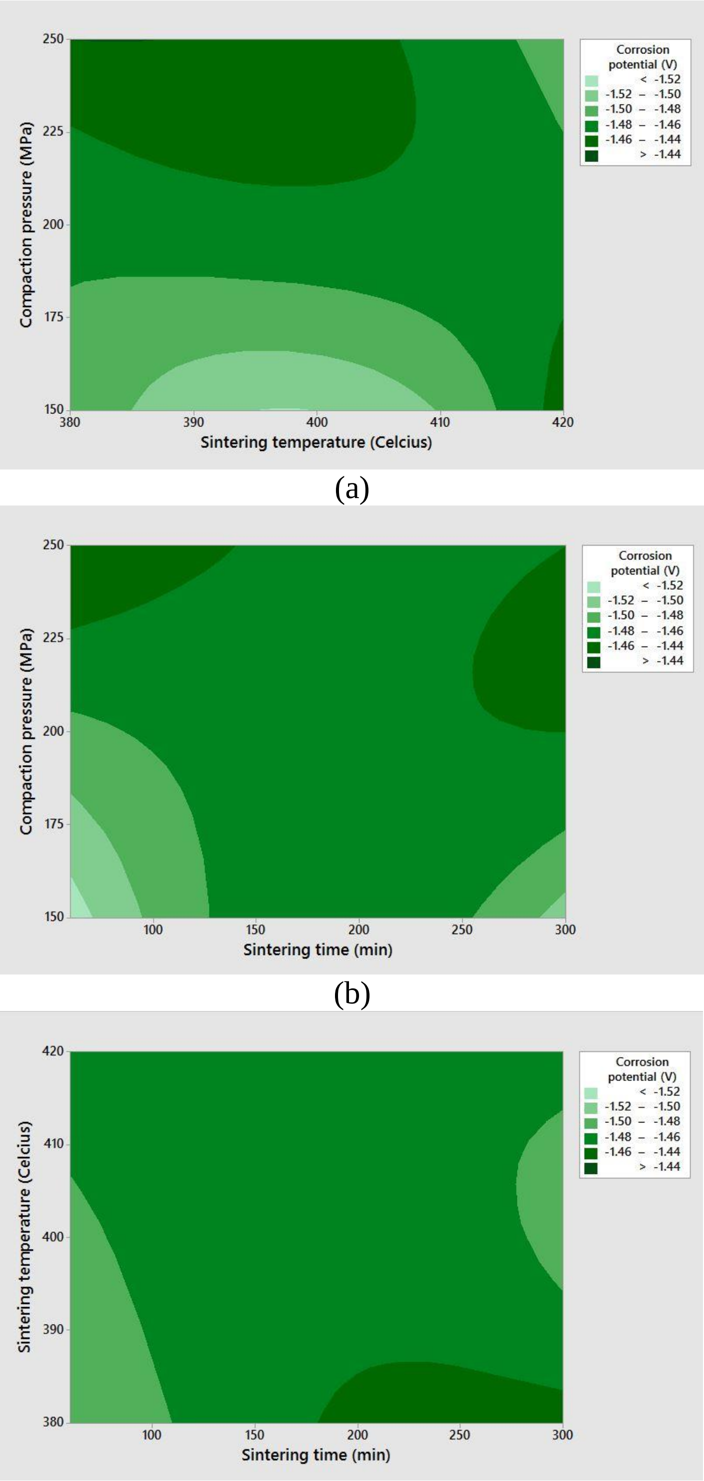

(a)

(b)

(c)

Figure 37: Effect of (a) sintering temperature and compaction pressure, (b) sintering time and compaction pressure, (c) sintering temperature and time on corrosion potential

cathode/anode area (Zhang et al., 2013). While, the precipitation of second phase such as β-$Mg_{17}Al_{12}$ acted as a corrosion barrier when continuously formed along grain boundary edge (Zhang et al., 2013). Thus, the amount and morphology of second phase affected the corrosion rate of Mg alloys.

On the other hand, the lowest corrosion resistance was seen in samples compacted with 150 MPa for 60 and 300 min by conjunction effect of compaction pressure and sintering time. Guo et al. investigated the effect of sintering parameters on Ti samples produced with PM technique (Guo et al., 2014). Samples were sintered between 1150 and 1350°C for 1, 2, 3 and 4h. The highest corrosion resistance was achieved for samples compacted at 1250°C for 2h. In another study, the corrosion rate of Al_2O_3 coated AZ91-Mg alloy was decreased by increasing the sintering temperature from 180 to 380°C which is similar to a recent study (Zhong et al., 2009). Thus, it can be concluded that an optimum sintering temperature should be selected to improve corrosion resistance.

3.3.1.2 DMEM (L) and DMEM+10%FBS

The maximum corrosion resistance in DMEM was achieved for plates which were compacted at 250 MPa while plates that were compacted under 200 MPa showed the highest corrosion rate at DMEM as an electrolyte (Fig. 38). Plates which are compacted under higher load show better corrosion resistance which is similar to results obtained for plates in Hank’s solution. However, samples compacted at 150 MPa show higher corrosion resistance than plates compacted at 200 MPa. It was seen that protective layer was not formed on the surface of plates compacted under 250 MPa led to show higher corrosion rate.

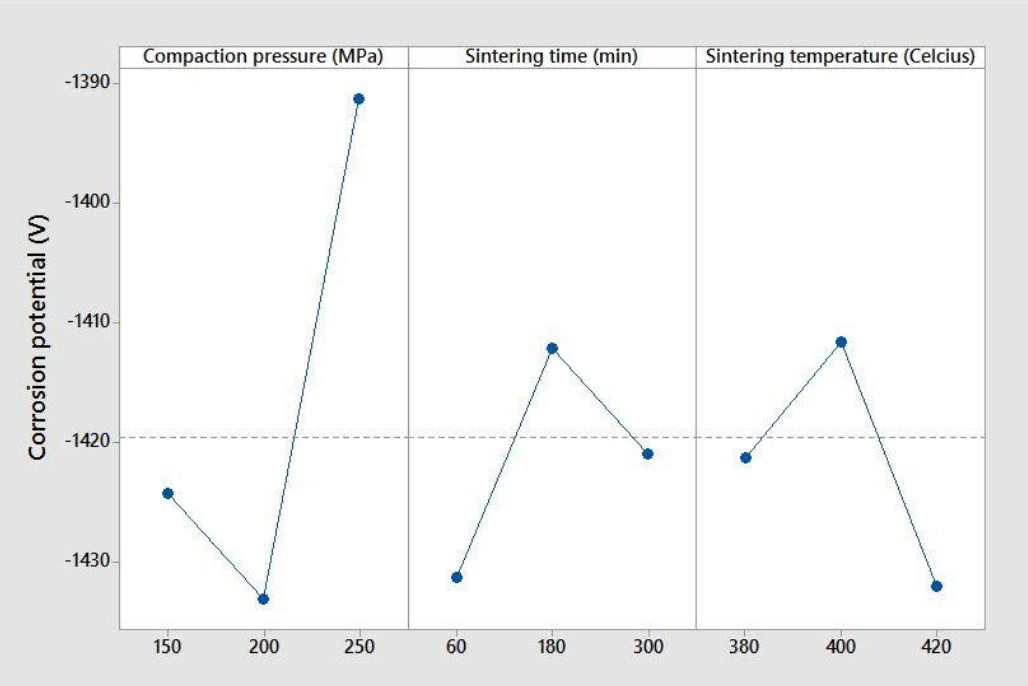

Figure 38: Effect of manufacturing parameters on corrosion potential of AZ91D-Mg in DMEM (L)

A similar trend with Hank's solution was observed when effect of compaction load and sintering time on corrosion resistance was investigated at the same time. The most effective protective layer for Mg plates was achieved for the samples sintered for 3h (Guo et al., 2014). Corrosion resistance of samples sintered for less or more than 3 h can be effected by second phase precipitation and porosity factors which play an important role corrosion behavior of Mg. Corrosion resistance of AZ91D-Mg samples was decreased with increasing sintering temperature from 380 to 400°C. On the other hand, corrosion rate was decreased with increasing sintering temperature up to 420°C. This phenomena happened due to formation of more stable protective layer on the surface during electrochemical tests in DMEM solution for samples which are sintered at 380°C and precipitation of α and β phases for plates which are sintered at higher sintering temperature (420°C) (Wang, 2003; Guo et al., 2014).

Figure 39 shows impact of manufacturing parameters on corrosion potential of AZ91D-Mg samples in DMEM+10%FBS. Corrosion behavior of plates in

DMEM+10%FBS is different than degradation in Hank's and DMEM due to presence of protein in electrolyte. Thus, absorption of protein on the surface of Mg alloys has significant effect on its corrosion resistance. The highest corrosion resistance was achieved for plates which were compacted at 200 MPa. Also, it was proved that corrosion rate was decreased with increasing the sintering temperature and time. Protein binding is thought to increase the corrosion resistance so the most suitable condition for sintering is the highest sintering temperature and time (Hiromoto et al., 2005). On the other hand, Hiromoto et al. proved corrosion resistance of Mg alloys in the presence of FBS was increased by decreasing the grain size of Mg alloys (Hiromoto et al., 2005). It can be concluded that the smallest corrosion rate is achieved for the samples sintered at 420°C for 5h. Yun measured corrosion potential of pure Mg in McCoy 5A solution (5% FBS) which was -1.550 V (Yun et al., 2009). The corrosion rate of samples in this study is lower than previous works which are explained above.

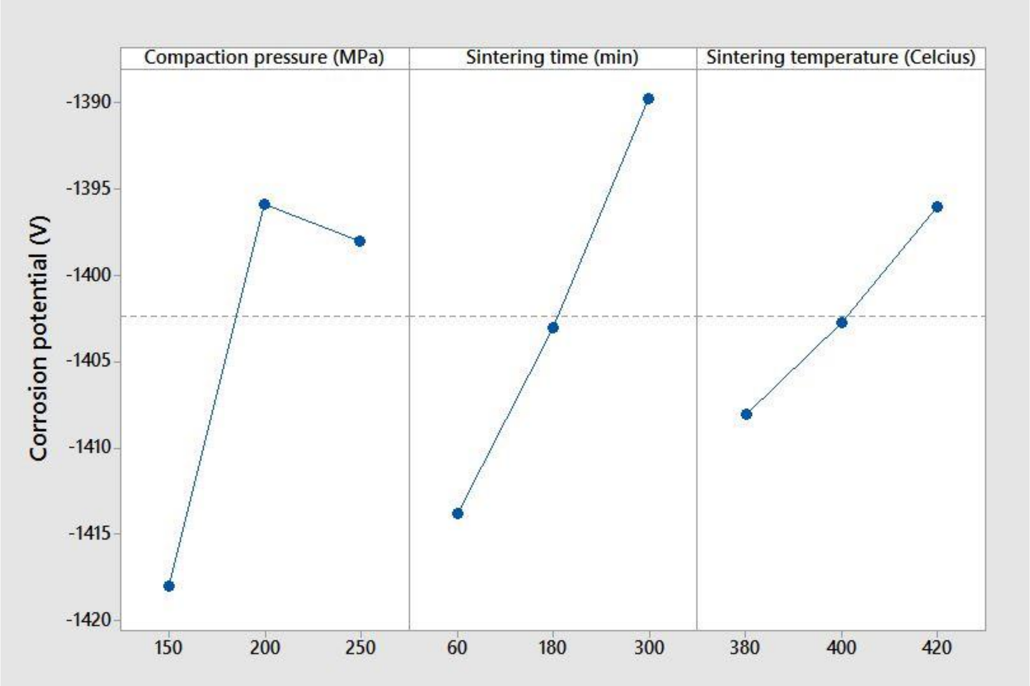

Figure 39: Effect of manufacturing parameters on corrosion potential in DMEM (L) +10% FBS

Morphology of samples 1, 2 and 3 was investigated with SEM and EDX after electrochemical test in DMEM and DMEM+10%FBS (Fig. 40 and 41). Presence of Ca and P ions on the surface of samples after electrochemical tests in DMEM was proved by EDX analysis. Also, other corrosion products such as C, O, Mg, Al, Na and Cl were seen on the surface of samples. The Ca/P ratios for the samples 1, 2 and 3 were measured as 3.93, 4.03 and 1.42, respectively. Also, the electrochemical test results showed that the highest corrosion rate was achieved for the samples with highest Ca/P ratio while the highest corrosion resistance was measured for the samples with smallest Ca/P ratio. The smallest amount of Ca ion on the surface of corroded Mg resulted in formation of $(Ca_{0.86}, Mg_{0.14})_{10}(PO_4)_6(OH)_2$ or $Ca_{10}(PO_4)_6(OH)_2$ which act as a protective layer and decreased corrosion rate of Mg and its alloys (Zander and Zumdick, 2015). Also, it is known that Ca/P ratio of HA (1.67) is an important component of bone. Additionally, previous studies proved that presence of HA on the surface of bone implant improves bone-implant integration. High Ca/P ratio led to an increase in corrosion rate of Mg implants (Gu et al., 2011). Thus, it can be concluded Ca/P ratio play an important role in corrosion resistance of Mg and its alloys.

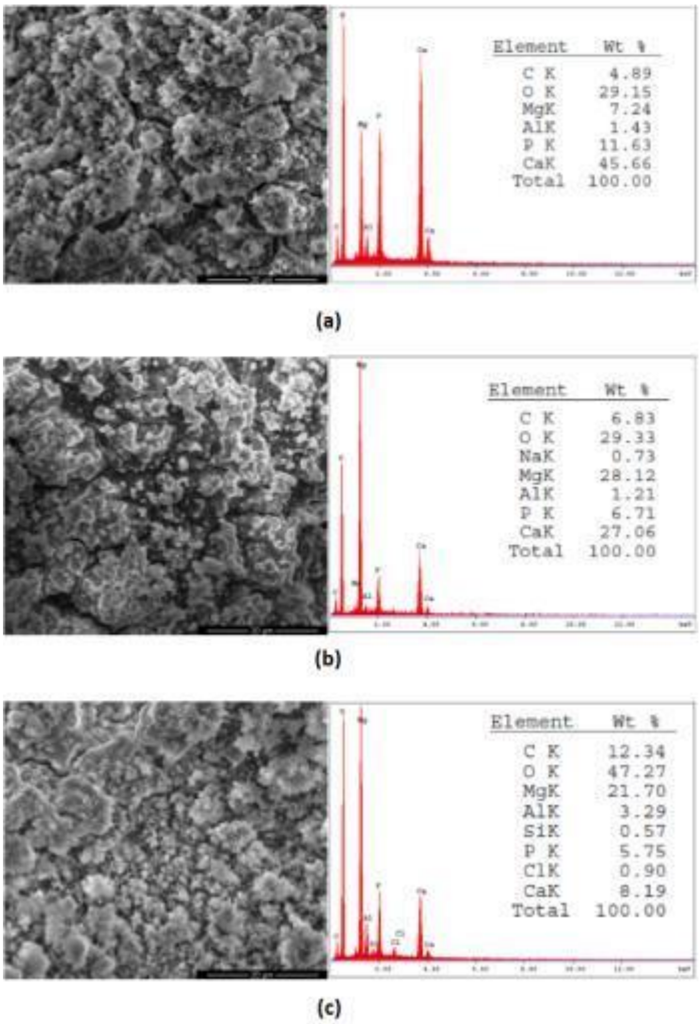

(a)

Element	Wt %
C K	4.89
O K	29.15
MgK	7.24
AlK	1.43
P K	11.63
CaK	45.66
Total	100.00

(b)

Element	Wt %
C K	6.83
O K	29.33
NaK	0.73
MgK	28.12
AlK	1.21
P K	6.71
CaK	27.06
Total	100.00

(c)

Element	Wt %
C K	12.34
O K	47.27
MgK	21.70
AlK	3.29
SiK	0.57
P K	5.75
ClK	0.90
CaK	8.19
Total	100.00

Figure 40: SEM images and EDX analysis of sample (a) #1, (b) #2 and (3) #3 after electrochemical test in DMEM

The Ca/P ratio of the samples 1, 2 and 3 on DMEM+10%FBS were measured 1.26, 1.87 and 1.67, respectively which show higher similarity to Ca/P ratio of hard tissues. Sample #3 shows the highest corrosion resistance among this samples (Ca/P=1.67). Also, it can be seen that samples compacted at 250 MPa showed the highest corrosion resistance in DMEM and DMEM+10% FBS.

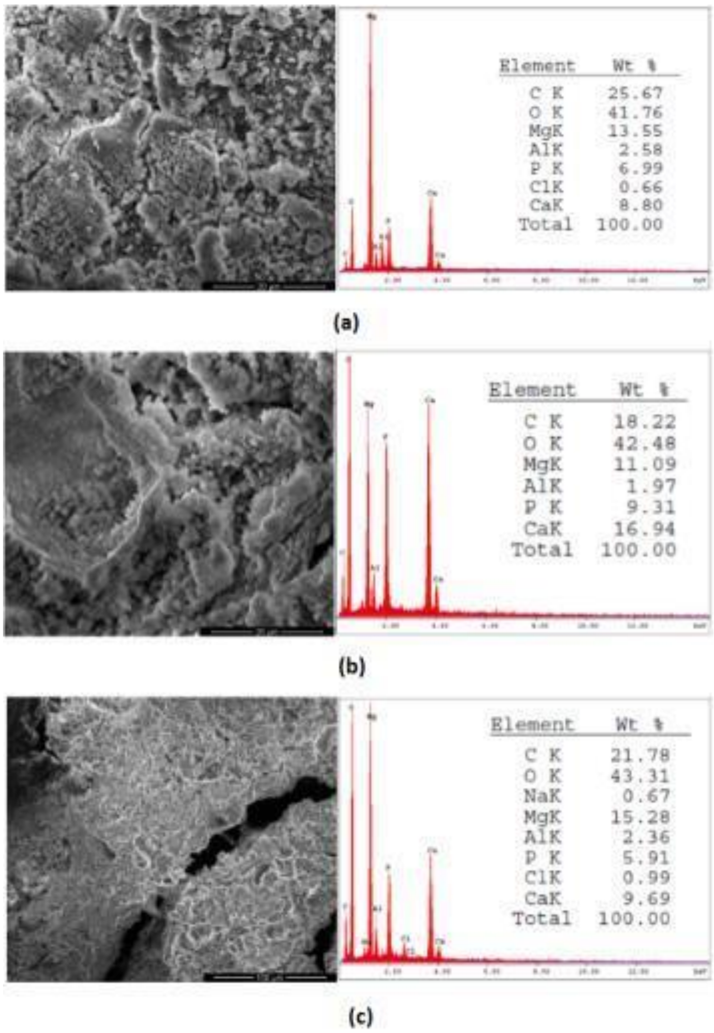

Figure 41: SEM images and EDX analysis of sample (a) #1, (b) #2 and (3) #3 after electrochemical test in DMEM + 10% FBS

Electrochemical test results are tabulated in Table 14. The lowest corrosion potential and current density were obtained in Hank's solution. The existence of higher Cl^- and lower $NaHCO_3$ content in Hank's solution led to a decrease in corrosion potential in Mg alloys (Chun Yan et al., 2010). Furthermore, high corrosion potential and current density were obtained in DMEM and DMEM + 10%FBS. This refers that Mg discs had higher corrosion rate in Hank's solution. Low corrosion potential in Hank's solution could be originated from the direct attack of Cl^- ions to intermetallic phases such as $Mg_{12}Al_{17}$ (Arrabal et al., 2013). Between DMEM and 10%FBS containing DMEM solutions, Mg alloy discs had lower corrosion potential in DMEM solution. Depending on FBS existence, protein adsorption and Al_2O_3 formation act as corrosion protective barrier on the surface of Mg discs (Gu et al., 2009). Presence of amino acids and proteins increases the corrosion resistance of Mg alloys (Sanchez et al., 2015). They help to form a protective layer on the implant surface against aggressive corrosive attacks. A highly porous surface also increased the corrosion resistance by contributing the protein and amino acid adsorption on the surface. However, this behavior can be changed drastically depending on the composition of the alloy in the presence of amino acids and proteins (Gu et al., 2009; Liu et al., 2010). For instance, the corrosion resistance of pure Mg and LAE422 Mg alloy decreases in solutions containing amino acids and proteins while the corrosion resistance of AZ31, AZ91 and Mg-Ca alloys increases in the same solution. In this study, the highest corrosion potential and current density were seen in 10%FBS containing DMEM solution due to the blocking micro galvanic pile originating from intermetallic phases. Apart from this, porous surface led to a decrease in corrosion rate because it accelerated the protein adsorption further. The higher corrosion potential values in DMEM than Hank’s solution can be interpreted based on higher protein adsorption due to porous surface of Mg alloy discs. The higher corrosion rate of in vitro than in vivo studies was also related to the degree of protein adsorption in another study (Sanchez et al., 2015).

Table 14: Corrosion potential values of Mg alloy discs in three different solutions

Solution	E_{corr} (V)	J_{corr} (mA/cm^2)	E_{pitt} (V)	$\lvert E_{corr} - E_{pitt}\rvert$
Hank	-1.47±0.02	1.242±0.08	-1.22±0.08	0.25
DMEM	-1.42±0.04	0.382±0.03	-1.14±0.03	0.28
DMEM+10%FBS	-1.40±0.04	0.242±0.07	-1.07±0.05	0.33

Pitting corrosion was observed after forming crevices on the exposed surfaces by localized corrosion attacks. Pitting corrosion potentials were also defined based on electrochemical potential curves (Fig. 42). Pitting corrosion potentials were obtained from where corrosion potential sharply changes in the electrochemical curve. As seen from SEM image in Figure 42, the crevices originating from pitting corrosion occurred. It is expected that porous surfaces as in this study are more prone to the formation of crevices due to pitting corrosion. The difference between corrosion potential and pitting potential shows resistance degree of materials to pitting corrosion (Tao et al., 2010). Mg alloy discs showed the higher difference in DMEM+10%FBS solution that stands for their higher pitting resistance than other solutions. Lowest potential difference was obtained in Hank's solution.

Electrochemical curves of the Mg alloy discs with porous and smooth surfaces are obtained in three different solutions (Fig. 42). Mg alloy disc with a smooth surface had lower corrosion potential than the one with porous surface in DMEM+10%FBS. Although porous surfaces are more inclined to corrode, the absorbed protein and amino acids restricted intense corrosion of the porous surface. It was also stated that rough surfaces inhibit pitting corrosion which can cause a reduction in corrosion potential (Alvarez et al., 2010). However, the presence of organic substances protected the porous surface more than the smooth one.

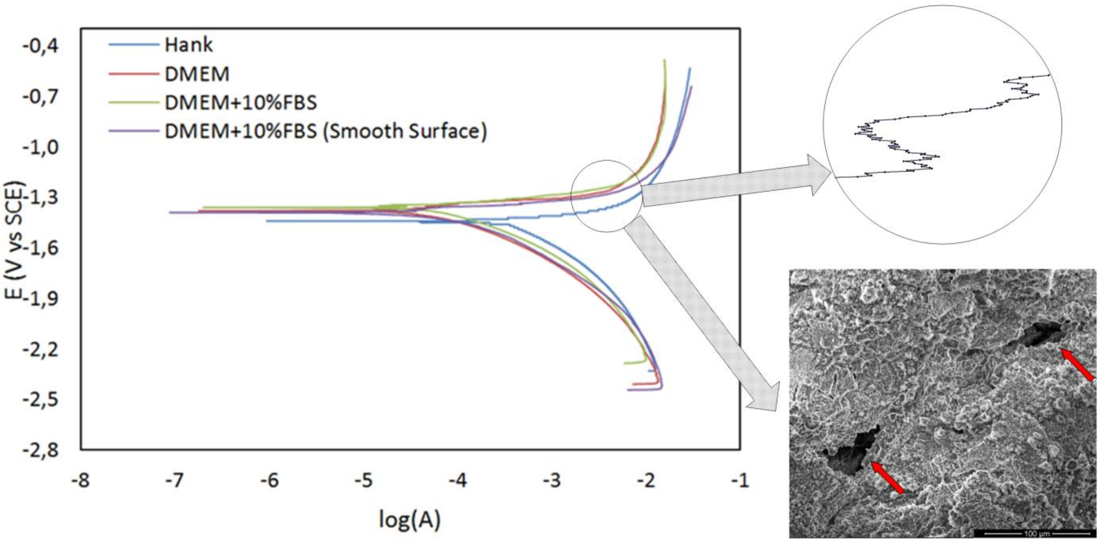

Figure 42: Electrochemical potential curves of Mg alloy discs

3.3.2 Immersion Analysis

Immersion test was conducted in SBF to determine dynamic corrosion rate of AZ91D-Mg plates. Figure 43 shows relationship between weight loose and immersion time in SBF. The corrosion rate of all samples increased at the end of 4th day, in comparison to their corrosion rate at the end of 2nd day. However, the corrosion rate of all samples declined steadily after 4th day. Previous studies proved weight loose rate increase with increasing immersion time because of the formation of cracks crevasses on the surface of plate which accelerate pitting corrosion mechanism (Zhang et al., 2011; Walton et al., 2012). However, the other factor which has an important role in corrosion rate is formation of calcium phosphates on the surface of Mg and its alloys in SBF. Calcium phosphates act as a protective layer and decrease corrosion rate (Zhang et al., 2011).

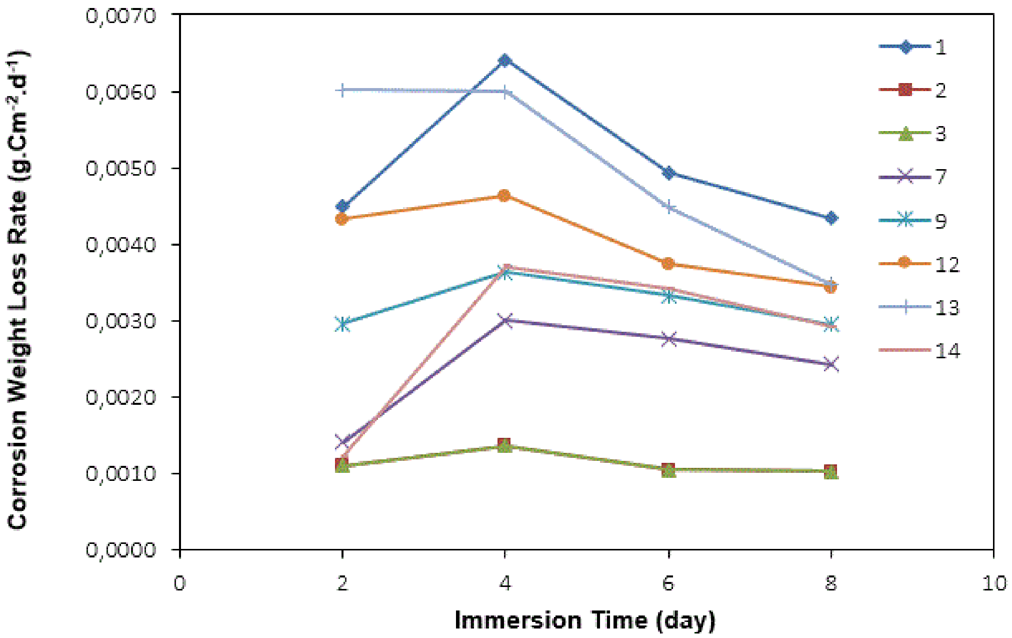

Figure 43: Corrosion weight loss rate in SBF at 37 °C in dynamic condition (n=3)

Figure 44 shows images of samples after 2 days of immersion in SBF. This figure clearly shows the formation of calcium phosphates on the surface of AZ91D-Mg plates. Also, formation of calcium phosphates decreases surface area of the samples so increased the corrosion resistance of plates. The corrosion weight loose rate was measured between 0.00102 and 0.00904 g.cm^{-2}.d^{-1} in this study. While, Zhang et al. reported the corrosion rate of Mg equal to 0.5 g.cm^{-2}.d^{-1} after 2 days immersion in NaCl (Zhang et al., 2011). This difference between corrosion rates can be explained by considering the high concentration of Cl^- in NaCl solution. An study confirmed that presence of Cl^- ions accelerated the corrosion of Mg and its alloys with increasing pitting corrosion rate (Zhang et al., 2013).

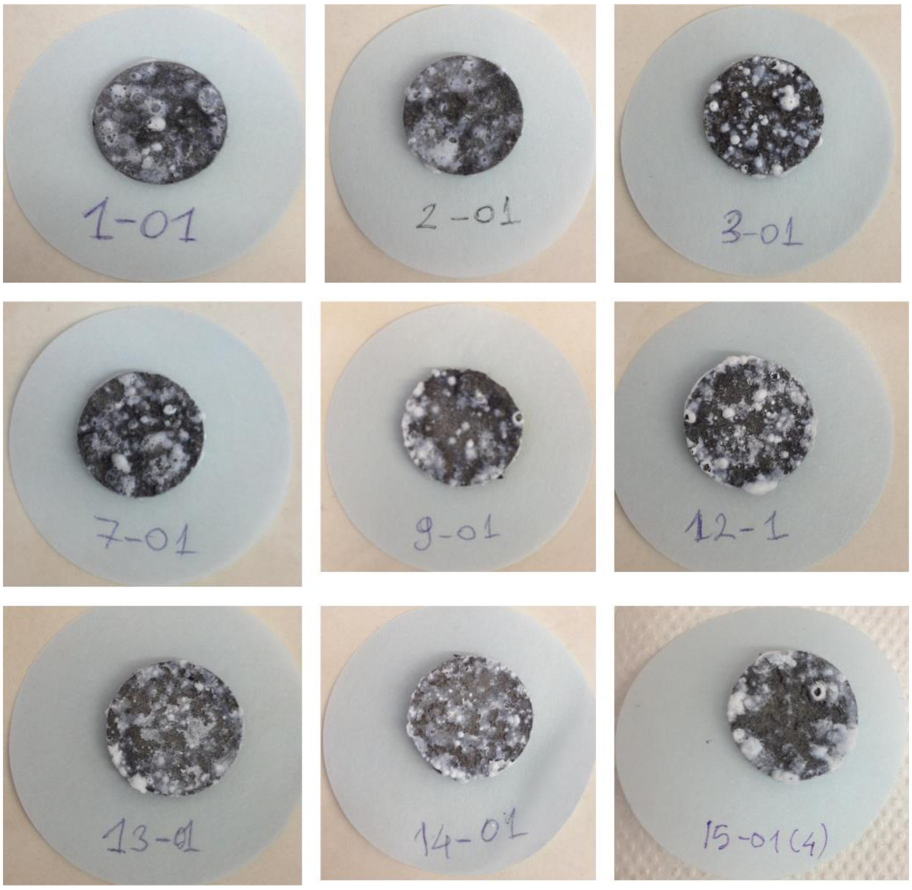

Figure 44: Images of AZ91D-Mg plates at the end of 2nd immersion in SBF

Figure 45 shows corrosion rate of AZ91D-Mg plates in SBF solution at the end of three different times (1, 4 and 8th day). Wang et al. verified that corrosion rate of Mg and its alloys slightly increased with increasing immersion time due to formation of cracks on the surface of immersed alloy (Wang et al., 2009). However, some of the samples (1, 2, 3, 7, 8 and 10) show negative corrosion rate which can be explained by considering the precipitation of calcium phosphates and other salts on the surface of plates (Fig. 45(a)). The precipitation of calcium phosphates and other salts on the surface may be accelerated by highly porous structure and textured surface of plates. Corrosion rate of other samples is in correlation with previous studies and corrosion rate of samples increased at the end of 8th day (Fig.45 (b)).

EDX analysis indicated the presence of Na, Cl, Ca and P ions on the surface of plates. Thus, negative corrosion rate of samples can be explained by considering the formation of a calcium phosphate protective layer and other salts which increase weight of the samples (Fig.44). Similarly, in another study, Mg showed a negative corrosion rate (Abidin et al., 2013).

Corrosion rate of Mg alloys was affected by microstructural properties such as grain size and phase distribution. Also, it was proved that presence of alloying element in pure or intermetallic form which act as a cathode accelerates the galvanic corrosion due to lower activity than Mg. In corrosion procedure of Mg alloys, α-Mg acts as an anode while other phases act as cathode.

High corrosion rate of Mg at first hours of immersion in SBF can be explained by considering to pH of solution. Previous studies proved that there is a great increase in pH at first hours of immersion of the samples in SBF. Following reactions are seen in first 24 hours of immersion:

$$2Mg + 4H_2O \rightarrow 2Mg^{2+} + 4OH^- + 2H_2 \qquad (8)$$

$$H_2CO_3 \leftrightarrow CO_2 + H_2O \qquad (9)$$

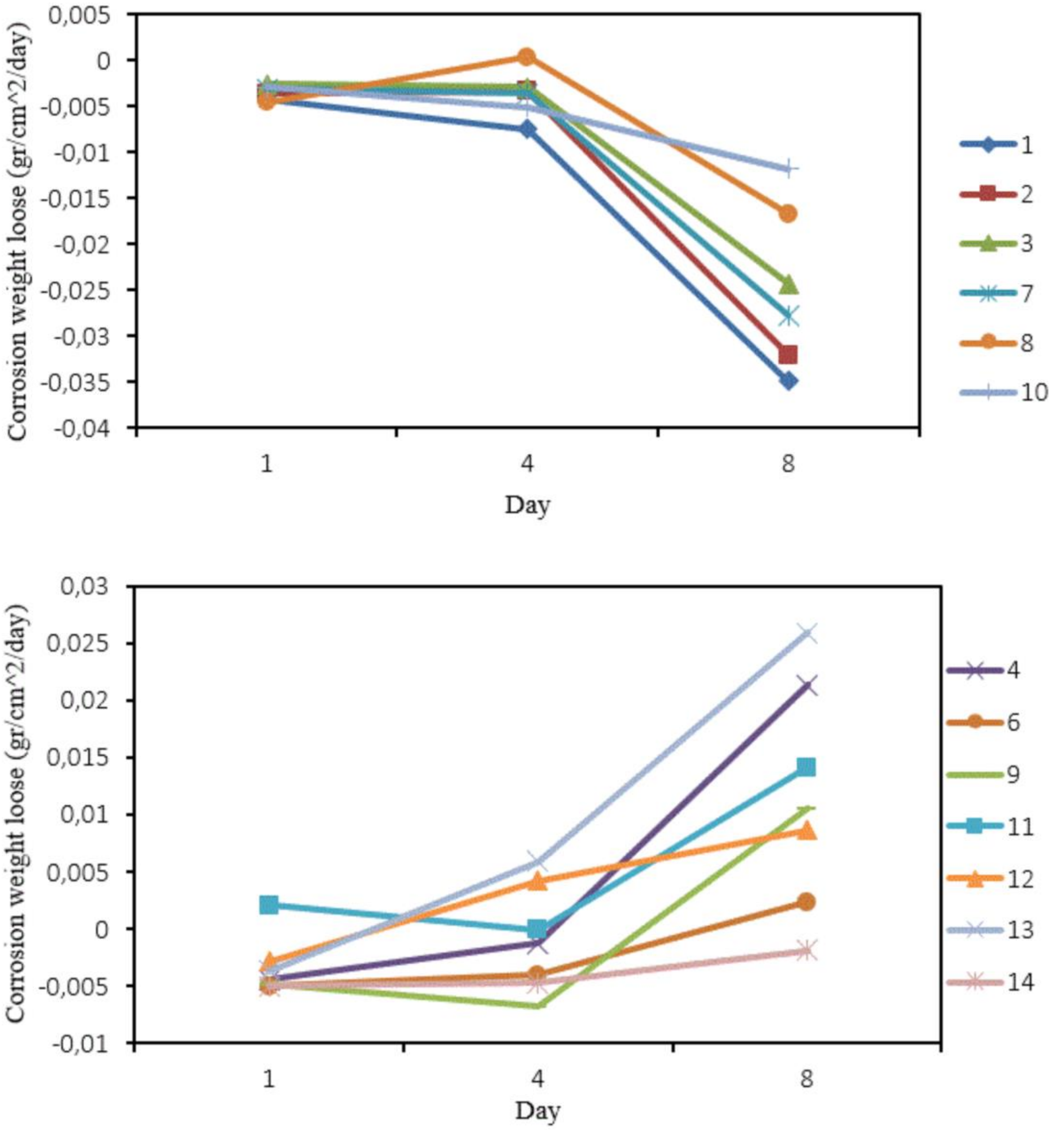

Figure 45: Corrosion rate of AZ91D-Mg plates at three time points in SBF

These two factors are reasons of a great increase in pH. Also, $Mg(OH)_2$ is not stable at the beginning of immersion process due to near to neutral pH of SBF. It is known that $Mg(OH)_2$ passive layer is stable at pHs above 10 while it is dissolved at acidic and neutral environment. However, this passive layer formed at relatively neutral pH due to localized increase in pH close to surface of Mg. The kinetics of dissolution of $Mg(OH)_2$ are lower than its formation kinetics so it can coat the Mg surface. $Mg(OH)_2$ has a protective layer so it is a weak passive layer. However, the formation of dehydrated $Mg(OH)_2$ has a considerable effect on corrosion rate of Mg.

It was reported that formation of MgO inner layer decreases the corrosion rate of Mg and its alloys in SBF. On the other hand, this passive layer is raptured by aggressive chloride ions present in SBF. The presence of Cl- ions resulted in dissolution of protective layer and accelerate pitting corrosion of Mg.

Formation of amorphous calcium phosphate layer on the surface of AZ91, AZ31, WE43 and LAE442 in vivo was reported (Witte et al., 2005). Also, Bornabpour et al. performed formation of $Mg(OH)_2$ and HA protective layer on the surface of pure Mg and Mg-Sr alloy in SBF (Bornapour et al., 2013).

3.4 Cell Culture Studies

3.4.1 Cell Viability

Cytotoxicity effect an AZ91D-Mg plates was investigated. Also, the effect of manufacturing parameters and surface texture on cell proliferation was detected. Figure 46 shows the morphology of h-FOB cells at 6th passage before seeding on plates.

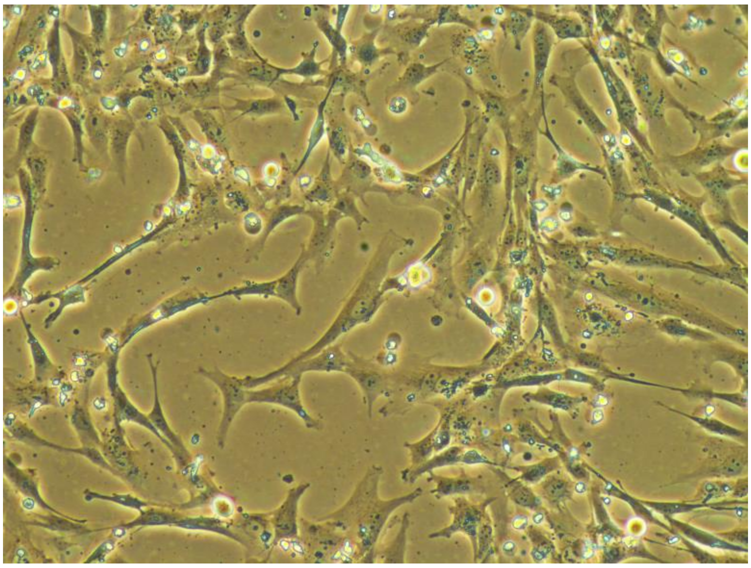

Figure 46: Phase contrast micrograph of h-Fob cells TCP

Viability of h-FOB cells seeded on implants was measured at the end of each time period. Cell viability percentage was calculated by comparing average absorbance of each sample with positive control group (h-FOB cells seeded on TCP). The cell viability percentage of each group is presented in Figure 47. According to Figure 47, there was no cytotoxicity effect in groups. The cell viability percentage of all plates was higher than 100% (more than control group) at the end of 7th day incubation. The cell percentage of plates with textured surface is lower than plates with smooth surface at the end of first day. However, this percentage showed great increase for textured surface at the end of 4th and 7th days. This can be explained that the initial cell attachment on these surface was lower compared to other groups at first day. Also, the cell viability of plates sintered for 3h was higher than that of plates sintered just for 1h at the end of 1th, 4th and 7th days. In addition, cell viability test proved that the plates compacted at 250 MPa showed higher cell viability than plates compacted at 300 MPa. This phenomena can be explained by considering the effect of compaction pressure on porosity of samples. It is known that porosity of plates is decreased by increasing compaction pressure. Thus, it can be concluded that porosity has a significant effect on cell proliferation. Samples with code numbers of C5 and C6 showed highest cell viability percentage at the end of 7th day. These samples have textured surface and they were compacted at 250 MPa so samples with higher porosity and textured surface had a positive effect on cell proliferation.

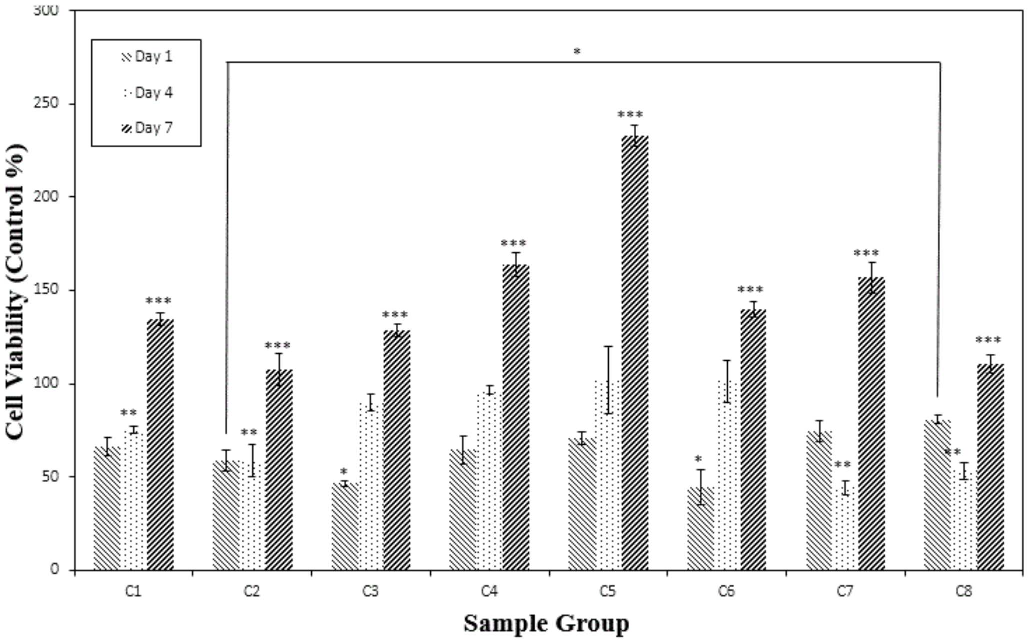

Figure 47: Response of h-FOB cells to smooth and micro-textured surface AZ91D-Mg implants. Cell viability monitored by Presto-Blue after 1, 3 and 7 days (n=3)

There was no decreasing trend in cell viability tests so it can be concluded that there is no cytotoxicity effect. Cell percentage on all plates except C7 and C8 was increased with increasing the incubation time. This can be resulted from achieving the confluency at the end of first day because these samples have smooth surface so the surface area of this samples is smaller than that of samples with textured surface. On the other hand, the cells proliferated to pores during this time period and cell percentage increased at the end of 7th day. Previous studies proved that cell percentage decreased as result of achieving to confluency (Zhang et al., 2014). Plates with code number of C5 and C6 showed biggest cell percentage at the end of 4th and 7th days. Thus, the textured surface improved the cell attachment and proliferation. It was proved that Mg implant with smooth surface declines cell attachment and proliferation while surface roughness improves cell attachment and proliferation (Abdal-hay et al., 2012). Porous and rough surfaces implants improve surface-cell integration due to high surface area (Pompa et al., 2015). Thus, this study is in correlation with previous studies (Abdal-hay et al., 2012; Zheng et al., 2014; Pompa et al., 2015).

The cell viability of plates at the end of 4th day did not show a significant difference in comparison to cell viability at the end of 1st day. This phenomena can be explained with considering to corrosion rate of plates in early stages of immersion. pH values of solution were highly increased at early stages of immersion due to the reaction of Cl^- ions with $Mg(OH)_2$ protective layer and formation of $MgCl_2$ and OH^- which are resulted in increasing of pH (Zhang et al., 2013). It is known that the high pH value (>9.18) has a negative effect on cellular activity (Zhang et al., 2014; Pompa et al., 2015). On the other hand, HA was precipitated on the surface of Mg implants due to the high pH value and presence of Ca^{2+} and PO_4^{3-} in solution which promoted osteoconductivity and osteoinductivity (Zhang et al., 2013). Furthermore, the enormous amount of Mg^{2+} ions resulted in formation of complex compounds such as Mg_xCa_y (PO_4) on the surface of Mg-based implants (Zhang et al., 2013).

The cell viability test shows significant increase in cell number at the end of 7th day. This phenomena can be explained by consideration to the fact that releasing of Mg^{2+} ions increase new bone formation (Witte et al., 2005). Previous studies proved that Mg^{2+} cations increase osteoblast cell activity and take part in synthesis of nucleic acids (Witte et al., 2005). Moreover, Mg is one of the most important component of the ribosomal machinery. The ribosomal machinery translates the genetic information into polypeptide structures (Witte et al., 2005). Thus, it can be concluded that the high concentration of Mg resulted in an increase at osteoid deposition around the degraded Mg implant (Witte et al., 2005). Furthermore, precipitation of apatite like structures increased the cell proliferation. As a result, presence of Mg ions in environment and precipitation of calcium phosphates enhance h-FOB cells proliferation.

3.4.2 Cell Morphology

The morphology of h-FOB cells was investigated with SEM after 1 day incubation in humidified environment at 37°C. Figure 48 shows morphology of cells at the end of 1st day. Also, precipitation of salts and some corrosion products such as calcium phosphates and other salts was observed. Additionally, cell grows from surface to pores and cracks were observed in SEM. Thus, cell attachment and proliferation clearly were observed on the surface of AZ91D-Mg plates.

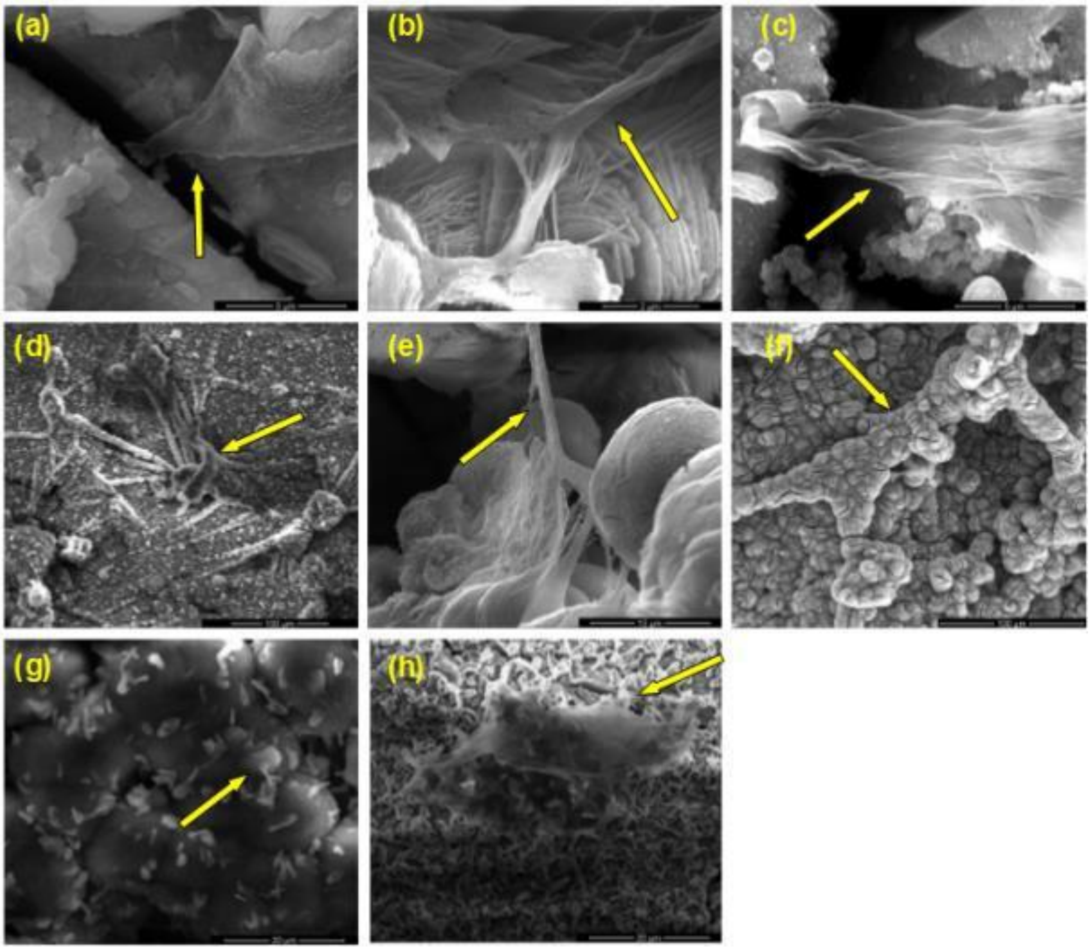

Figure 48: Morphology of h-FOB cells on the surface of AZ91D-Mg plates at the end of 1st day (a) sample #C1; (b) sample #C2; (c) sample #C3; (d) sample #C4; (e) sample #C5; (f) sample #C6; (g) sample #C7; and (h) sample #C8

Figure 49 shows morphology of h-FOB cells on AZ91D-Mg plates at the end of 7th day. The effect of surface texture on cell morphology was observed in SEM images. EDX analysis proved the presence of C, Ca, P and metal oxides on the surface of plates. The presence of C elements is proved presence of cells on the surface of plates. Also, EDX analysis proved that the spherical particles on the surface of plates are magnesium and aluminum oxides.

SEM images showed that cells were spread all over the surface of textured plates while h-FOB cells were accumulated near to seeding region. Previous studies proved the effect of patterned surface on cell growth and attachment (Mirhosseini et al., 2007). The 2T3 osteoblast cells accumulated on the surface of Ti implant with smooth surface but uniformly spread on the surface of patterned Ti implants (Mirhosseini et al., 2007).

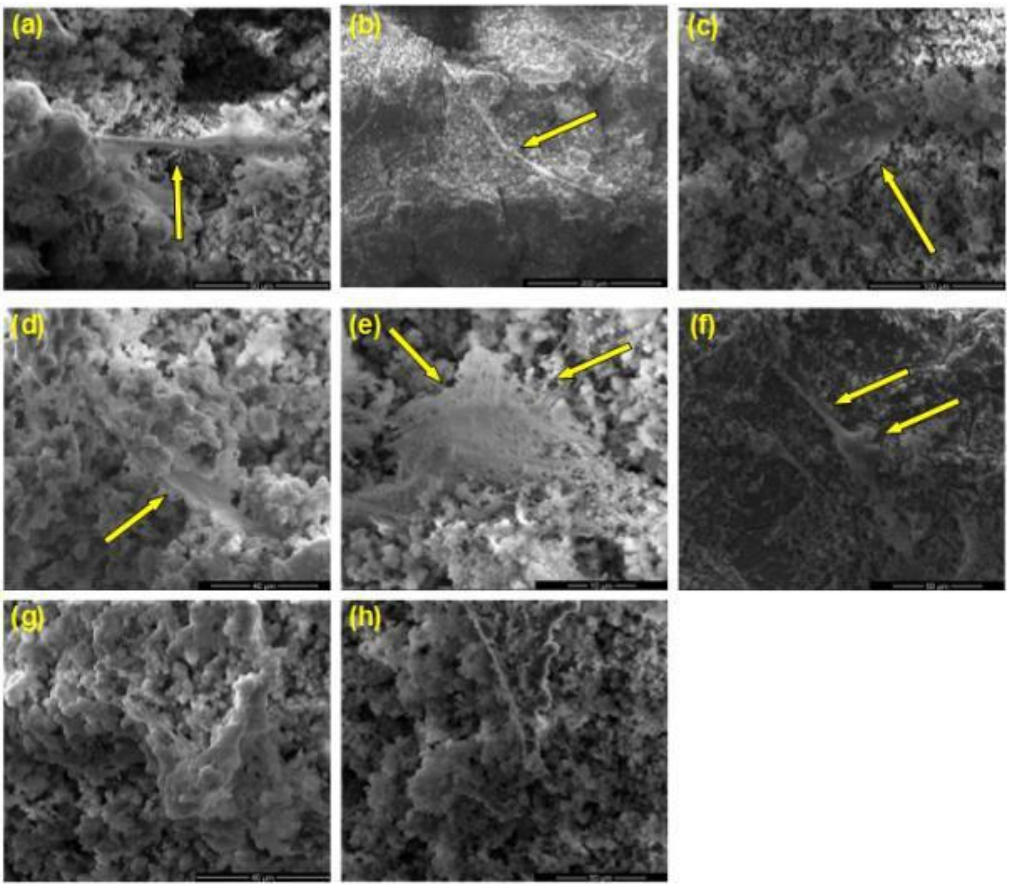

Figure 49: Morphology of h-FOB cells on the surface of AZ91D-Mg plates at the end of 7th day (a) sample #C1; (b) sample #C2; (c) sample #C3; (d) sample #C4; (e) sample #C5; (f) sample #C6; (g) sample #C7; and (h) sample #C8

Figure 50 shows the SEM images of sample with code number of C5 at the end of 7th day in four different magnifications (100X, 1600X, 3000X and 6000X). The surface of C5 was completely covered by h-FOB cells and also there is no cell accumulation on specific area. Thus, the textured surface and surface roughness positively affected cell attachment and proliferation. Also, salt particles were observed on the surface of plate but these particles has no negative effect on cell viability. Moreover, the cells show needle like protrusion around the salt particles on surface.

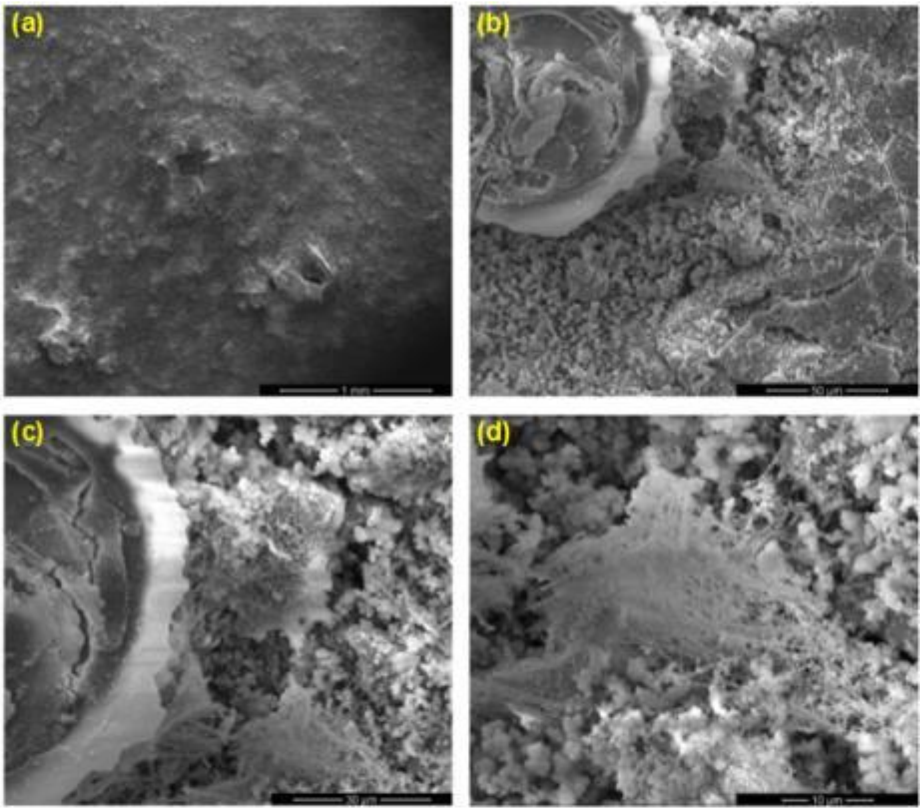

Figure 50: SEM images of surface of sample #5 at the end of 7th day (a) 100X, (b) 1600X, (c) 3000X and (d) 6000X

3.4.3 Confocal Microscope Analysis of Cells

The seeded samples which were stained by phalloidin-FITC dye were investigated to analysis effect of surface texture on cell behavior after incubation for 1st and 7th days at 37°C. According to Figure 51, there is no difference between cells alignment at the end of 1st day and cells were attached to surface of plates with smooth and textured structured. However, there is a significant difference between cell morphology and alignment for plates with smooth and textured surface after 7th day incubation (Figure 52).

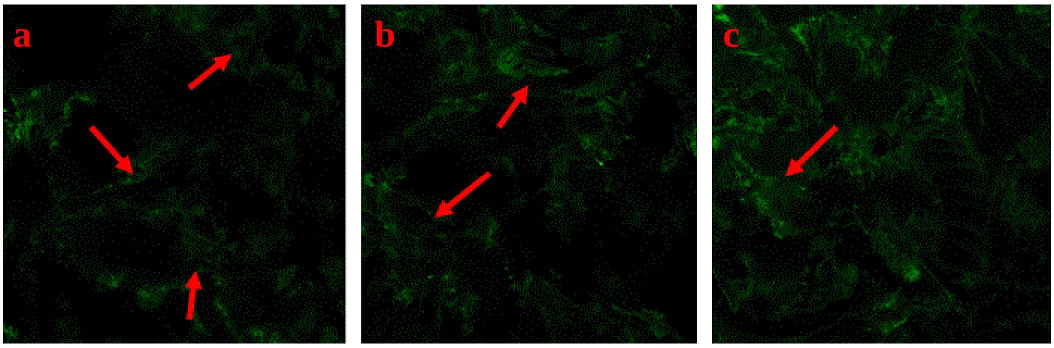

Figure 51: Fluorescence microscopy of h-FOB cells were seeded on: a) sample #C5; b) sample #C6; and c) sample #C7 after incubation for 1 day

Fluorescence microscopy results showed that h-FOB cells were aligned along the channels for the samples with textured surface while in smooth surface cells are accumulated in areas near to seeding region. Thus, it can be proved that pseudopodia's extended along the channels and surface textured play significant role in pseudopodia extension. Previous studies proved that pattern structures improve cell spreading in comparison with smooth surface (Riedel et al., 2011; Dumas et al., 2012; Liang et al., 2013; Wittenbrink et al., 2015).

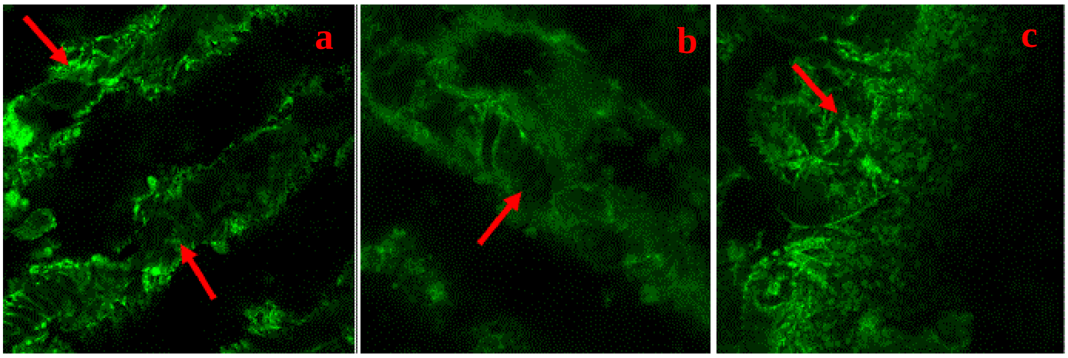

Figure 52: Fluorescence microscopy of h-FOB cells were seeded on: a) sample #C5; b) sample #C6; and c) sample #C7 after incubation for 7th day

Riedel et al. showed that repeated pattern on surface of Ti based implant improves mesenchymal stem cell spreading and also cells aligned along the pattern (Riedel et al., 2011). Also, it was proved aspect ratio of textures has significant effect on pseudopodia extension so cell alignment (Riedel et al., 2011). They showed that increasing aspect ratio from 24 to 175 nm decreased extension of pseudopodia (Riedel et al., 2011). In other study, it was observed that low aspect ratio have negative effect on osteoblast like cells alignment and there was no cell alignment on implant with aspect ratio between 190 to 240 nm (Fassbender et al., 2009). Thus, it can be concluded that aspect ratio is a significant factor in cell alignment parallel to channels.

3.4.4 ALP Activity Analysis

Figure 53 shows ALP activity of h-FOB cells on AZ91D-Mg plates at the end of 7th and 14th day. It is known that osteoblast cells secret ALP in the stage of active bone deposition so ALP used as early marker for bone formation and osteoblastic activity. ALP assay was applied to investigate effect of AZ91D-Mg on osteogenic differentiation of h-FOB cells. It was observed that ALP activity of all of the samples at 14th day were higher than 7th day. Thus, it can be concluded that cell osteogenic differentiation of h-FOB cells continued in all of groups. Surface microstructure, roughness and porous structure of plates play important roles in increasing of osteogenic differentiation of the cells up to 14^{th} day. Results are in agreement with further studies in which surface roughness and porosity improve ALP activity (Moon et al., 2014; Park et al., 2015).

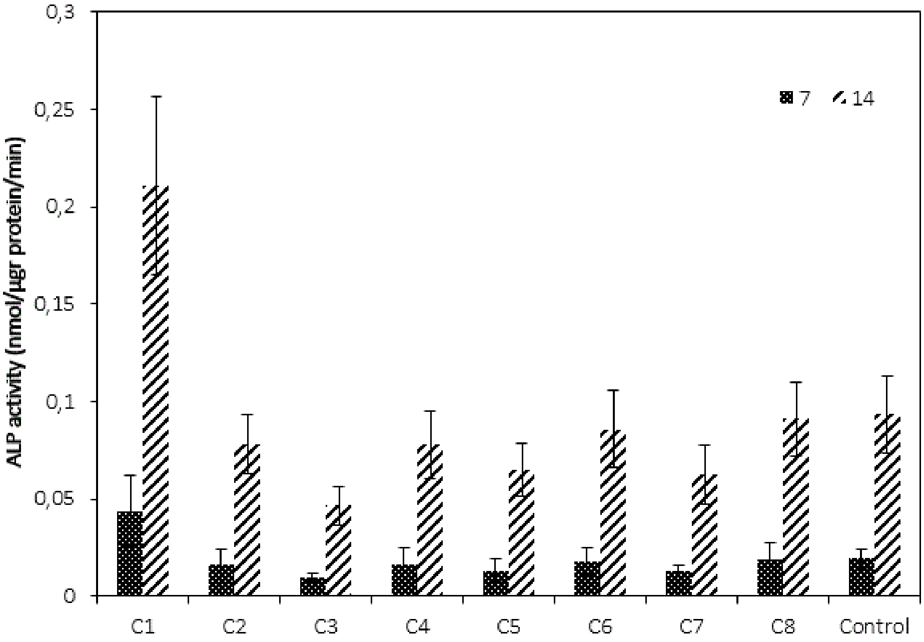

Figure 53: ALP activity of h-FOB cells seeded on AZ91D-Mg plates

ALP activity of plates compacted at 300 MPa is higher than that of samples compacted at 250 MPa. It is known that the compaction pressure has a significant effect on hardness of samples in which hardness value is increased with increasing compaction pressure. Thus, plates compacted at higher pressure show most similarity to bone tissue. Previous studies proved high hardness value enhances osteogenic cell differentiation (Coelho and Jimbo, 2014; Chen and Thouas, 2015). The sample #C1 clearly shows the highest ALP activity among the samples. Furthermore, micro textures on the surface of implants enhance cellular activity due to increasing of surface area of implants (Jabur, 2013; Moon et al., 2014; Park et al., 2015). Moreover, sintering time was affected ALP activity in which the increasing of sintering time results in a decrease in cellular activity. It is known that the increasing of sintering time gives time to further increase in grain size so the pore size collapse decrease as a result. Thus, pore size has significant effect on osteogenic cell differentiation.

CHAPTER 4

CONCLUSION

AZ91D-Mg biomedical implants were manufactured by PM under various manufacturing conditions and then employed physical, mechanical, corrosion analysis and cell culture studies. The effect of compaction pressure, sintering temperature and time on physical, mechanical and corrosion properties of Mg alloy plates was investigated. It was concluded that compaction pressure had a significant effect on the relative density. Sintering temperature and time affected negatively the bending strength. The confocal microscope results proved that surface roughness is decreased with increasing the compaction pressure so the surface roughness can be controlled with compaction pressure. Furthermore, it was demonstrated that the desired surface micro structure was successfully manufactured by PM route. Due to higher Cl^- ions content, Hank's solution not only induced lower corrosion potential than DMEM and 10%FBS+DMEM solutions but also showed lower pitting corrosion potential. Beyond that, the plates with smooth surface showed lower corrosion potential than the plates with textured surface in the presence of FBS that was important due to the positive effect of porous surfaces on cell attachment and proliferation. Moreover, immersion tests which conducted in SBF proved that corrosion rate of plates was decreased by formation of protective layers such as calcium phosphates on the surface of immersed plates. Also, formation of calcium phosphates has positive effect on cell adhesion and proliferation. Corresponding to cell viability analysis, AZ91D-Mg biomedical implants exhibit high degree of biocompatibility. Furthermore, the plates with higher porosity and micro texture surface increased cell adhesion and proliferation. Also, surface roughness plays an important role in cellular activity of h-FOB cells. The h-FOB cells spread all over the plates with micro texture surface while the cells accumulated around seeding area for plates with smooth surface. It can be concluded that PM can be regarded as a biomedical implant manufacturing technique for its ability to manufacture products with high mechanical integrity and complex surface shapes. Beyond that, it was proved that corrosion rate of AZ91D-Mg alloy can be controlled by surface modification. Moreover, cell culture studies recommended that AZ91D-Mg is a good candidate as a biodegradable bone implant.

REFERENCES

A. Abdal-hay, M. Dewidar and J. K. Lim (2012). "Biocorrosion behavior and cell viability of adhesive polymer coated magnesium based alloys for medical implants." Applied Surface Science **261**: 536-546.

N. I. Z. Abidin, B. Rolfe, H. Owen, J. Malisano, D. Martin, J. Hofstetter, P. J. Uggowitzer and A. Atrens (2013). "The in vivo and in vitro corrosion of high-purity magnesium and magnesium alloys WZ21 and AZ91." Corrosion Science **75**: 354-366.

A. Ahmed and H. Rashed (2014). "Effects of niobium doping on microstructure of BaTiO3 based ceramics." International Journal of Scientific & Engineering Research **5**(13): 790-797.

R. B. Alvarez, H. J. Martin, M. Horstemeyer, M. Q. Chandler, N. Williams, P. T. Wang and A. Ruiz (2010). "Corrosion relationships as a function of time and surface roughness on a structural AE44 magnesium alloy." Corrosion Science **52**(5): 1635-1648.

D. C. Andersson, P. Lindskog, H. Staf and P. L. Larsson (2014). "A Numerical Study of Material Parameter Sensitivity in the Production of Hard Metal Components Using Powder Compaction." Journal of Materials Engineering and Performance **23**(6): 2199-2208.

K. Apedo, C. Munzer, H. He, P. Montgomery, N. Serres, C. Fond and F. Feugeas (2015). "Cement paste surface roughness analysis using coherence scanning interferometry and confocal microscopy." Materials Characterization **100**: 108-119.

R. Arrabal, B. Mingo, A. Pardo, M. Mohedano, E. Matykina and I. Rodríguez (2013). "Pitting corrosion of rheocast A356 aluminium alloy in 3.5 wt.% NaCl solution." Corrosion Science **73**: 342-355.

M. Bamberger and G. Dehm (2008). "Trends in the development of new Mg alloys." Annual Reviews of Materials Research **38**: 505-533.

P. Bartolo, J.-P. Kruth, J. Silva, G. Levy, A. Malshe, K. Rajurkar, M. Mitsuishi, J. Ciurana and M. Leu (2012). "Biomedical production of implants by additive electro-chemical and physical processes." CIRP Annals-Manufacturing Technology **61**(2): 635-655.

S. Bauer, P. Schmuki, K. von der Mark and J. Park (2013). "Engineering biocompatible implant surfaces: Part I: Materials and surfaces." Progress in Materials Science **58**(3): 261-326.

A. Biesiekierski, J. Wang, M. A. H. Gepreel and C. Wen (2012). "A new look at biomedical Ti-based shape memory alloys." Acta Biomaterialia **8**(5): 1661-1669.

C. Boland, R. Hexemer, I. Donaldson and D. Bishop (2013). "Industrial processing of a novel Al–Cu–Mg powder metallurgy alloy." Materials Science and Engineering: A **559**: 902-908.

L. Bolzoni, T. Weissgaerber, B. Kieback, E. M. Ruiz Navas and E. Gordo (2013). "Mechanical behaviour of pressed and sintered CP Ti and Ti–6Al–7Nb alloy obtained from master alloy addition powder." Journal of the Mechanical Behavior of Biomedical Materials **20**: 149-161.

M. Bornapour, N. Muja, D. Shum Tim, M. Cerruti and M. Pekguleryuz (2013). "Biocompatibility and biodegradability of Mg–Sr alloys: The formation of Sr-substituted hydroxyapatite." Acta Biomaterialia **9**(2): 5319-5330.

R. Brånemark, L. Emanuelsson, A. Palmquist and P. Thomsen (2011). "Bone response to laser-induced micro-and nano-size titanium surface features." Nanomedicine: Nanotechnology, Biology and Medicine **7**(2): 220-227.

J. Čapek and D. Vojtěch (2014). "Effect of sintering conditions on the microstructural and mechanical characteristics of porous magnesium materials prepared by powder metallurgy." Materials Science and Engineering: C **35**: 21-28.

A. Chaya, S. Yoshizawa, K. Verdelis, N. Myers, B. J. Costello, D.-T. Chou, S. Pal, S. Maiti, P. N. Kumta and C. Sfeir (2015). "In vivo study of magnesium plate and screw degradation and bone fracture healing." Acta Biomaterialia **18**: 262-269.

C. Chen, C. Chu, J. Yang, C. Bao, G. Qiao, D. Tian, B. Wang, K. Ishizaki and K. Niihara (2011). "Effect of raw materials on microstructure and bending strength of porous in situ MgO/Fe–Cr–Ni composites." Materials Science and Engineering: A **528**(29): 8438-8442.

Q. Chen and G. A. Thouas (2015). "Metallic implant biomaterials." Materials Science and Engineering: R: Reports **87**: 1-57.

Y. Chen, Z. Xu, C. Smith and J. Sankar (2014). "Recent advances on the development of magnesium alloys for biodegradable implants." Acta Biomaterialia **10**(11): 4561-4573.

J. Cheng, B. Liu, Y. Wu and Y. Zheng (2013). "Comparative in vitro study on pure metals (Fe, Mn, Mg, Zn and W) as biodegradable metals." Journal of Materials Science & Technology **29**(7): 619-627.

J. Cheng and Y. Zheng (2013). "In vitro study on newly designed biodegradable Fe‑X composites (X= W, CNT) prepared by spark plasma sintering." Journal of Biomedical Materials Research Part B: Applied Biomaterials **101**(4): 485-497.

S. Chikosha, T. Shabalala and H. Chikwanda (2014). "Effect of particle morphology and size on roll compaction of Ti-based powders." Powder Technology **264**: 310-319.

Z. Chun Yan, Z. Rong Chang, L. Cheng Long and G. Jia Cheng (2010). "Comparison of calcium phosphate coatings on Mg–Al and Mg–Ca alloys and their corrosion behavior in Hank's solution." Surface and Coatings Technology **204**(21): 3636-3640.

P. G. Coelho and R. Jimbo (2014). "Osseointegration of metallic devices: Current trends based on implant hardware design." Archives of Biochemistry and Biophysics **561**: 99-108.

J. D. Currey (1999). "The design of mineralised hard tissues for their mechanical functions." Journal of Experimental Biology **202**(23): 3285-3294.

W. Daogao, Y. Shihong, W. Zhiqiang, Z. Zhang, M. Ruiying, X. Zhang and C. Dehong (2014). "Effect of samarium on microstructure and corrosion resistance of aged as-cast AZ92 magnesium alloy." Journal of Rare Earths **32**(7): 663-671.

E. Davim, M. Fernandes and A. Senos (2015). "Increased surface area during sintering of calcium phosphate glass and sodium chloride mixtures." Journal of the European Ceramic Society **35**(1): 329-336.

D. D. Deligianni, N. Katsala, S. Ladas, D. Sotiropoulou, J. Amedee and Y. Missirlis (2001). "Effect of surface roughness of the titanium alloy Ti–6Al–4V on human bone marrow cell response and on protein adsorption." Biomaterials **22**(11): 1241-1251.

K. Diao, Z. Xiao and Y. Zhao (2015). "Specific surface areas of porous Cu manufactured by Lost Carbonate Sintering: Measurements by quantitative stereology and cyclic voltammetry." Materials Chemistry and Physics **162**: 571-579.

S. V. Dorozhkin (2014). "Calcium orthophosphate coatings on magnesium and its biodegradable alloys." Acta Biomaterialia **10**(7): 2919-2934.

H. Du, Z. Wei, H. Wang, E. Zhang, L. Zuo and L. Du (2011). "Surface microstructure and cell compatibility of calcium silicate and calcium phosphate composite coatings on Mg–Zn–Mn–Ca alloys for biomedical application." Colloids and Surfaces B: Biointerfaces **83**(1): 96-102.

V. Dumas, A. Rattner, L. Vico, E. Audouard, J. C. Dumas, P. Naisson and P. Bertrand (2012). "Multiscale grooved titanium processed with femtosecond laser influences mesenchymal stem cell morphology, adhesion, and matrix organization." Journal of Biomedical Materials Research Part A **100**(11): 3108-3116.

H. E. Exner and E. Arzt (1990). Sintering processes. Netherlands, Springer.

J. Fan, X. Qiu, X. Niu, Z. Tian, W. Sun, X. Liu, Y. Li, W. Li and J. Meng (2013). "Microstructure, mechanical properties, in vitro degradation and cytotoxicity evaluations of Mg–1.5 Y–1.2 Zn–0.44 Zr alloys for biodegradable metallic implants." Materials Science and Engineering: C **33**(4): 2345-2352.

J. Fassbender, T. Strache, M. Liedke, D. Markó, S. Wintz, K. Lenz, A. Keller, S. Facsko, I. Mönch and J. McCord (2009). "Introducing artificial length scales to tailor magnetic properties." New Journal of Physics **11**(12): 125002.

A. Francis, Y. Yang, S. Virtanen and A. Boccaccini (2015). "Iron and iron-based alloys for temporary cardiovascular applications." Journal of Materials Science: Materials in Medicine **26**(3): 1-16.

G. Fu and W. Soboyejo (2009). "Cell/surface interactions of human osteo-sarcoma (HOS) cells and micro-patterned polydimelthylsiloxane (PDMS) surfaces." Materials Science and Engineering: C **29**(6): 2011-2018.

C. Garcia, F. Martin, Y. Blanco, M. De Tiedra and M. Aparicio (2009). "Corrosion behaviour of duplex stainless steels sintered in nitrogen." Corrosion Science **51**(1): 76-86.

C. García, F. Martín, P. De Tiedra and L. G. Cambronero (2007). "Pitting corrosion behaviour of PM austenitic stainless steels sintered in nitrogen–hydrogen atmosphere." Corrosion Science **49**(4): 1718-1736.

J. Geis-Gerstorfer, C. Schille, E. Schweizer, F. Rupp, L. Scheideler, H.-P. Reichel, N. Hort, A. Nolte and H.-P. Wendel (2011). "Blood triggered corrosion of magnesium alloys." Materials Science and Engineering: B **176**(20): 1761-1766.

R. A. Gittens, T. McLachlan, R. Olivares-Navarrete, Y. Cai, S. Berner, R. Tannenbaum, Z. Schwartz, K. H. Sandhage and B. D. Boyan (2011). "The effects of combined micron-/submicron-scale surface roughness and nanoscale features on cell proliferation and differentiation." Biomaterials **32**(13): 3395-3403.

C. A. Grillo, F. Alvarez and M. A. F. L. de Mele (2014). "Cellular response to rare earth mixtures (La and Gd) as components of degradable Mg alloys for medical applications." Colloids and Surfaces B: Biointerfaces **117**: 312-321.

X. Gu, N. Li, Y. Zheng and L. Ruan (2011). "In vitro degradation performance and biological response of a Mg–Zn–Zr alloy." Materials Science and Engineering: B **176**(20): 1778-1784.

X. Gu, Y. Zheng and L. Chen (2009). "Influence of artificial biological fluid composition on the biocorrosion of potential orthopedic Mg–Ca, AZ31, AZ91 alloys." Biomedical Materials **4**(6): 065011.

S. Guo, A. Chu, H. Wu, C. Cai and X. Qu (2014). "Effect of sintering processing on microstructure, mechanical properties and corrosion resistance of Ti–24Nb–4Zr–7.9 Sn alloy for biomedical applications." Journal of Alloys and Compounds **597**: 211-216.

A. Happe, N. Röling, A. Schäfer and D. Rothamel (2015). "Effects of different polishing protocols on the surface roughness of Y-TZP surfaces used for custom-made implant abutments: A controlled morphologic SEM and profilometric pilot study." The Journal of Prosthetic Dentistry **113**(5): 440-447.

H. Hermawan, D. Dubé and D. Mantovani (2010). "Developments in metallic biodegradable stents." Acta Biomaterialia **6**(5): 1693-1697.

S. Hiromoto, E. Onodera, A. Chiba, K. Asami and T. Hanawa (2005). "Microstructure and corrosion behaviour in biological environments of the new forged low-Ni Co–Cr–Mo alloys." Biomaterials **26**(24): 4912-4923.

B. Homayun and A. Afshar (2014). "Microstructure, mechanical properties, corrosion behavior and cytotoxicity of Mg–Zn–Al–Ca alloys as biodegradable materials." Journal of Alloys and Compounds **607**: 1-10.

D. Hong, P. Saha, D.-T. Chou, B. Lee, B. E. Collins, Z. Tan, Z. Dong and P. N. Kumta (2013). "In vitro degradation and cytotoxicity response of Mg–4% Zn–0.5% Zr (ZK40) alloy as a potential biodegradable material." Acta Biomaterialia **9**(10): 8534-8547.

A. S. Jabur (2013). "Effect of powder metallurgy conditions on the properties of porous bronze." Powder Technology **237**: 477-483.

M. B. Kannan (2010). "Influence of microstructure on the in-vitro degradation behaviour of magnesium alloys." Materials Letters **64**(6): 739-742.

R. Kumar, S. Seetharamu and M. Kamaraj (2014). "Quantitative evaluation of 3D surface roughness parameters during cavitation exposure of 16Cr–5Ni hydro turbine steel." Wear **320**: 16-24.

Y. Lai, H. Huang, Q. Huang, H. Zhang and Z. Guo (2014). "Optimization of the experimental conditions for the synthesis of micro-size monodisperse spherical silver powders using Box–Behnken design." Powder Technology **263**: 7-13.

S. P. Lake, S. Ray, A. M. Zihni, D. M. Thompson, J. Gluckstein and C. R. Deeken (2015). "Pore size and pore shape–but not mesh density–alter the mechanical strength of tissue ingrowth and host tissue response to synthetic mesh materials in a porcine model of ventral hernia repair." Journal of the Mechanical Behavior of Biomedical Materials **42**: 186-197.

J. Lévesque, H. Hermawan, D. Dubé and D. Mantovani (2008). "Design of a pseudo-physiological test bench specific to the development of biodegradable metallic biomaterials." Acta Biomaterialia **4**(2): 284-295.

F. Li, J. Li, G. Xu, G. Liu, H. Kou and L. Zhou (2015). "Fabrication, pore structure and compressive behavior of anisotropic porous titanium for human trabecular bone implant applications." Journal of the Mechanical Behavior of Biomedical Materials **46**: 104-114.

J.-Y. Li, J.-X. Xie, J.-B. Jin and Z.-X. Wang (2012). "Microstructural evolution of AZ91 magnesium alloy during extrusion and heat treatment." Transactions of Nonferrous Metals Society of China **22**(5): 1028-1034.

Y. Li, C. Wen, D. Mushahary, R. Sravanthi, N. Harishankar, G. Pande and P. Hodgson (2012). "Mg–Zr–Sr alloys as biodegradable implant materials." Acta Biomaterialia **8**(8): 3177-3188.

C. Liang, H. Wang, J. Yang, Y. Cai, X. Hu, Y. Yang, B. Li, H. Li, H. Li and C. Li (2013). "Femtosecond laser-induced micropattern and Ca/P deposition on Ti implant surface and its acceleration on early osseointegration." ACS applied materials & interfaces **5**(16): 8179-8186.

P. Liang, H. L. Su, P. Donnadieu, M. G. Harmelin, A. Quivy, P. Ochin, G. Effenberg, H. J. Seifert, H. L. Lukas and F. Aldinger (1998). "Experimental investigation and thermodynamic calculation of the central part of the Mg-Al phase diagram." Zeitschrift für Metallkunde **89**(8): 536-540.

D. J. Lin, M. T. Tsai, T. M. Shieh, H. L. Huang, J. T. Hsu, Y. C. Ko and L. J. Fuh (2013). "In vitro antibacterial activity and cytocompatibility of bismuth doped micro-arc oxidized titanium." Journal of Biomaterials Applications **27**(5): 553-563.

C. Liu, Y. Wang, R. Zeng, X. Zhang, W. Huang and P. Chu (2010). "In vitro corrosion degradation behaviour of Mg–Ca alloy in the presence of albumin." Corrosion Science **52**(10): 3341-3347.

L. Liu and M. Schlesinger (2009). "Corrosion of magnesium and its alloys." Corrosion Science **51**(8): 1733-1737.

W. Liu, F. Cao, L. Chang, Z. Zhang and J. Zhang (2009). "Effect of rare earth element Ce and La on corrosion behavior of AM60 magnesium alloy." Corrosion Science **51**(6): 1334-1343.

I. Lozzi, A. Pucci, O. Pantani, L. D'Acqui and L. Calamai (2008). "Interferences of suspended clay fraction in protein quantitation by several determination methods." Analytical Biochemistry **376**(1): 108-114.

S. Luo, Y. Yang, G. Schaffer and M. Qian (2014). "Warm die compaction and sintering of titanium and titanium alloy powders." Journal of Materials Processing Technology **214**(3): 660-666.

Y. Miao, L. Yaohui, L. Jiaan and S. Yulai (2014). "Corrosion and mechanical properties of AM50 magnesium alloy after being modified by 1 wt.% rare earth element gadolinium." Journal of Rare Earths **32**(6): 558-563.

N. Mirhosseini, P. Crouse, M. Schmidth, L. Li and D. Garrod (2007). "Laser surface micro-texturing of Ti–6Al–4V substrates for improved cell integration." Applied Surface Science **253**(19): 7738-7743.

T. Miyazawa, Y. Kobayashi, A. Kamegawa, H. Takamura and M. Okada (2004). "Grain size refinements of Mg Alloys (AZ61, AZ91, ZK60) by HDDR treatment." Materials Transactions **45**(2): 384-387.

M. Moazami-Goudarzi and F. Akhlaghi (2013). "Effect of nanosized SiC particles addition to CP Al and Al–Mg powders on their compaction behavior." Powder Technology **245**: 126-133.

D. C. Montgomery (2008). Design and analysis of experiments, John Wiley & Sons.

S.-K. Moon, J.-S. Kwon, S.-H. Uhm, E.-J. Lee, H.-J. Gu, T.-G. Eom and K.-N. Kim (2014). "Biological evaluation of micro–nano patterned implant formed by anodic oxidation." Current Applied Physics **14**: S183-S187.

M. Moravej and D. Mantovani (2011). "Biodegradable metals for cardiovascular stent application: interests and new opportunities." International Journal of Molecular Sciences **12**(7): 4250-4270.

M. Moravej, F. Prima, M. Fiset and D. Mantovani (2010). "Electroformed iron as new biomaterial for degradable stents: Development process and structure–properties relationship." Acta Biomaterialia **6**(5): 1726-1735.

E. Mostaed, M. Hashempour, A. Fabrizi, D. Dellasega, M. Bestetti, F. Bonollo and M. Vedani (2014). "Microstructure, texture evolution, mechanical properties and corrosion behavior of ECAP processed ZK60 magnesium alloy for biodegradable applications." Journal of the Mechanical Behavior of Biomedical Materials **37**: 307-322.

C. M. Murphy, M. G. Haugh and F. J. O'Brien (2010). "The effect of mean pore size on cell attachment, proliferation and migration in collagen–glycosaminoglycan scaffolds for bone tissue engineering." Biomaterials **31**(3): 461-466.

D. Mushahary, C. Wen, J. M. Kumar, J. Lin, N. Harishankar, P. Hodgson, G. Pande and Y. Li (2014). "Collagen type-I leads to in vivo matrix mineralization and secondary stabilization of Mg–Zr–Ca alloy implants." Colloids and Surfaces B: Biointerfaces **122**: 719-728.

N. Nam, M. Bian, M. Forsyth, M. Seter, M. Tan and K. Shin (2012). "Effect of calcium oxide on the corrosion behaviour of AZ91 magnesium alloy." Corrosion Science **64**: 263-271.

J. B. Park and J. D. Bronzino (2002). Biomaterials: Principles and Applications. USA, CRC Press.

S. W. Park, D. Lee, H. R. Lee, H.-J. Moon, B. R. Lee, W.-K. Ko, S.-J. Song, S. J. Lee, K. Shin and W. Jang (2015). "Generation of functionalized polymer nanolayer on implant surface via initiated chemical vapor deposition (iCVD)." Journal of Colloid and Interface Science **439**: 34-41.

Q. Peng, Y. Huang, L. Zhou, N. Hort and K. U. Kainer (2010). "Preparation and properties of high purity Mg–Y biomaterials." Biomaterials **31**(3): 398-403.

Q. Peng, J. Meng, Y. Li, Y. Huang and N. Hort (2011). "Effect of yttrium addition on lattice parameter, Young's modulus and vacancy of magnesium." Materials Science and Engineering: A **528**(4): 2106-2109.

M. Peuster, C. Hesse, T. Schloo, C. Fink, P. Beerbaum and C. von Schnakenburg (2006). "Long-term biocompatibility of a corrodible peripheral iron stent in the porcine descending aorta." Biomaterials **27**(28): 4955-4962.

L. Pompa, Z. U. Rahman, E. Munoz and W. Haider (2015). "Surface characterization and cytotoxicity response of biodegradable magnesium alloys." Materials Science and Engineering: C **49**: 761-768.

D. Poquillon, V. Baco-Carles, P. Tailhades and E. Andrieu (2002). "Cold compaction of iron powders—relations between powder morphology and mechanical properties: Part II. Bending tests: results and analysis." Powder Technology **126**(1): 75-84.

L. Prodanov, E. Lamers, M. Domanski, R. Luttge, J. A. Jansen and X. F. Walboomers (2013). "The effect of nanometric surface texture on bone contact to titanium implants in rabbit tibia." Biomaterials **34**(12): 2920-2927.

N. C. Quach, P. J. Uggowitzer and P. Schmutz (2008). "Corrosion behaviour of an Mg–Y–RE alloy used in biomedical applications studied by electrochemical techniques." Comptes Rendus Chimie **11**(9): 1043-1054.

J. J. Ramsden, D. M. Allen, D. J. Stephenson, J. R. Alcock, G. Peggs, G. Fuller and G. Goch (2007). "The design and manufacture of biomedical surfaces." CIRP Annals-Manufacturing Technology **56**(2): 687-711.

B. D. Ratner, A. S. Hoffman, F. J. Schoen and J. E. Lemons (2004). Biomaterials Science: An Introduction to Materials in Medicine, Academic Press.

N. A. Riedel, J. D. Williams and K. C. Popat (2011). "Ion beam etching titanium for enhanced osteoblast response." Journal of materials science **46(**18): 6087-6095.

R. Rojaee, M. Fathi, K. Raeissi and M. Taherian (2014). "Electrophoretic deposition of bioactive glass nanopowders on magnesium based alloy for biomedical applications." Ceramics International **40**(6): 7879-7888.

H. Rønold, S. Lyngstadaas and J. Ellingsen (2003). "Analysing the optimal value for titanium implant roughness in bone attachment using a tensile test." Biomaterials **24**(25): 4559-4564.

A. H. M. Sanchez, B. J. Luthringer, F. Feyerabend and R. Willumeit (2015). "Mg and Mg alloys: How comparable are in vitro and in vivo corrosion rates? A review." Acta Biomaterialia **13**: 16-31.

N. E. L. Saris, E. Mervaala, H. Karppanen, J. A. Khawaja and A. Lewenstam (2000). "Magnesium: an update on physiological, clinical and analytical aspects." Clinica Chimica Acta **294**(1): 1-26.

N. Sato, K. Kubo, M. Yamada, N. Hori, T. Suzuki, H. Maeda and T. Ogawa (2009). "Osteoblast mechanoresponses on Ti with different surface topographies." Journal of Dental Research **88**(9): 812-816.

T. Scheerlinck and P.-P. Casteleyn (2006). "The design features of cemented femoral hip implants." Journal of Bone & Joint Surgery, British Volume **88**(11): 1409-1418.

Y. Shibata and Y. Tanimoto (2015). "A review of improved fixation methods for dental implants. Part I: Surface optimization for rapid osseointegration." Journal of Prosthodontic Research **59**(1): 20-33.

L. Smith, P. Midha and A. Graham (1998). "Simulation of metal powder compaction, for the development of a knowledge based powder metallurgy process advisor." Journal of Materials Processing Technology **79**(1): 94-100.

G. J. Swamy, A. Sangamithra and V. Chandrasekar (2014). "Response surface modeling and process optimization of aqueous extraction of natural pigments from Beta vulgaris using Box–Behnken design of experiments." Dyes and Pigments **111**: 64-74.

A. Tahmasebifar, S. Güngör and Z. Evis (2015). "Flor İyonlari İlave Edilmiş Nano-Kalsiyum Fosfatlarin Mikroyapısının Araştırmaları." Journal of the Faculty of Engineering & Architecture of Gazi University **30**(1): 1-7.

Y. Tao, T. Xiong, C. Sun, L. Kong, X. Cui, T. Li and G.-L. Song (2010). "Microstructure and corrosion performance of a cold sprayed aluminium coating on AZ91D magnesium alloy." Corrosion Science **52**(10): 3191-3197.

A. F. van Tol, J. E. Tibballs, N. R. Gjerdet and P. Ellison (2013). "Experimental investigation of the effect of surface roughness on bone-cement-implant shear bond strength." Journal of the Mechanical Behavior of Biomedical Materials **28**: 254-262.

J. Walker, S. Shadanbaz, T. B. Woodfield, M. P. Staiger and G. J. Dias (2014). "Magnesium biomaterials for orthopedic application: a review from a biological perspective." Journal of Biomedical Materials Research Part B: Applied Biomaterials **102**(6): 1316-1331.

R. Walter and M. B. Kannan (2011). "In-vitro degradation behaviour of WE54 magnesium alloy in simulated body fluid." Materials Letters **65**(4): 748-750.

C. A. Walton, H. J. Martin, M. Horstemeyer and P. T. Wang (2012). "Quantification of corrosion mechanisms under immersion and salt-spray environments on an extruded AZ31 magnesium alloy." Corrosion Science **56**: 194-208.

G. Wang, W. Liu, Y. Huang, S. Ma and Z. Zhong (2014). "Effects of sintering temperature on the mechanical properties of sintered NdFeB permanent magnets prepared by spark plasma sintering." Journal of Magnetism and Magnetic Materials **349**: 1-4.

H. Wang, R. Zhang, X. Hu, C.-A. Wang and Y. Huang (2008). "Characterization of a powder metallurgy SiC/Cu–Al composite." Journal of Materials Processing Technology **197**(1): 43-48.

W. F. Wang (2003). "Effect of MnS powder addition and sintering temperature on the corrosion resistance of sintered 303LSC stainless steels." Corrosion Science **45**(5): 957-966.

X. H. Wang, J. S. Li, R. Hu, H. C. Kou and L. Zhou (2013). Mechanical properties and bioactive surface modification via alkali-heat treatment of porous titanium for biomedical applications. Advanced Materials Research, Trans Tech Publ.

Y. Wang, M. Wei and J. Gao (2009). "Improve corrosion resistance of magnesium in simulated body fluid by dicalcium phosphate dihydrate coating." Materials Science and Engineering: C **29**(4): 1311-1316.

Z. Wen, C. Wu, C. Dai and F. Yang (2009). "Corrosion behaviors of Mg and its alloys with different Al contents in a modified simulated body fluid." Journal of Alloys and Compounds **488**(1): 392-399.

E. Willbold, X. Gu, D. Albert, K. Kalla, K. Bobe, M. Brauneis, C. Janning, J. Nellesen, W. Czayka and W. Tillmann (2015). "Effect of the addition of low rare earth elements (lanthanum, neodymium, cerium) on the biodegradation and biocompatibility of magnesium." Acta Biomaterialia **11**: 554-562.

E. Willbold, A. Kaya, R. Kaya, F. Beckmann and F. Witte (2011). "Corrosion of magnesium alloy AZ31 screws is dependent on the implantation site." Materials Science and Engineering: B **176**(20): 1835-1840.

R. Willumeit, J. Fischer, F. Feyerabend, N. Hort, U. Bismayer, S. Heidrich and B. Mihailova (2011). "Chemical surface alteration of biodegradable magnesium exposed to corrosion media." Acta Biomaterialia **7**(6): 2704-2715.

F. Witte (2010). "The history of biodegradable magnesium implants: a review." Acta Biomaterialia **6**(5): 1680-1692.

F. Witte, F. Feyerabend, P. Maier, J. Fischer, M. Störmer, C. Blawert, W. Dietzel and N. Hort (2007). "Biodegradable magnesium–hydroxyapatite metal matrix composites." Biomaterials **28**(13): 2163-2174.

F. Witte, V. Kaese, H. Haferkamp, E. Switzer, A. Meyer-Lindenberg, C. Wirth and H. Windhagen (2005). "In vivo corrosion of four magnesium alloys and the associated bone response." Biomaterials **26**(17): 3557-3563.

F. Witte, H. Ulrich, C. Palm and E. Willbold (2007). "Biodegradable magnesium scaffolds: Part II: Peri ‐ implant bone remodeling." Journal of Biomedical Materials Research Part A **81**(3): 757-765.

I. Wittenbrink, A. Hausmann, K. Schickle, I. Lauria, R. Davtalab, M. Foss, A. Keller and H. Fischer (2015). "Low-aspect ratio nanopatterns on bioinert alumina influence the response and morphology of osteoblast-like cells." Biomaterials **62**: 58-65.

S. Wu, X. Liu, K. W. Yeung, H. Guo, P. Li, T. Hu, C. Y. Chung and P. K. Chu (2013). "Surface nano-architectures and their effects on the mechanical properties and corrosion behavior of Ti-based orthopedic implants." Surface and Coatings Technology **233**: 13-26.

D. H. Xiao, T. C. Yuan, X. Q. Ou and Y. H. He (2011). "Microstructure and mechanical properties of powder metallurgy Ti-Al-Mo-V-Ag alloy." Transactions of Nonferrous Metals Society of China **21**(6): 1269-1276.

Y. Yamada, K. Shimojima, Y. Sakaguchi, M. Mabuchi, M. Nakamura, T. Asahina, T. Mukai, H. Kanahashi and K. Higashi (1999). "Compressive properties of open-cellular SG91A Al and AZ91 Mg." Materials Science and Engineering: A **272**(2): 455-458.

A. Yamamoto and S. Hiromoto (2009). "Effect of inorganic salts, amino acids and proteins on the degradation of pure magnesium in vitro." Materials Science and Engineering: C **29**(5): 1559-1568.

X. Yan, L. x. Hu and S. Yu (2014). "Dynamic recrystallization kinetics of as-cast AZ91D alloy." Transactions of Nonferrous Metals Society of China **24**(6): 1683-1689.

Y. Yun, Z. Dong, D. Yang, M. J. Schulz, V. N. Shanov, S. Yarmolenko, Z. Xu, P. Kumta and C. Sfeir (2009). "Biodegradable Mg corrosion and osteoblast cell culture studies." Materials Science and Engineering: C **29**(6): 1814-1821.

A. Zafari, H. Ghasemi and R. Mahmudi (2014). "An investigation on the tribological behavior of AZ91 and AZ91+ 3wt% RE magnesium alloys at elevated temperatures." Materials & Design **54**: 544-552.

D. Zander and N. A. Zumdick (2015). "Influence of Ca and Zn on the microstructure and corrosion of biodegradable Mg–Ca–Zn alloys." Corrosion Science **93**: 222-233.

R. C. Zeng, J. Zhang, W. J. Huang, W. Dietzel, K. Kainer, C. Blawert and K. Wei (2006). "Review of studies on corrosion of magnesium alloys." Transactions of Nonferrous Metals Society of China **16**: 763-771.

B. Zhang, Y. Hou, X. Wang, Y. Wang and L. Geng (2011). "Mechanical properties, degradation performance and cytotoxicity of Mg–Zn–Ca biomedical alloys with different compositions." Materials Science and Engineering: C **31**(8): 1667-1673.

J. Zhang, C. Dai, J. Wei, Z. Wen, S. Zhang and C. Chen (2013). "Degradable behavior and bioactivity of micro-arc oxidized AZ91D Mg alloy with calcium phosphate/chitosan composite coating in m-SBF." Colloids and Surfaces B: Biointerfaces **111**: 179-187.

J. Zhang, N. Kong, Y. Shi, J. Niu, L. Mao, H. Li, M. Xiong and G. Yuan (2014). "Influence of proteins and cells on in vitro corrosion of Mg–Nd–Zn–Zr alloy." Corrosion Science **85**: 477-481.

L. N. Zhang, Z. T. Hou, X. Ye, Z. B. Xu, X. L. Bai and P. Shang (2013). "The effect of selected alloying element additions on properties of Mg-based alloy as bioimplants: A literature review." Frontiers of Materials Science **7**(3): 227-236.

X. Zhang, Y. J. Li, C. S. WANG, H. W. LI and B.-D. ZHANG (2013). "Corrosion and electrochemical behavior of Mg–Y alloys in 3.5% NaCl solution." Transactions of Nonferrous Metals Society of China **23**(5): 1226-1236.

X. Zhang, K. Zhang, X. g. Li, W. Cong, H. W. Li, C. S. Wang and D. Xia (2011). "Corrosion and electrochemical behavior of as-cast Mg-5Y-7Gd-1Nd-0.5 Zr magnesium alloys in 5% NaCl aqueous solution." Progress in Natural Science: Materials International **21**(4): 314-321.

Y. Zheng, X. Gu and F. Witte (2014). "Biodegradable metals." Materials Science and Engineering: R: Reports **77**: 1-34.

Y. Zheng, Y. Li, J. Chen and Z. Zou (2015). "Effects of tensile and compressive deformation on corrosion behaviour of a Mg–Zn alloy." Corrosion Science **90**: 445-450.

X. Zhong, Q. Li, B. Chen, J. Wang, J. Hu and W. Hu (2009). "Effect of sintering temperature on corrosion properties of sol–gel based Al 2 O 3 coatings on pre-treated AZ91D magnesium alloy." Corrosion Science **51**(12): 2950-2958.

T. Zhou, M. Yang, Z. Zhou, J. Hu and Z. Chen (2013). "Microstructure and mechanical properties of rapidly solidified/powder metallurgy Mg–6Zn and Mg–6Zn–5Ca at room and elevated temperatures." Journal of Alloys and Compounds **560**: 161-166.

W. Zhou, Y. Zheng, M. Leeflang and J. Zhou (2013). "Mechanical property, biocorrosion and in vitro biocompatibility evaluations of Mg–Li–(Al)–(RE) alloys for future cardiovascular stent application." Acta Biomaterialia **9**(10): 8488-8498.

H. Zhuang, Y. Han and A. Feng (2008). "Preparation, mechanical properties and in vitro biodegradation of porous magnesium scaffolds." Materials Science and Engineering: C **28**(8): 1462-1466.

APPENDICES

A. CALIBRATON CURVE FOR ALP ACTIVITY ASSAY

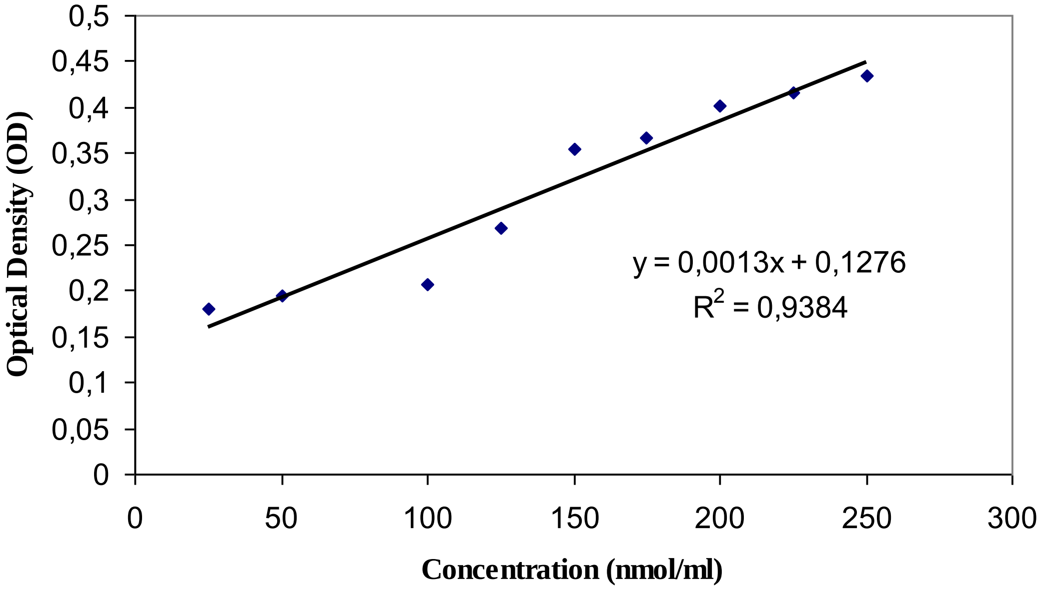

Figure A.1. The calibration curve of p-nitrophenol.

B. CALIBRATON CURVE FOR BCA ASSAY

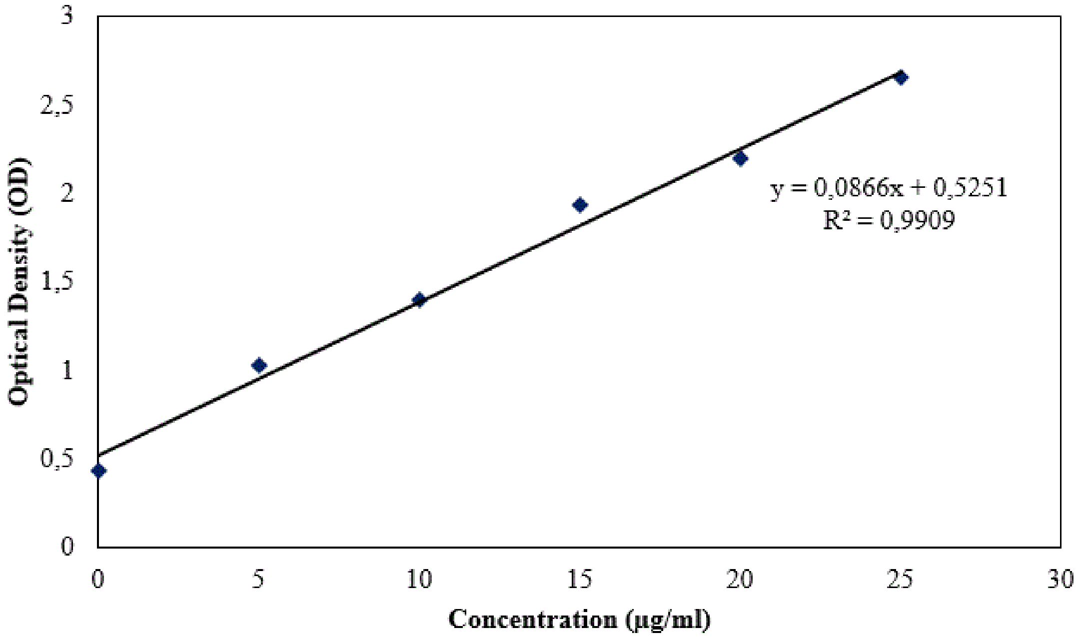

Figure B.1. The calibration curve of bovine serum albumin.

CIRRICULUM VITAE

PERSONAL INFORMATION

Surname, Name: Tahmasebifar, Aydin
Nationality: IRAN
Date and Place of Birth: 28 January 1981, Tabriz
Marital Status: Single
Phone: +90 554 304 2727
Email: aydin.tahmasebifar@gmail.com

EDUCATION

Degree	Institution	Year of Graduation
MS	Middle East Technical University, Engineering Sciences	2011
BS	Sahand University of Technology, Industrial Metallurgy Materials Science and Engineering	2006
High School	Alameh Tabatabayi High Scholl, Tabriz	1999

FOREIGN LANGUAGE

English (Fluent), Turkish (Fluent), French (Beginner)

REFEREED JOURNALS

1- **A. Tahmasebifar**, S. Gungor, Z. Evis, “The Micro-Structural Investigation of Nano-Calcium Phosphates Doped with Fluoride Ions”, Journal of the Faculty of Engineering and Architecture of Gazi University, Vol.30, No 1 (2015), 1-7.
2- **A. Tahmasebifar**, Z. Evis, “Structural and Mechanical Characteristics of Hydroxyapatite and Tri-Calcium Phosphates Doped with Al^{3+} and F^{-} Ions”, Journal of Ceramic and Processing Research, Vol.14, No 4 (2013), 549-556.
3- S. Hossein Nedjad, J.Teimouri, **A.Tahmasebifar**, “A New Concept in Further Alloying of Fe–Ni–Mn Maraging Steels”, Scripta Materialia, Vol. 60 (2009), 528-531.

CONFERENCE PAPERS

1- **A. Tahmasebifar**, S. M. Kayhan, Z. Evis, M. Koç, "Mechanical and Electrochemical Investigation of AZ91D Magnesium alloy as a Biomedical Implant", Submitted and Presented at 24th International Conference on Metallurgy and Materials (METAL 2015), 3-5 June 2015 Brno, Czech Republic.
2- **A. Tahmasebifar**, S. M. Kayhan, Z. Evis, Y. Usta, M. Koç, "Manufacturing and Evaluation of Magnesium-based Surfaces with Porous and Micro-Scale Features for Biomedical Applications", Submitted and Presented at Advances in Materials and Processing Technologies (AMPT), 17-20 November 2014 Dubai, UAE.
3- **A. Tahmasebifar**, S. M. Kayhan, Z. Evis, Y. Usta, M. Koç, "Fabrication of Micro-scale Porous Surfaces for Mg-based Implants", Submitted and Presented at the Materials Science and Technology (MST) 2015 in Advanced Manufacturing Technology Symposium, 12-16 October 2014 Pittsburgh, PA, USA.
4- **A. Tahmasebifar**, S. M. Kayhan, Z. Evis, Y. Usta, M. Koç, "Feasibility Studies for the Manufacturability of Mg-Based Micro-Textured and Porous Surfaces for Biomedical", 7th International Powder Metallurgy Conference & Exhibition (2014), Turkey.
5- Serap Gungor Geridonmez, Zafer Evis, **Aydin Tahmasebifar**, "Nano-Calcium Phosphates Doped With Fluoride and Titanium Ions and Their Sintering Characteristics", 25th European Conference on Biomaterials (2013), Spain.
6- **Aydin Tahmasebifar**, Zafer Evis, Serap Gungor Geridonmez, "Mechanical Properties and Microstructure of Calcium Phosphates Doped with Aluminum and Fluoride Ions", 25th European Conference on Biomaterials (2013), Spain.
7- **A. Tahmasebifar**, Z. Evis, "Structural and mechanical investigation of nano-sized tri-calcium phosphates doped with Al^{3+} and F^- ions",Nanomaterials for Biomedical Technologies (2012), Germany.
8- **A. Tahmasebifar** and Z. Evis, "Microstructural and Mechanical Characterization of Al^{3+} and F^- Doped Tri-calcium Phophates", 13th Ceramics, Cells and Tissues: Regenerative Nano-medicine, Tissue and Genetic Engineering, and the Role of Ceramics (2011), Italy.
9- **A. Tahmasebifar** and Z. Evis, "Investigation of the Microstructural and Mechanical Properties of Nanosize Tri-Calcium Phosphate Doped with Al^{3+} and F^-", Turkish Italian Workshop on the Frontiers of in Nanomaterial Research and Applications (2010), Turkey.

HOBBIES

Playing Basketball, Tennis, Football, Book, Movies